



Jette Bloemberg

MRI-Ready Actuation System for a Self- Propelling Needle

A Design and Experimental Approach

MRI-Ready Actuation System for a Self-Propelling Needle

A Design and Experimental Approach

By

Jette Bloemberg

in partial fulfilment of the requirements for the degree of

Master of Science

in Mechanical Engineering

at the Delft University of Technology,

to be defended publicly on Wednesday February 17, 2021 at 15:30.

Student number:	4364384	
Project duration:	May 20, 2020 – February 17, 2021	
Supervisors:	Ir. F. Trauzettel	TU Delft
	Prof. dr. ir. P. Breedveld	TU Delft
	Dr. D. Dodou	TU Delft
Thesis committee:	Prof. dr. ir. P. Breedveld	TU Delft
	Ir. F. Trauzettel	TU Delft
	Dr. D. Dodou	TU Delft
	Dr. ir. M. Langelaar	TU Delft
	Dr. J. Jovanova	TU Delft

An electronic version of this thesis is available at <http://repository.tudelft.nl/>.



Preface

After a long match, where I spent more time at home than the other five and a half years of my studies, I have won: my master thesis is finished! The research was performed within the BITE (Bio-Inspired Technology) research group at the TU Delft in collaboration with the Amsterdam University Medical Centres (AUMC). Preceding research in the BITE-group had focussed on a wasp-inspired, self-propelling needle driven by electromagnetic motors. The research described in this master thesis report is on a self-propelling needle used inside an MRI scanner. I was assigned to design, develop, and test a version of this self-propelling needle without conductive, metallic, or magnetic components. I wrote this thesis as part of my master's degree in mechanical engineering, specialised in biomechanical design.

During my project, many people have helped me. First of all, I would like to thank Fabian Trauzettel, Dimitra Dodou, and Paul Breedveld for their support. I appreciate how the three of you guided me through this project and how you were always willing to make time to help. Thank you, David Jager from DEMO (Dienst Elektronische en Mechanische Ontwikkeling), for your time and help in producing the needle. Thank you, Luigi van Riel, Gustav Strijkers, Bram Coolen, Martijn de Bruin, and Theo de Reijke from the AUMC for the useful discussions about the application of the project in focal laser ablation for prostate cancer treatment and the help in designing the setup and performing the experiments inside the MRI scanner. Furthermore, I would like to thank my roommates for the best daily cappuccino breaks. Lastly, thanks to my friends and family for being supportive, helping me where possible, brainstorming or proofreading, and going for a walk. Need-les(s) to say, I hope you enjoy your reading.

Jette Bloemberg
Delft, February 2021

Contents

Abstract	1
Keywords	1
Abbreviations	1
Nomenclature	1
1. Introduction	1
1.1 Focal laser ablation.....	1
1.2 Wasp-inspired needles.....	2
1.3 Problem statement	4
1.4 Goal of the research.....	5
1.5 Structure of the report.....	5
2. Requirements.....	5
2.1 Must haves.....	5
2.1.1 Performance.....	5
2.1.2 Dimensions.....	6
2.1.3 Materials	6
2.2 Nice to haves	6
3. Design.....	7
3.1 Actuation unit: layout.....	7
3.2 Actuation unit: rotational selector	8
3.3 Steering unit	11
3.4 Putting it all together	13
4. Prototype	16
4.1 Material selection	16
4.2 MR compatibility tests	17
4.3 Prototype manufacturing	19
4.3.1 Needle.....	19
4.3.2 Actuation & steering unit	19
4.3.3 Support structure	19
4.3 Functionality test	21

5. Evaluation.....	22
5.1 Goal of the experiment	22
5.2 Experimental setup	23
5.3 Experimental procedure	23
5.4 Experimental results	24
5.5 Interpretation of the results.....	26
6. Discussion	27
6.1 Limitations	27
6.1.1 Limitations of the prototype	27
6.1.2 Limitations of the experiment	27
6.2 Future work	28
6.2.1 Pneumatic actuation	28
6.2.2 Phantom studies.....	29
6.2.3 Towards clinical use	29
7. Conclusion.....	31
Acknowledgements	32
References	32
Appendix A. Functional analysis self-propelling needles.....	39
Appendix B. State of the art pneumatic actuators	41
Appendix C. Idea generation.....	43
C.1 Needle segment motion actuation.....	43
C.2 Connect needle segments to actuation unit.....	43
C.3 Interconnect needle segments	44
C.4 Provide orientation endpoint needle	44
C.5 Allow steering.....	45
C.6 Lock steering angle.....	46
Appendix D. Concepts rotational selector.....	47
D.1 Axial gear concept.....	47
D.2 Spur gear concept	48
Appendix E. Design iterations concept prototyping.....	51
E.1 Prototype 1	51
E.2 Prototype 2.....	52

E.3 Prototype 3	53
E.4 Prototype 4	54
E.5 Prototype 5	55
E.6 Conclusions concept prototyping	56
Appendix F. Functioning internal mechanism	57
F.1 Selector torque	57
F.2 Selector friction	57
F.3 Manual actuation speed	58
F.4 Cam profile	59
Appendix G. MATLAB code cam analysis	61
Appendix H. Technical drawings manual actuator	65
Appendix I. Magnetic resonance parameters	67
I.1 Nomenclature	67
I.2 MR compatibility tests	67
I.3 <i>Ex vivo</i> experiment	68
Appendix J. Original MR images <i>ex vivo</i> experiment	69
Appendix K. Design pneumatic actuator	71
K.1 Design directions	71
K.2 State of the art 3D-printed soft bellows	71
K.3 Bellows prototype	72
K.3.1 Bellows design 1: multiple folds	73
K.3.2 Bellows design 2: separate folds	74
K.3.3 Bellows design 3: separate folds	74
K.3.4 Bellows design 4: separate folds with support	75
K.3.5 Bellows design 5: multiple folds with support	75
K.3.6 Post-processing	76
K.4 Conclusions bellows	76
Appendix L. Technical drawings pneumatic actuator	77

MRI-Ready Actuation System for a Self-Propelling Needle

A Design and Experimental Approach

Jette Bloemberg

Abstract

Standard treatment methods for prostate cancer often result in side-effects because of damage to the surrounding tissue. Magnetic resonance imaging (MRI) guided focal laser ablation to treat prostate cancer reduces the risk of adverse effects by preserving noncancerous tissue. Prostate cancer diagnosis and focal laser ablation treatment both require the insertion of a needle for biopsy and optical fibre positioning. The insertion of needles in soft tissues causes tissue motion and deformation, resulting in tissue damage. In this study, we propose an MRI-ready actuation system for a needle that can be inserted into tissue with a zero external push force and without buckling. The zero external push force is achieved by moving parallel needle segments in a reciprocating manner. The actuation unit's design inspired by the click-pen mechanism actuates the reciprocating motion of six parallel needle segments by solely a discrete manual translating actuation as its input. A prototype, called the Ovipositor MRI-Needle, was built using 3D printed parts and six 0.25-mm diameter Nitinol rods. Experimental validation of the Ovipositor MRI-Needle in *ex vivo* human prostate tissue inside a preclinical MRI scanner showed that the needle could advance in three out of five measurements through the tissue. The Ovipositor MRI-Needle is a step forward in the direction of developing a self-propelling needle for MRI-guided transperineal laser ablation to treat prostate cancer.

Keywords

Medical needle, magnetic resonance imaging, additive manufacturing, manual actuator, biologically inspired design.

Abbreviations

FDM	Fused deposition modelling
MRI	Magnetic resonance imaging
PLA	Polylactic acid
PMMA	Polymethyl methacrylate
RF	Radiofrequency
SLA	Stereolithography

Nomenclature

l	Length (m)
α, β	Angle (rad)
r	Radius (m)
F	Force (N)
d	Distance (mm)

1. Introduction

1.1 Focal laser ablation

The prostate is a gland about the size of a walnut. It is located directly below the bladder surrounding the urethra (Fig. 1) [1]. The prostate consists of tubuloalveolar glands embedded in smooth muscle and dense connective tissue, enclosed by a thick connective tissue capsule [1]. The prostate's function is to produce a part of the semen that plays a role in activating sperm [1, 2].

Prostate cancer is the second most common cancer diagnosed in men and the fifth leading cause of cancer-related deaths for men worldwide [3, 4]. Radiotherapy and radical prostatectomy are standard treatment methods to treat prostate cancer. However, these methods result in urinary incontinence for respectively 38% and 71% of the patients and erectile dysfunction for respectively 78% and 88% of the patients, reported six months after the treatment [5].

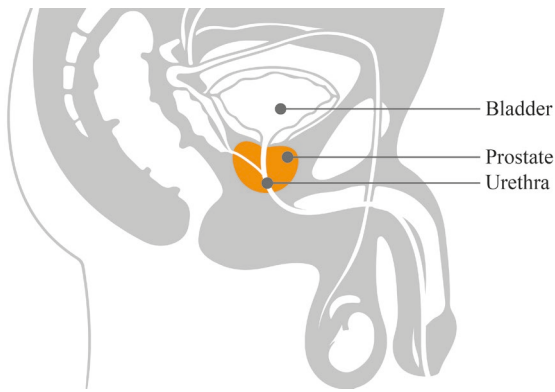


Fig. 1. Schematic representation of the male reproductive organs. The prostate is indicated in orange.

Focal therapy is a treatment option that reduces the risk of side effects by preserving noncancerous tissue because the tumour is treated locally [6]. Focal laser ablation of the prostate is an appealing focal therapy option as it leads to homogeneous tissue necrosis and it does not appear to alter the sexual and urinary function of the patient [7]. In focal laser ablation, a laser fibre is used to destruct tissue thermally [8].

Prostate cancer diagnosis and focal laser ablation both require needle insertion to obtain core biopsies [9, 10] and to position optical fibres near the target zone [11]. In clinical practice, needle insertion is typically performed by pushing the needle through the tissue. Needle insertion might lead to tissue strain in the needle vicinity [12], which in turn might cause functional damage to the surrounding cells [13]. In needle insertion into the prostate, damage by the needle to tissue structures as the urethra, the anterior wall of the rectum, and the pelvic sidewall has to be avoided [14]. As a needle penetrates tissue, both axial and lateral forces cause the tissue to deform [15]. The tissue surrounding the needle is dragged with the needle during needle insertion [12]. Less dragging of the tissue at the interface between the moving needle and the surrounding tissue, can reduce tissue strain and thus limit functional damage [12]. Furthermore, tissue motion and deformation might lead to poor control of the needle path [15]. Hence, clinicians typically need multiple attempts to reach the target location, leading to increased tissue damage [12].

An axial force is required to push the needle through the tissue. When this axial force exceeds

the critical load of the needle, the needle deflects laterally, called buckling [16]. The lateral deflection might damage tissue in the needle vicinity and might lead to poor control of the needle path [17, 18]. Buckling can be prevented by increasing the critical load of the needle or decreasing the penetration load of the tissue [16].

1.2 Wasp-inspired needles

The ovipositor of parasitic wasps has been used as a source of inspiration for medical needle designs [12, 19-21], because it is long and thin, does not buckle, and is able to steer [22]. Parasitic wasps pass their eggs along an ovipositor on or into their hosts, who sometimes hide in a substrate such as wood [23]. The ovipositor consists of one dorsal valve and two ventral valves that the wasp moves in a reciprocating manner (Fig. 2). A groove-and-tongue mechanism interlocks the valves along their length [24, 25]. The push-pull motion of the valves has two functions. First, it keeps the unsupported length of the valves low and independent of the insertion depth [16]. Second, pulling a valve provides stability to the wasp's ovipositor preventing buckling [16, 26, 27], while another valve is pushed with an equal and opposite force [28]. The pulling and pushing forces produce a net force near zero, enabling a self-propelling motion. The ovipositor's steering motion is presumably achieved by selectively advancing the valves to a bevel-shaped tip, which causes deflection of the ovipositor-tip due to the reaction forces applied by the surrounding substrate [29].

Parittotokkaporn et al. [28] showed that samples with a surface texture inspired by the

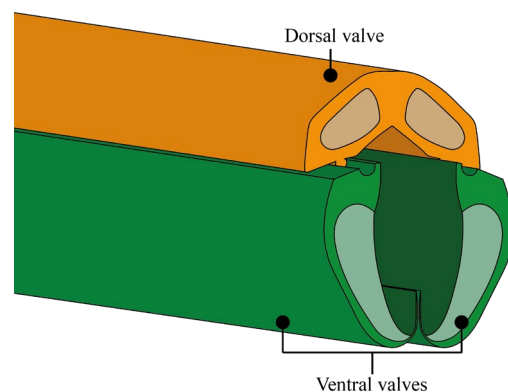


Fig. 2. Schematic representation of the parasitic wasp ovipositor, with the dorsal and ventral valves differentially protruded.

wasp ovipositor actuated with a push-pull motion could move tissue along the surface through the reciprocating, i.e., the push-pull motion, of the samples, without applying an external push force to the tissue. The samples were mounted into reciprocating mechanisms with the sample teeth pressed into the tissue and the remaining part of the sample positioned above the tissue [28]. Frasson et al. [30] developed a probe consisting of two parallel segments with surface serrations and an interlocking mechanism similar to the groove-and-tongue mechanism in the wasp ovipositor. Inserting the segmented needle using a push-pull motion similar to the wasp ovipositor resulted in less tissue displacement and less tissue damage than pushing a single-element needle through the tissue [12].

Scali et al. [29, 32] also developed self-propelling, steerable needle prototypes inspired by the ovipositor of the parasitic wasp. By stepping away from nature and replacing the

interlocking groove-and-tongue mechanism of the valves by off-the-shelf Nitinol rods devoid of serrations and bundled by a shrinking tube, it was possible to produce needles, consisting of six parallel needle segments, with an insertion diameter of 0.84 mm [32]. This insertion diameter is lower than the other ovipositor-inspired needles and probes in the literature that held on to the interlocking mechanism [12, 19, 20, 30]. The needle prototype uses a push-pull mechanism to advance itself with a zero external push force and without buckling [29]. We used the needle consisting of six parallel needle segments that are actuated by six electromagnetic motors in a reciprocating motion in a consecutive manner to accomplish a self-propelling motion developed by Scali et al. [32] as a design starting point (Fig. 3).

For a self-propelling motion of the needle, Eq. 1 holds:

$$-(1F_{fric} + 1F_{cut})_{pro} \leq (5F_{fric})_{re} \quad (1)$$

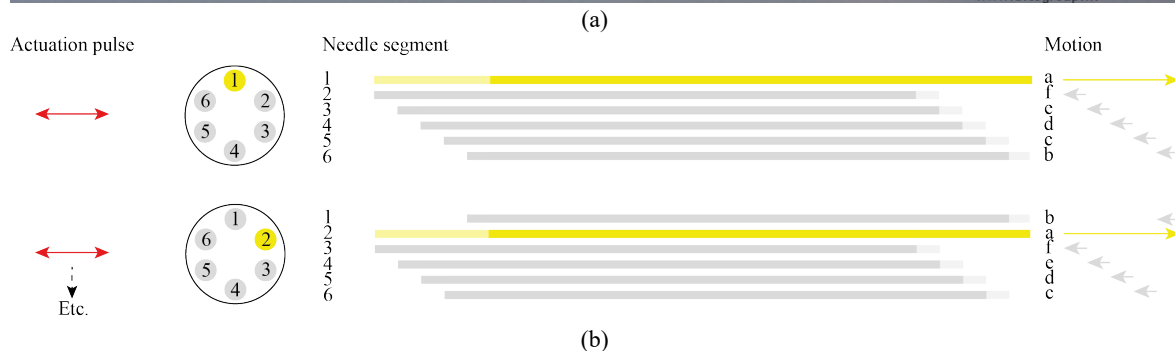
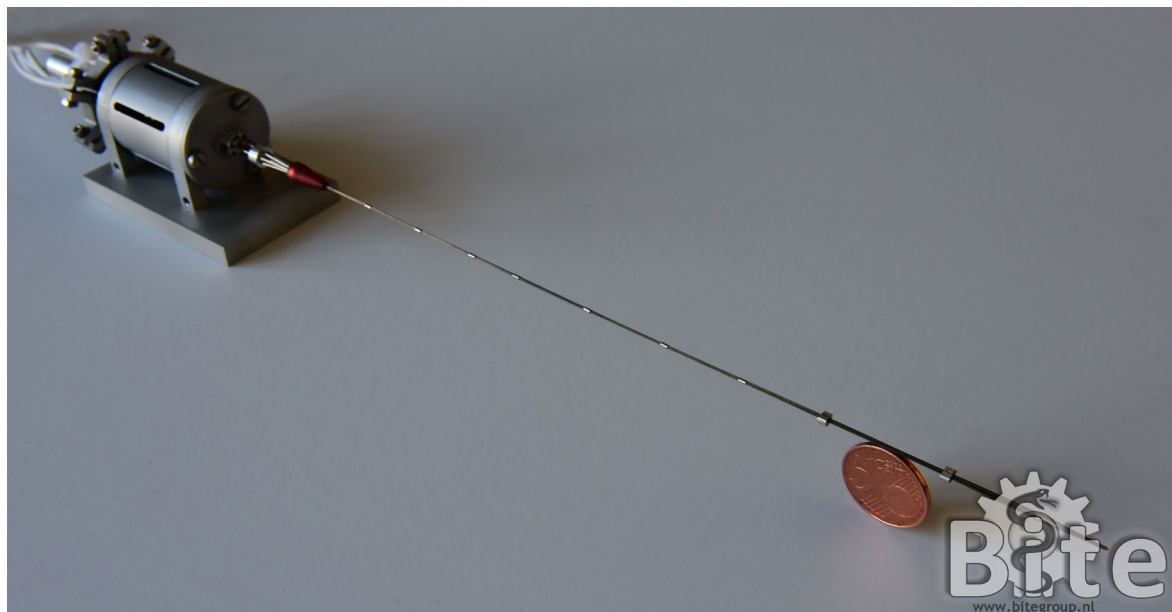


Fig. 3. (a) Photograph of the segmented needle developed by Scali, adapted with permission from [31], actuated by six electromagnetic motors. (b) Visualisation of the motion sequence of the needle segments. As a result of an actuation pulse, one needle segment moves forward over the stroke distance while the other needle segments move backwards over 1/5th of the stroke distance in a consecutive manner. As a result of the subsequent pulse, the adjacent needle segment moves forward over the stroke distance while the other needle segments move backwards.

where $\mathbf{F}_{fric,pro}$ and $\mathbf{F}_{cut,pro}$ are the friction and cutting force of the protruding needle segment, respectively, and $\mathbf{F}_{fric,re}$ is the friction force of one retracting needle segment, assuming that one segment is protruding and the other five retracting. For the self-propelling motion to occur, the friction force of the five retracting needle segments should overcome the sum of the friction force and cutting force of the protruding needle segment. In order for the self-propelling mechanism to work, continuous contact between the outer surface of the needle segments and the surrounding tissue is required [21].

1.3 Problem statement

To guide laser ablation of the prostate, magnetic resonance imaging (MRI) is an attractive imaging option because it provides visualisation of the target zone and real-time temperature monitoring [33, 34]. The human body exists mainly of water, which consists of two hydrogen atoms and one oxygen atom. The nucleus of a hydrogen atom consists of one proton. A clinical MRI scanner applies a strong magnetic field with oscillating gradients that resonate with these protons to generate images of the body's anatomy and physiology [35]. Mapping temperature changes can be achieved based on temperature-dependent MRI parameters, such as the proton resonance frequency, the T_1 relaxation time, and the molecular diffusion constant of water [36, 37]. MRI provides non-ionising, non-invasive, and high-contrast imaging for soft tissues [38].

For the design of instruments used inside an MRI scanner, precautions must be followed to ensure the safety of the patient and other persons within the MR environment. The ASTM F2503 standard distinguishes three classifications for medical devices in the MR environment: MR safe, MR conditional, and MR unsafe [39]. MR-safe devices are composed of materials that are electrically non-conductive, non-metallic, and non-magnetic; these devices are inherently safe to use in an MR environment [39]. MR conditional devices are safe only when used within defined operating conditions. MR unsafe devices, e.g., stainless steel instruments, pose unacceptable risks to the persons within the MR environment.

Self-propelling needles enable the clinician to reach the target tissue while avoiding unwanted tissue damage in and around the prostate. Past prototypes of a self-propelling needle based on the wasp's ovipositor used electromagnetic motors to actuate the individual needle segments [21, 30]. The primary application of the needle developed in this study is MRI-guided transperineal focal laser ablation of prostate tumours. Therefore, electromagnetic motors are not an option due to the interference of these motors with the magnetic field. The interference induces safety hazards and distorts the MR images [40]. In this research, we focused on designing a new MRI-ready actuation system for a self-propelling needle and evaluating its performance in prostate tissue.

We opted to replace the electromagnetic motors by an MR-safe actuator that uses a power supply that is commonly available in MRI rooms. Alternative actuation methods are piezo motors, ultrasonic motors, Bowden cables, pneumatics, hydraulics, magnetic spheres, and shape memory alloy actuators. Piezo motors, ultrasonic motors, and shape memory alloy actuators require the use of metallic materials [41], which makes it impossible to make them MR safe. Regarding Bowden cables, friction, backlash, and inertia of the cables make an effective energy transfer difficult [41]. Magnetic spheres induce imaging artefacts [41]. In a hospital setup, pneumatics, compared to hydraulics, are advantageous as pressurised air is commonly available in an MRI room. Moreover, in pneumatics, small leakages are acceptable, whereas in hydraulics, leaks are to be avoided [42]. We chose pneumatic actuation as pneumatics allow for MR-safe actuation, pressurised air is commonly available in MRI rooms, and pneumatic actuation systems allow for small leakages.

An important drawback of pneumatics is that air is compressible, so the only well-defined pneumatic actuator positions are the beginning and end positions. This makes pneumatic actuators more suited for a discrete, stepwise motion instead of a continuous motion [43]. The mechanism of a stepper motor can overcome the air compressibility obstacle by using a pneumatic actuator to drive a mechanism in discrete steps [43, 44]. In this research, we

applied this discrete actuation for a stepper motor to drive a self-propelling needle.

One way to test the principle of an MRI-ready mechanism that actuates the motion sequence of a self-propelling needle is to develop the pneumatics and to test the needle with pneumatic actuation. If the actuation unit and the pneumatics work, the needle will self-propel through the tissue. Another way to test the actuation principle is by manually actuating the needle unit by the same motion as the pneumatic actuator. In this case, the functionality of the needle segment actuation mechanism and the needle protruding in the target tissue are evaluated. Here, we opted for a discrete manual translating actuation similar to the pneumatic actuation [40]. An actuator using a discrete manual input motion allows for easy adaptation to pneumatic actuation in a future version of the MRI-ready actuation system.

1.4 Goal of the research

Ovipositor-inspired, self-propelling needles developed up to now by Frasson et al. [30] and Scali [21] are actuated by electromagnetic motors. These needles cannot be used in MRI-guided procedures, as the electromagnetic motors interfere with the magnetic field. The main goal of this study is:

To develop and experimentally validate a self-propelling needle with an MRI-ready actuation unit that converts a discrete translating motion into the reciprocating motion of parallel needle segments that form the needle.

Subgoals of this study are:

- To design an actuation system that converts a discrete manual translating motion into the reciprocating motion of the parallel needle segments;
- To manufacture a prototype, containing the actuation system and needle, entirely out of MRI-ready materials;
- To develop a needle that is sharp enough to self-propel through human prostate tissue.

Additionally, the design should not obstruct a mechanism to steer the needle and allow

functionalisation of the needle core primarily for optical biopsy and focal laser ablation.

1.5 Structure of the report

The first part of this paper, Section 2, describes the design requirements set for the needle and the actuation unit presented in this study. Section 3 presents the conceptual and final design. Section 4 describes the production of the prototype, followed by an experimental evaluation of the self-propelling performance in *ex vivo* prostate tissue in Section 5. Finally, Sections 6 and 7 discuss and conclude the findings of this study, respectively.

2. Requirements

2.1 Must haves

We established a set of design requirements for the needle and the needle actuation unit at the start of the design process. A brief overview of the design requirement can be found in Table I. The must-have requirements are essential for the functioning and usefulness of the prototype to be developed in this study.

2.1.1 Performance

- 1) *Manual actuation.* The input motion of the actuation unit is a discrete manual translating motion. Discrete manual actuation is used as the input motion in this study to evaluate the functionality of the prototype's internal mechanism and allow for easy adaptation to pneumatic actuation in a future version of the design.
- 2) *Parallel needle segments [6].* The needle consists of six parallel needle segments with a central core to implement the self-propelling motion, applied in the segmented needle developed by Scali et al. [32], of the six needle segments to position a central element in the body.
- 3) *Needle segment stroke [4 mm].* In order to advance the needle using a self-propelling motion, the needle segments require actuation of a reciprocating motion over a 4-mm stroke distance, in line with the stroke applied in the segmented needle developed by Scali [21].

- 4) *Continuous actuation of the needle segments.* The needle segments are in motion continuously in order to apply a constant strain to the surrounding tissue: one needle segment moves forward until the stroke value is reached while the remaining five needle segments move 1/5th of the stroke value backwards in a consecutive manner.
- 5) *Maximum needle segment offset [4 mm].* The offset between the needle segments at the needle tip can be varied between 0 and 4 mm to allow for steering, this is in line with the needle segment offset in the steering experiment performed by Scali [21].

2.1.2 Dimensions

- 6) *Needle length [200 mm].* The needle length is 200 mm, to be able to reach the prostate transperineally [45].
- 7) *Needle insertion diameter [0.84 mm].* The needle insertion diameter is 0.84 mm, similar to the needle developed by Scali et al. [32], to comply with the conventional needles used for optical biopsy and optical treatment fibre positioning. Commonly used optical biopsy needles vary in diameter between 1 mm (14 Gauge) and 2 mm (19 Gauge) [46]. Optical treatment fibre positioning commonly requires two to four needles with a diameter of 0.8 mm (21 Gauge) [11].
- 8) *Actuation unit length [200 mm].* The actuation unit is small in order to fit within a closed-bore tunnel-shaped MRI scanner.
- 9) *Actuation unit diameter [60 mm].* The actuation unit has a small diameter in order to fit within a closed-bore tunnel-shaped MRI scanner.
- 10) *Hollow core diameter [1 mm].* The actuation unit contains a central lumen in order to allow insertion of a functional element, such as an optical fibre to apply the needle in optical biopsy and focal laser ablation. Fibres used for optical biopsy and focal laser ablation have diameters ranging from 0.25 to 1.0 mm [47, 48].

2.1.3 Materials

- 11) *MR safe.* The actuation system does not contain metallic, magnetic, or conductive

materials, in order to be inherently MR safe according to ASTM F2503 [39]. The needle is safe to use within the experimental conditions. Materials are determined to be MR safe if they fulfil the ASTM F2503 criteria on the magnetically induced displacement force and torque, and the radio frequency heating [39], tested with ASTM standards F2052, F2213, and F2182, respectively.

- 12) *MR compatible.* The actuation system and the needle introduce no image quality issues, create no radio frequency noise signals, do not interfere with the radio frequency signal, and do not interfere by proton signals of plastics, according to ASTM F2119 [49].
- 13) *Manufacturability: 3D printed.* It is possible to manufacture the prototype's components, excluding the needle, using three-dimensional (3D) printing. 3D printing offers rapid and cheap development and fabrication processes compared to conventional manufacturing methods such as injection moulding [50, 51].

2.2 Nice to haves

The nice-to-have requirements are requirements that a future version of the design should meet to make it suitable for clinical practice. The concept presented in this study does not have to fulfil these requirements yet; however, it should not obstruct the next version of the design closer to clinical practice either.

- 14) *Disposable.* The needle and the actuation unit should be designed and produced as a disposable medical device to comply with the single-use fibre for focal laser ablation [52]. For disposable medical devices, low manufacturing costs, simple fabrication and assembly processes, and terminal sterilisation suitability are important aspects [53, 54].
- 15) *Heat resistant.* The materials and material interconnections used at the needle tip should resist temperatures up to 90°C caused by the laser fibre tip [55, 56].
- 16) *Biocompatible.* The materials used in the needle in contact with the patient should be biocompatible according to ISO 10993.

Table I. Design requirements for the needle and needle actuation unit.

Description	Value
<i>Must have:</i>	
1) Manual actuation	-
2) Number of needle segments	6
3) Needle segment stroke	4 mm
4) Continuous actuation of needle segments	-
5) Maximum needle segment offset	4 mm
6) Needle length	200 mm
7) Needle insertion diameter	0.84 mm
8) Actuation unit length	200 mm
9) Actuation unit diameter	60 mm
10) Hollow core diameter	1 mm
11) MR safe	-
12) MR compatible	-
13) Manufacturability: 3D printed	-
<i>Nice to have:</i>	
14) Disposable	-
15) Heat resistant	90°C
16) Biocompatible	-

3. Design

3.1 Actuation unit: layout

The needle’s self-propelling motion requires a sequential translation of the needle segments in six steps per cycle. During every step of the motion, one needle segment moves forward over a specified distance called the “stroke” while the other needle segments move slowly backwards over 1/5th of the stroke distance (Fig. 3b). The sequential translation of the needle segments can be manually actuated by (a) separately actuating the six needle segments using six individual

discrete manual translations (Fig. 4a) or by (b) converting the reciprocating motion of a single discrete manual translation into a global rotating motion of a rotational selector, after which the rotational selector selects and actuates the needle segments in the required order and over the required distance (Fig. 4b). The first design option is similar to the actuation applied in the needle developed by Scali [21], by replacing the six electromagnetic motors in that system by six manual actuators, requiring six hands. Additionally, a workflow support system is required to indicate to the operator the order and the duration of the operation of the correct manual actuator. As every needle segment should go through the same sequence of translating motions, the second design option requires only one manual actuator and seems more space-efficient, providing that a well-working rotational selector can be designed within the required dimensions of the actuation unit (length 200 mm, diameter 60 mm). For this reason, we looked into the design of a rotational selector actuated by a discrete, stepwise motion. More detailed considerations that affected the design of the manually actuated needle are discussed in Appendices A-C. These considerations include a functional analysis of existing self-propelling needles driven by electromagnetic motors compared to the needle in this study, a state-of-the-art overview of the pneumatic actuators in the scientific and patent literature, and the preliminary idea generation process for our Ovipositor MRI-Needle.

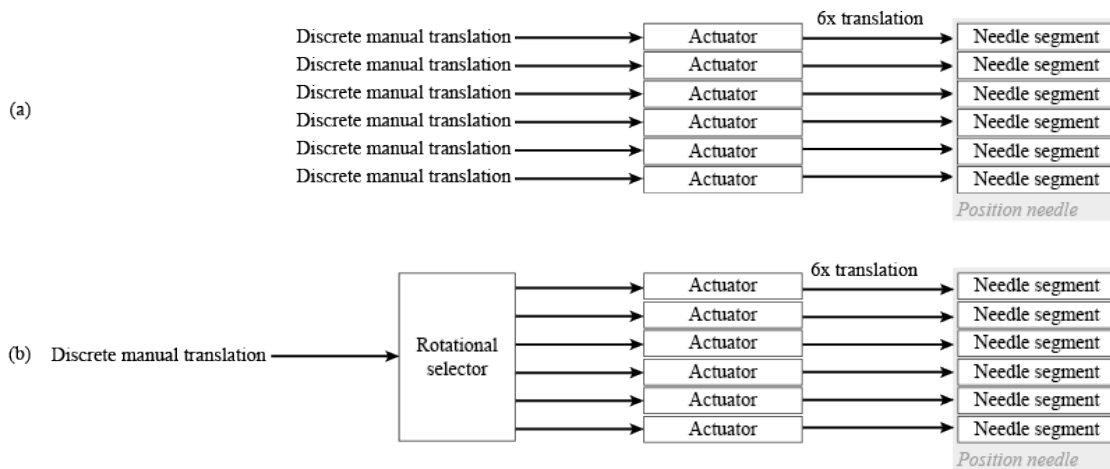


Fig. 4. Actuation sequences for obtaining the required motion sequences of the needle segments. (a) The six needle segments are individually actuated by six discrete manual translations, requiring six hands. (b) A rotational selector in front of the translational actuators is actuated by one discrete manual translation. The rotational selector actuates a rotation and selectively actuates the required translation for each needle segment.

3.2 Actuation unit: rotational selector

During the course of this project, a number of design concepts for the rotational selector were generated (Appendix D). This section focuses on the winning design concept that turned out to be best suited for this study. The design is based on the so-called click-pen-mechanism of a ballpoint pen. Fig. 5 shows the first patented click-pen-mechanism (Parker Pen Co Ltd) [57] and an exploded view of a slightly different click-pen-mechanism. The click-pen-mechanism converts the discrete motion of pressing the button at the end of the pen into a rotation and a subsequent translation of the ballpoint tip.

The rotational selector implements the motion conversion mechanism of the click-pen to convert a discrete manual translating motion into the rotation of an intermediate element and

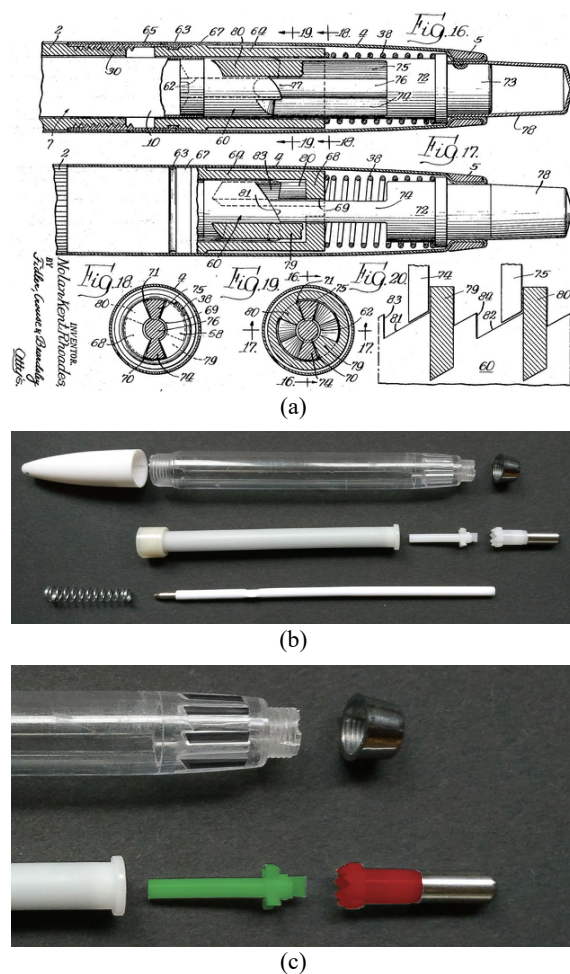


Fig. 5. (a) Illustration of one of the first patented click-pen-mechanisms (Parker Pen Co Ltd) [57] (b) Photograph of a disassembled ballpoint pen with a click-pen-mechanism. (c) Close-up of the same click-pen-mechanism, with the button in red, and the translating and rotating part in green.

translations of the needle segments. Fig. 6 shows the working principle of the rotational selector. The cylindrical mechanism is simplified and visualised in a flat two-dimensional (2D) schematic illustration for an easy explanation of the working principle. The columns in Fig. 6 show the subsequent steps in the motion cycle. The rows in Fig. 6 show the different layers of the rotational selector.

The selector (in green) contains two sets of teeth that are aligned. A housing (in grey) also contains two sets of teeth. The housing is fixed with respect to the surroundings. For the housing, the teeth at the right are shifted over half a tooth width relative to the teeth at the left. The selector is actuated by the input motion: a discrete translating motion in the horizontal z-direction. When the selector is moved in the positive z-direction (Fig. 6a), the teeth at the right side of the selector come in contact with the teeth at the right side of the housing (Fig. 6b, the interacting teeth of the housing are indicated in dark grey). The interaction between the teeth at the right side of the housing and the teeth at the right side of the selector causes the selector to move in the positive y-direction over half the pitch-distance of the teeth until the selector cannot move further in the positive z- and y-directions because the teeth at the right side of the housing block the selector. In the following step, the selector is moved in the negative z-direction (Fig. 6c) until the selector's left teeth come in contact with the housing's left teeth (Fig. 6d). The interaction between the housing's left teeth and the selector's left teeth causes the selector to move again in the positive y-direction over half the pitch-distance of the teeth until the housing's left teeth block the selector again.

The stepwise translation of the selector in the y-direction in the simplified 2D illustration in Fig. 6 is, in reality, a stepwise rotation around the z-axis in 3D. The interaction between the teeth of the selector and the housing converts the discrete horizontal translating motion that actuates the selector into a stepwise rotation of the selector.

Figs 6e-h show that the selector contains small protruding cylinders (in dark green) that can slide in straight horizontal slots in a cam (in orange). The housing prevents the cam from translating in the horizontal z-direction. When

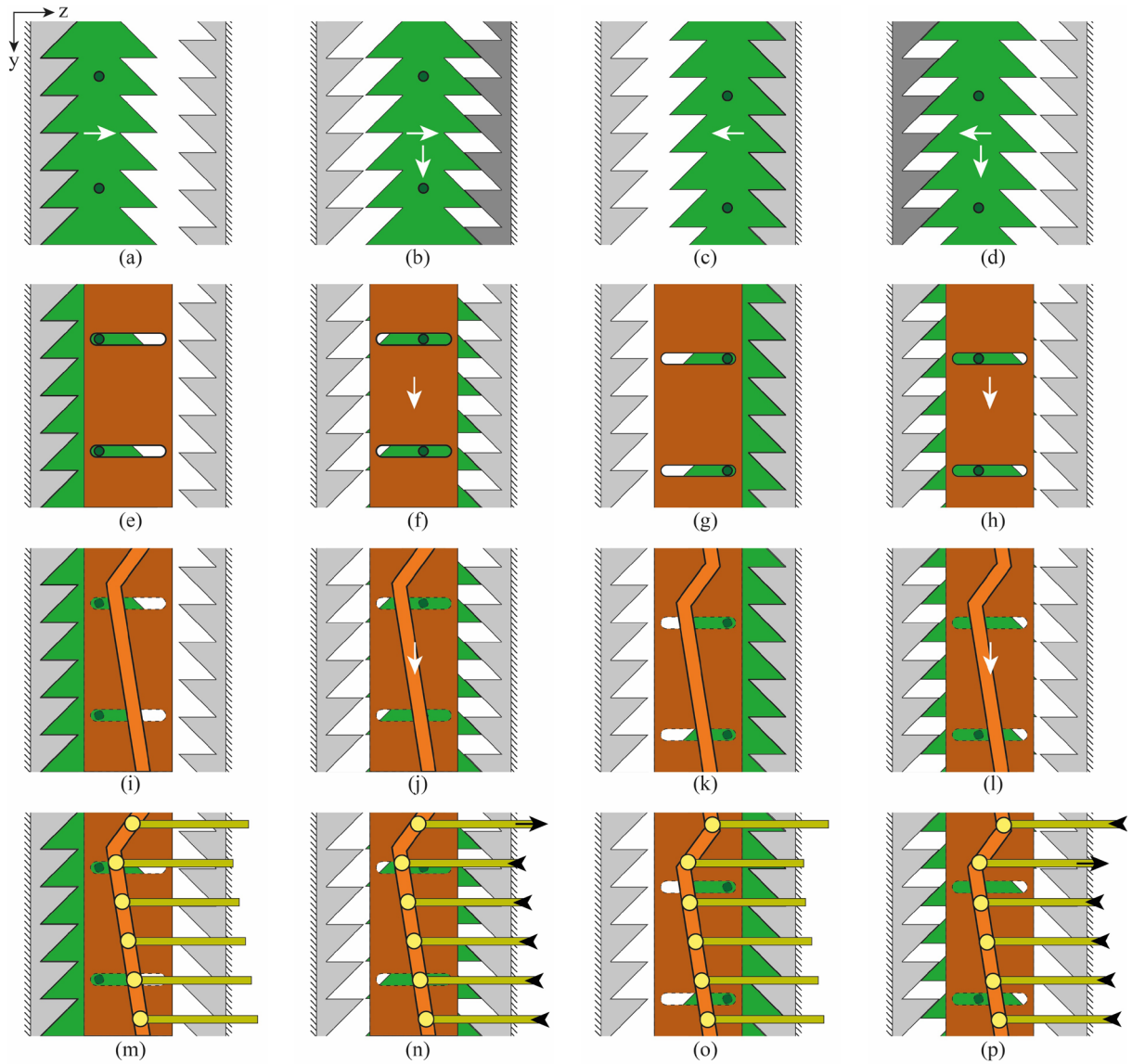


Fig. 6. Two-dimensional schematic representation of the rotational selector motion mechanism including the selector (in green), the housing (in grey), the cam (in orange), and the needle segment holders (in yellow). The columns show the subsequent steps in the motion cycle. The rows show the different layers of the rotational selector. The arrows indicate the next move for the part. For an explanation of the working principle, the reader is referred to the text.

the selector is translated in the positive or negative z -direction, the protruding cylinders of the selector transmit the selector's stepwise translation in the y -direction to the cam (Figs 6f,h). The stepwise translation of the cam in the y -direction in the simplified 2D illustration in Fig. 6 is in 3D a stepwise rotation of a ring-shaped cam around the z -axis.

Figs 6i-l show that the cam contains a V-shaped slot (in light orange). Six needle segment holders (Figs 6m-p, in yellow) contain small protruding cylinders (in light yellow) that can slide in the cam's V-shaped slot. The needle

segment holders are divided over the length of the V-shaped slot. The housing restricts the needle segment holders to their translating motion in the z -direction so they can only move in the z -direction caused by the motion of the V-shaped slot in the y -direction. The combination of the equal division of the needle segment holders over the length of the slot and the V-shape of the slot causes one needle segment holder to move in the positive z -direction, whereas the other needle segment holders move slowly in the negative z -direction (Figs 6m-p).

Fig. 7 shows the 3D working principle of the selector (in green), surrounded by a concentric housing (in grey) and driving the six needle segment holders (in yellow) via the cam (in orange), the inside of the mechanism containing a hollow core for the introduction of additional instrumentation. Fig. 8 shows the assembled actuation unit, including a cone to converge the needle segments to the insertion diameter. The cone has an S-shape to keep constant and maximum radii of curvature of the needle segments. The housing and the selector both contain six teeth at the left and right sides. Therefore, the translation of the selector in the positive or the negative z-direction results in a 30°-rotation of the selector around the z-axis as the selector slides over half the pitch-distance of

the teeth. An iterative design process on the exact shape of the actuation unit was carried out using 3D printing in order to refine the mechanism. One challenge was to actuate the required translating motions of the needle segment holders without additional translations in the z-direction like in the click-pen-mechanism of a ballpoint pen. In the click-pen-mechanism, the same teeth cause both the rotation and translation of the ballpoint tip, which imposes an additional translation on the intermediate part to overcome the barrier of the teeth in each step. Moreover, the best teeth angle to allow for a smooth motion and the optimal clearance for moving parts within the resolution and print quality of the used 3D printer were explored. The teeth angle is a trade-off between

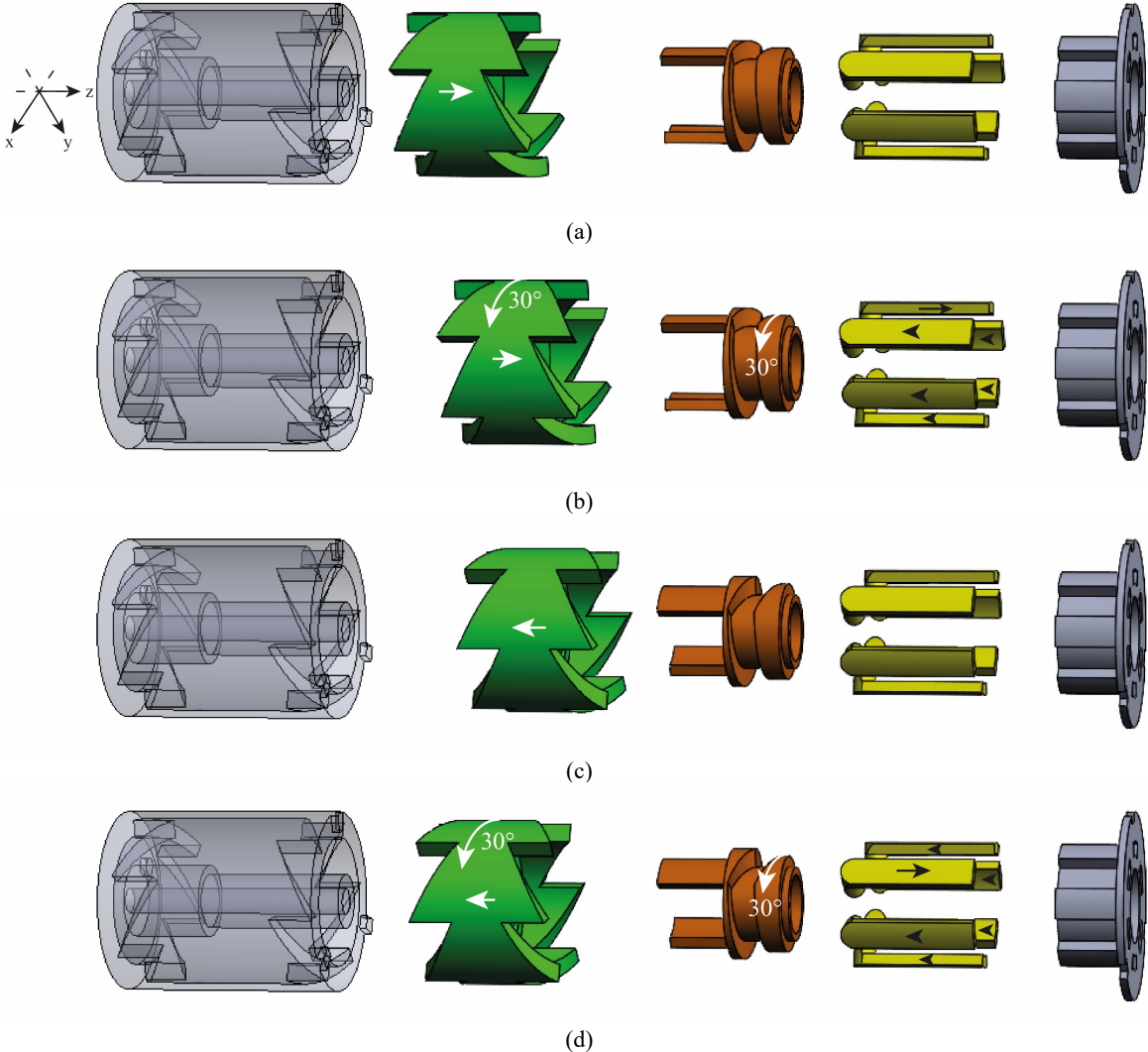


Fig. 7. Motion sequence of the rotational selector in 3D, including the selector (in green), the housing (in grey), the cam (in orange), and the needle segment holders (in yellow). The subfigures show the motions of the components caused by a single back and forth translation of the selector in the z-direction. The arrows indicate the next move for the part. For an explanation of the working principle, the reader is referred to the text.

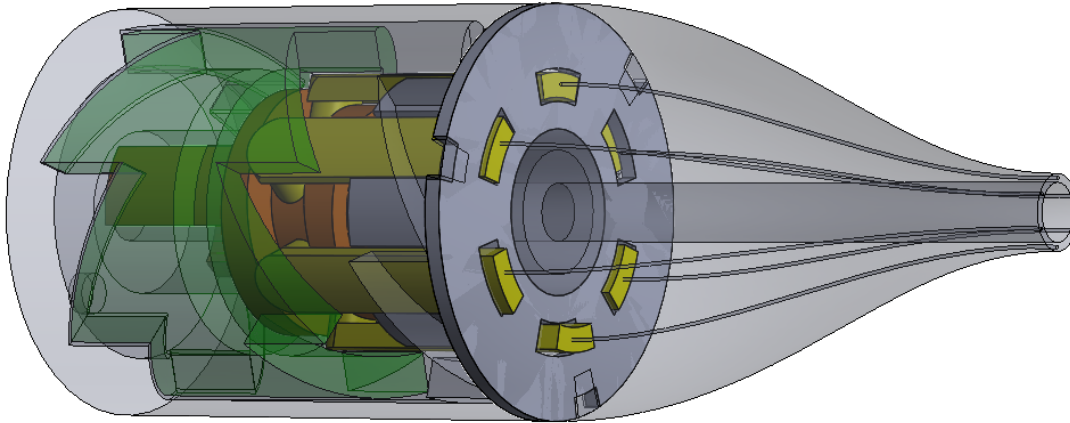


Fig. 8. Actuation unit consisting of a selector (in green), a cam (in orange), and six needle segment holders (in yellow). The needle segments are converged to the insertion diameter using a cone with embedded channels for the needle segments.

a low friction force between the selector's and the housing's teeth and a low selector stroke, thus a low actuation unit's length. For more details about this iterative process, the reader is referred to Appendix E.

3.3 Steering unit

Steering is achieved in our prototype by creating an offset between the needle segment tips to approximate a bevel-shaped tip (Fig. 9) [29]. The surrounding tissue exerts forces on the bevel-shaped tip in an asymmetric fashion, resulting in bending of the needle in the direction of the bevel [58]. Research by Scali et al. [29] on wasp-inspired needles showed that approximated bevel-shaped tips could indeed be used to steer the needle successfully.

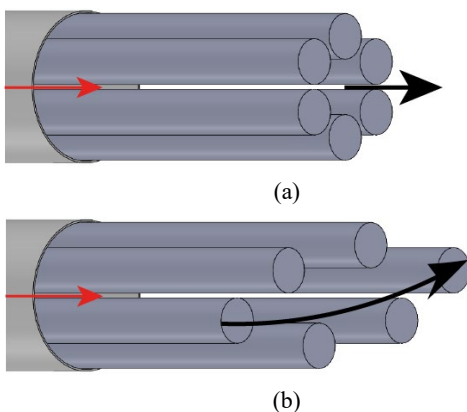


Fig. 9. Visualisation of the needle tip showing (a) the straight configuration without an offset between the needle segments and (b) the steering configuration with an offset between the needle segments to approximate a bevel-shaped tip changing the direction of motion of the needle tip (black arrow) from the actuation direction of the needle segments (red arrow).

Instead of individually advancing the selected needle segments to approximate a bevel-shaped tip, like in Scali [29], we used a more simple steering system by implementing a global steering unit. The steering unit was inspired by the mechanism applied in the I-Flex [59] (Fig. 10); a steerable surgical instrument prototype designed for minimally invasive eye surgery and controlled by six steel cables. Fig. 11a shows the motion of the housing with respect to the cone to create an offset between the needle segments at the needle tip. The housing is tilted with a pitch and yaw motion with respect to the cone around its centre of rotation at the cone's proximal end. Tilting of the housing pushes and pulls the needle segments into and out of the cone, thereby shifting the needle segments over the required offset in a controlled manner. Shifting of the needle segments results in a bevel-shaped tip.

In order to allow for global steering, the connection between the cone and the housing should allow a pitch and yaw motion and maintain a high torsion stiffness to prevent a roll motion (Fig. 11b). A roll motion is problematic because it would twist the needle segments at the



Fig. 10. Photograph of the I-Flex, a steerable surgical instrument prototype that applies a global steering mechanism to steer the tip of the instrument. Adapted with permission from [59].

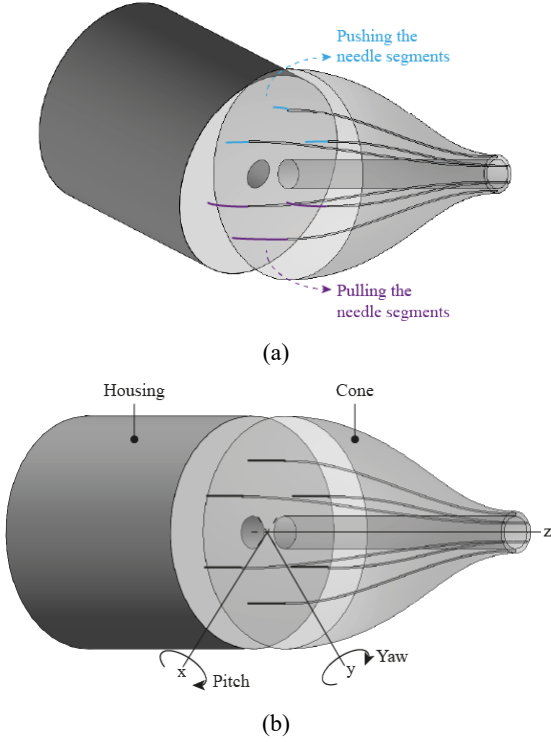


Fig. 11. Visualisation of the shifting of the needle segments to initiate a bevel-shaped tip. (a) Tilting of the housing with respect to the cone results in pushing (blue) of the needle segments on one side of the housing and therefore protrusion of these needle segments at the tip. Whereas on the opposite side, the needle segments are being pulled (purple), resulting in retraction of these needle segments at the tip. (b) A pitch and yaw tilting motion of the housing with respect to the cone results in shifting of the needle segments.

distal end of the needle with respect to the needle segments inside the actuation unit, i.e., at the proximal end of the needle. As a result, the operator would no longer know which needle segment at the distal end corresponds to which needle segment at the proximal end, which would lead to confusion about the steering direction. Furthermore, twisting of the needle segments could result in the needle segments getting entangled. Entanglement of the needle segments prohibits the needle segments' individual motions, thereby impeding the self-propelling motion of the needle.

Fig. 12 shows the structure implemented in our design that allows a yaw and pitch motion, whereas it maintains a high torsion stiffness. We used a linear cone joined base-to-base with the above-mentioned S-shaped cone, resulting in a double cone. The added linear cone allows a yaw and pitch motion of the housing with respect to

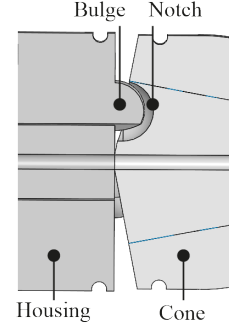


Fig. 12. Visualisation of the cross-section with bulges and notches to allow a yaw and pitch motion of the housing with respect to the cone, while preventing a roll motion.

the double cone. Three notches in the linear cone combined with three bulges in the housing maintain a high torsion stiffness. The bulges of the housing fit exactly into the notches of the linear cone because the notch is the negative shape of the bulge. The combination of the bulges and notches provides a high torsion stiffness to prevent the housing's roll motion with respect to the double cone.

Following design requirement 5, the maximum needle segment offset is 4 mm. This offset is the difference in the z-position between the tip of the needle segment that is pushed forward the most, and the tip of the needle segment that is pulled back the most caused by tilting the housing with respect to the double cone. The steepness of the linear cone determines the feasible angles between the housing and the double cone and thus the maximum needle segment offset. The needle segments are Nitinol rods. The rod segments between the housing and the double cone bend when the housing is tilted with respect to the double cone. The length of the needle segment between the housing and the double cone was approximated with the formula for the arc length (Fig. 13, Eq. 2) because we assumed the rods behave like beams that bend uniformly:

$$l_{needle0} = r_{needle}\alpha \quad (2)$$

where $l_{needle0}$ is the length of the needle segment between the housing and the double cone in the neutral position. Angle α is the angle between the housing and the double cone and r_{needle} is the distance between the centre of the double cone and the needle segment. To allow a

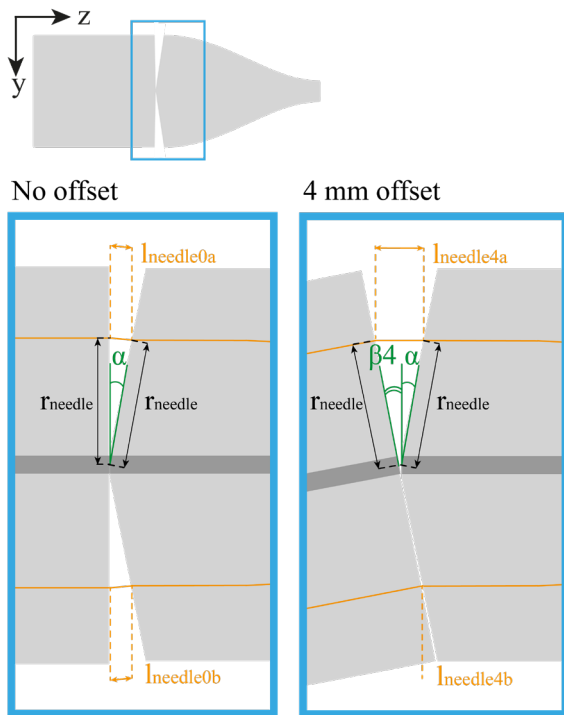


Fig. 13. Visualisation of the cross-section when there is no offset or a 4-mm offset between the needle segments at the needle tip.

maximum 4-mm offset, the angle between housing and the double cone is set to 10° in the neutral position.

3.4 Putting it all together

The complete design consists of a needle and a combined actuation and steering unit. According to design requirements 2 and 7 on the number of needle segments and the needle insertion diameter, to comply with the conventional needles used for optical biopsy and optical treatment fibre positioning, the needle in this

study consists of six 0.25-mm diameter Nitinol rods, i.e., the needle segments. Following design requirement 8, the needle length was set to 200 mm, to reach the prostate transperineally [45]. Fig. 14 shows that the six needle segments are bundled at the tip using a shrinking tube. The thin-walled shrinking tube holds the needle segments together to limit diverging of the needle segments, while only minimally increasing the insertion diameter. The shrinking tube was fixated to one of the needle segments to maintain its position at the needle tip, similar to the prototype described by Scali et al. [32]. The remaining needle segments can move freely back and forth through the shrinking tube. This way, the needle segments are bundled at the tip, while they can easily move back and forth with respect to each other.

To facilitate manual actuation of the rotational selector, a manual translation ring was added to the actuation unit (Figs 15a,c, Part 4 in red). Following design requirement 1 on manual actuation, the manual translation ring can be operated with a discrete translating motion alternatingly in the positive and negative z-direction (Fig. 15c). Cylindrical pins on the manual translation ring (Fig. 15a, Part 4 in red) interact with a circumferential slot in the selector (Fig. 15a, Part 5 in green), transmitting the translating motion in the z-direction but allowing the selector's rotating motion around the z-axis without the operator needing to rotate their hand. The housing contains three straight horizontal slots to facilitate the passing through of the manual translation ring's cylindrical pins (Fig. 15a, Parts 1,7 in grey).

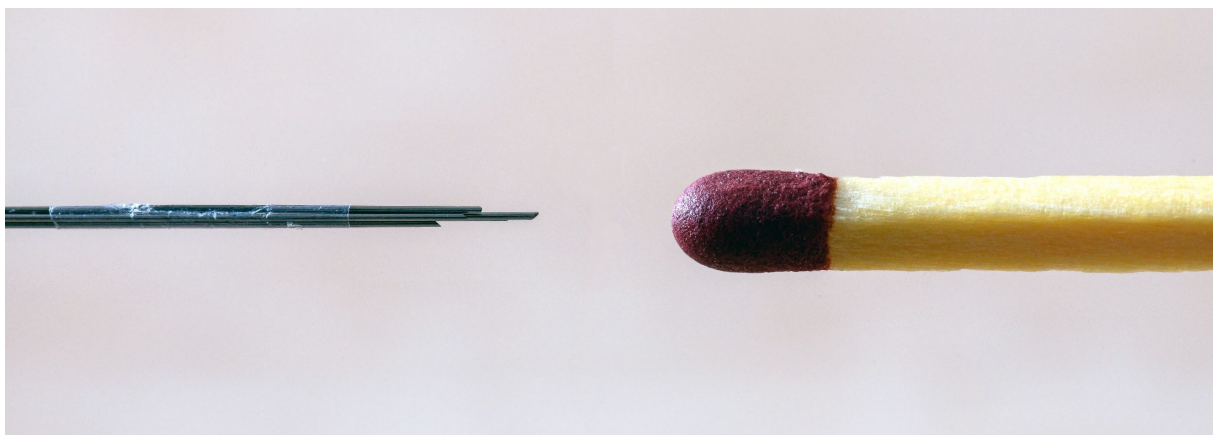


Fig. 14. Close-up photograph of the needle tip consisting of six sharpened Nitinol rods held together by a shrinking tube (Vention Medical) glued to one of the six rods.

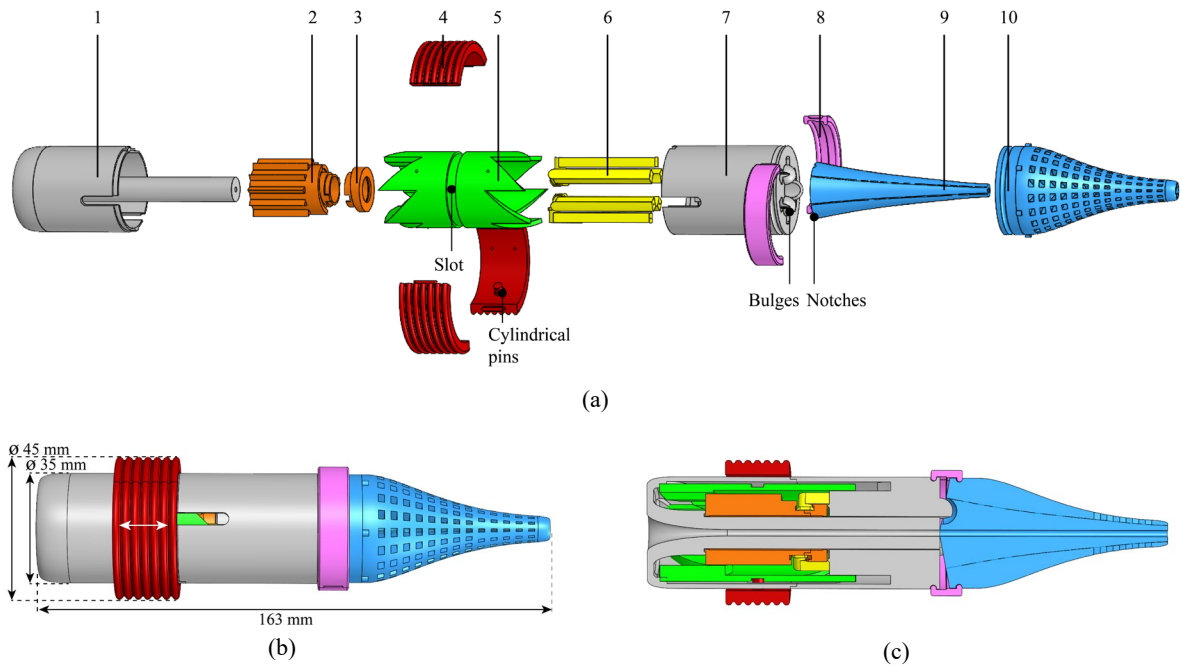


Fig. 15. (a) Exploded view of the actuation and steering unit, consisting of a housing bottom (1), cam bottom (2), cam top (3), manual translation ring (4), selector (5), needle segment holder (6), housing top (7), lock ring (8), double cone inside (9), and double cone outside (10). (b) Sketch of the assembly of the actuation and steering unit, indicating its outer dimensions. The manual actuation of the manual translation ring is indicated with a white arrow. (c) Sketch of the cross-section of the assembly of the actuation and steering unit.

The selector's small protruding cylinders and the cam's straight horizontal slots (Fig. 6) to transmit the selector's rotation to the cam are in reality internal and external spur gear teeth, respectively (Fig. 16a). The teeth are oriented parallel to the horizontal centreline of the selector and cam. Small protruding structures like the selector's cylinders would break off easily due to concentrated loads at the connection between the small protruding cylinders and the selector. The spur gear teeth facilitate the load distribution, due to actuation of the prototype, over the entire width of the gear teeth.

To facilitate a smooth motion, we limited the contact area between the moving components. The manual translation ring's internal surface and the selector's external surface contain dome-shaped protrusions to provide a smooth sliding and rotating motion with respect to the housing (Fig. 16b). The housing and cam contain protruding rings to provide a smooth rotating motion of the cam with respect to the housing (Fig. 16c).

Fig. 17 shows the position-displacement curve of the needle segment holders. Following design requirement 3 on the needle segment stroke, the height of the cam-track dictates a 4-

mm stroke in the positive z-direction for the needle segment holders over a 60° -rotation of the cam. During the following 300° -rotation, the cam-path dictates a 4-mm stroke in the negative z-direction. Hence, rotation of the cam results in the translating sequence of the needle segment holders as visualised in Fig. 3b, conform design requirement 4 on continuous actuation.

The lock ring locks the steering angle of the housing with respect to the double cone (Fig. 15a, Part 8 in pink). Different lock rings were developed for locking the steering angle at the straight configuration or the 4-mm offset configuration.

According to design requirement 13 on the manufacturability, the components of the device should be possible to produce using 3D printing. To facilitate the manufacturability or assembly processes, the cam, housing, and double cone consist of two parts. The cam consists of an upper and lower part (Fig. 15a, Parts 2,3 in orange). Likewise, the cam bottom and top contain the upper and lower part of the V-shaped slot, respectively. Printing the cam in two parts allows both sides of the V-shaped slot to be printed without a support structure adhered to it as required by the 3D printing process. Printing

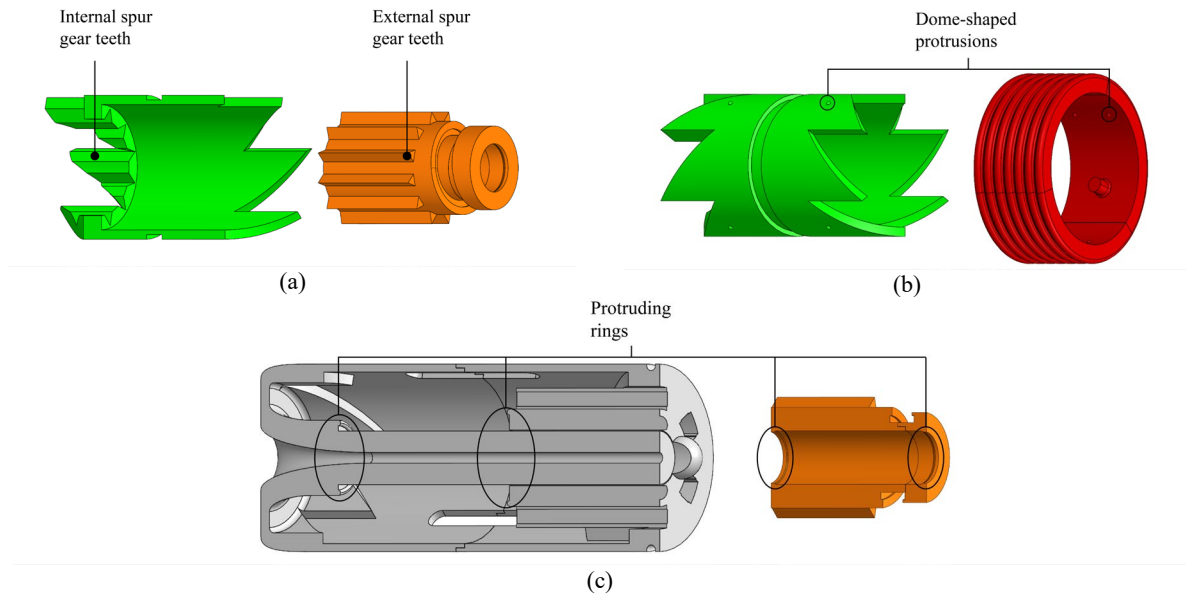


Fig. 16. (a) The selector (in green, cross-section view) and cam (in orange) contain internal and external spur gear, respectively, to transmit the selector's rotation to the cam. (b) The selector (in green) and the manual translation ring (in red) both contain six dome-shaped protrusions to provide a smooth sliding motion with respect to the housing. (c) The housing (in grey, cross-section view) and the cam (in orange, cross-section view) both contain two protruding rings to provide a smooth rotating motion of the cam with respect to the housing.

without support results in a smooth surface of the V-shaped slot without support remainders that could obstruct the needle segment holders' motion. The cam bottom contains protrusions that can be inserted into the cut-out slots in the cam top, as to connect them.

The housing is split into two parts, the housing bottom and top (Fig. 15a, Parts 1,7 in grey), as to allow assembly of the Ovipositor MRI-Needle. The housing bottom and top contain protrusions and cut-out slots similar to those in the cam bottom and top.

The double cone consists of two parts, an outer and an inner part (Fig. 15a, Parts 9,10 in blue). The outer and inner parts of the double cone contain internal and external grooves, respectively. These 0.4-mm diameter grooves allow the needle segments to move back and forth freely (Fig. 18). The double cone consists of two parts to prevent clogging of the needle grooves. Grooves can be printed with smaller dimensions than holes because of clogging

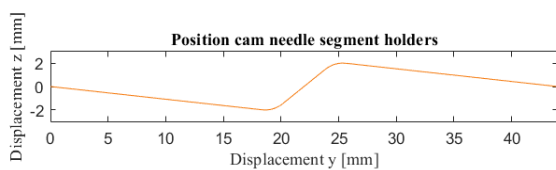


Fig. 17. Z-position in [mm] of the needle segment holder over the circumferential distance (displacement y in [mm]).

issues. Holes with small dimensions have a high risk of clogging during 3D printing because 3D print material is printed or cured around the entire circumference of the hole, compared to recessed features like grooves that only require material to be printed or cured around half the circumference. Furthermore, Fig. 18 shows that a hive structure was used for the outer part of the double cone. The hive structure facilitates the 3D printing process by creating short grooves to prevent clogging [60].

Following dimensional design requirements 8 and 9, the length of the actuation and steering unit is 163 mm (Fig. 15b), the outer diameter is 35 mm, and the outer diameter of the manual translation ring is 45 mm. The hollow core was designed to have a diameter of 2 mm, to comply

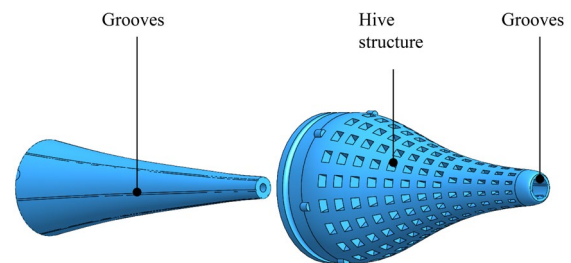


Fig. 18. Exploded view of the double cone, showing the hive structure in the outer part of the double cone and grooves at the intersection of the inner and outer parts of the double cone to prevent clogging of the grooves during the 3D printing process.

to design requirement 10 on a central lumen to allow the insertion of a functional element and simultaneously prevent clogging due to the 3D printing process.

The actuation and steering unit was designed using Solidworks software (Dassault Systems Solidworks Corporation; Waltham, MA, USA). Appendices F-G show more in-depth description of the theoretical and practical functioning of the internal mechanism, such as the displacement, velocity, and acceleration curves of the cam. Appendix H contains the technical drawings of the actuation and steering unit assembly and its parts.

4. Prototype

4.1 Material selection

For use in an MRI scanner, the prototype must be MR safe and MR compatible, following design requirements 11 and 12, respectively. Table II lists the materials contained in the Ovipositor MRI-Needle and the support structure used to position the Ovipositor MRI-Needle inside the MRI scanner.

The needle is composed of nickel-titanium, also called Nitinol. Nitinol is metallic and therefore, MR conditional at best. Nitinol is paramagnetic, which means that an external

Table II. List of materials of the Ovipositor MRI-Needle and its support structure.

Part(s)	Material
Needle	Nitinol
Housing	Polylactic acid (PLA)
Internal components actuation and steering unit	Dental Model V2 resin (Formlabs)
Support structure	PLA, polymethyl methacrylate (PMMA)

magnetic field weakly magnetises it while it loses its magnetism when the external magnetic field is removed [61]. Nitinol has a lower magnetic susceptibility than stainless steel; hence it produces fewer image artefacts than stainless steel [62, 63]. Therefore, medical devices made with Nitinol are generally useful in MRI-guided clinical procedures [64, 65]. The susceptibility difference between the Nitinol device and the surrounding tissue causes a signal void that shows up as a black area in the MR image, which can be used to visualise the Nitinol device [65, 66].

The components of the actuation and steering unit were 3D printed on Formlabs and Ultimaker 3D printers, using Dental Model V2 resin (Formlabs) and polylactic acid (PLA), respectively (Fig. 19). The Formlabs and the Ultimaker 3D printer are a stereolithography (SLA) and fused deposition modelling (FDM) printer, respectively. The housing parts were



Fig. 19. Exploded view of additive manufactured components. The grey parts, i.e., the housing components, were produced using the fused deposition technology (FDM) technology in polylactic acid (PLA) on the Ultimaker 3. The orange parts, i.e., the actuation and steering unit's internal components and the double cone, were produced using the stereolithography (SLA) technology in Dental Model resin V2 (Formlabs) on the Formlabs Form 3B.

printed on the Ultimaker 3D printer (Fig. 19, in grey), whereas the actuation unit's internal components and the double cone were printed on the Formlabs 3D printer (Fig. 19, in orange). The Formlabs 3D printer allows printing with higher accuracy and better surface properties than the Ultimaker 3D printer. The housing components are thin-walled cylindrical components containing straight horizontal slots. Printing the housing components using the Formlabs 3D printer resulted in deformed components. Therefore, we chose to print the housing components using the Ultimaker 3D printer, which resulted in cylindrical parts. For more information about these 3D print processes and their application in medicine, we refer the reader to [50, 67].

In order to test the Ovipositor MRI-Needle inside an MRI scanner, we needed a movable support structure for the tissue. Instead of the general method of moving a needle towards the tissue, we decided to use the opposite method by moving the tissue towards our Ovipositor MRI-Needle, similar to the experimental procedure executed by Scali et al. [29, 32]. Using this method, the actuation and steering unit was kept stationary, fixed to the MRI scanner, in order to use the manual actuation force solely for the subsequent translation of the needle segments with a zero external push force. As a result, the stationary actuation and steering unit prevented the manual actuation force from resulting in an external push force that pushes the needle through the tissue. The principle of needle insertion with a zero external push force holds if the self-propelled needle pulls the tissue towards itself by pulling itself deeper into the tissue.

In order to allow the tissue to move towards the Ovipositor MRI-Needle, we needed a support structure that fits inside the MRI scanner, aligns the needle with the tissue, allows the tissue to move towards the needle with very low friction, and is MR safe and MR compatible. The materials used for the support structure are PLA and polymethyl methacrylate (PMMA). Section 4.3.3 explains the design of the support structure.

4.2 MR compatibility tests

In order to investigate the MR compatibility and visibility of the materials used in the Ovipositor MRI-Needle and the support structure, we conducted two MR compatibility tests. The goal of the first MR compatibility test was to investigate the MR compatibility of the materials used in the support structure and the Ovipositor MRI-Needle's housing and internal components. The goal of the second MR compatibility test was to investigate the MR compatibility of the Nitinol needle and the shrinking tube and to select the best shrinking tube for our design. Fig. 20 shows the preclinical 7-T MRI system (MR Solutions Ltd) used in the MR compatibility tests.

Fig. 21 shows the material samples tested in the first MR compatibility test. The material samples were embedded in 5% weight of gelatine powder in water (wt%) inside a Falcon tube. The Falcon tube used was a 50-mL polypropylene tube with a cap. Gelatine was used for two reasons: (1) gelatine is a watery substance, resulting in a signal in the MR image, whereas air does not provide an MR signal, thus causing a signal void, i.e., a black area in the MR image [68]; and (2) gelatine allows spacing of the material samples with respect to each other inside the Falcon tube, allowing the distinction of the different material samples in the MR image. The lack of hydrogen protons inside the material samples causes a signal void in the MR image. Image artefacts caused by the material can affect the image quality when the signal void created by the component is larger than the component in reality. An increased signal void



Fig. 20. Photograph of the preclinical 7-T MRI system (MR Solutions Ltd) used in the MR compatibility and *ex vivo* tests executed in this study. The MRI system is located at the Amsterdam University Medical Centres.

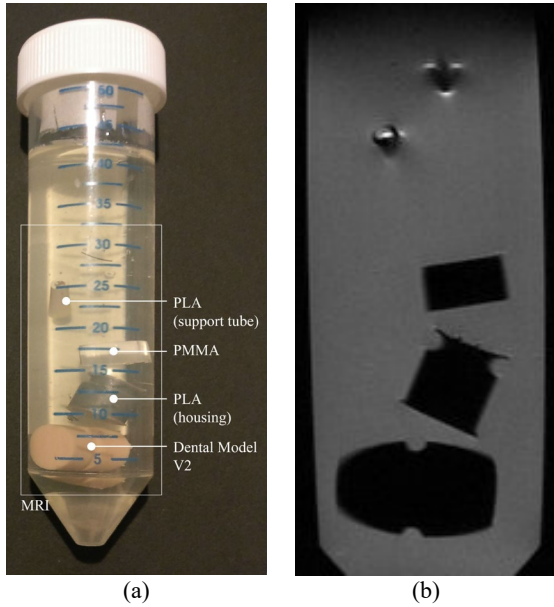


Fig. 21. Samples to test the MR compatibility of the materials used in the prototype, (a) photograph of the materials used in the prototype in a Falcon tube filled with gelatine, (b) MR image of the Falcon tube in (a).

might be caused by a material with a magnetic susceptibility different from the surrounding tissue, which causes a local change of the magnetic field [69]. Fig. 21b shows that the hollow PLA, PMMA, solid PLA, and Dental Model V2 material samples showed signal voids

in the MR image with similar dimensions as the material samples in reality. Around the hollow PLA material sample, two image artefacts showed up. This was probably caused by the presence of small air bubbles inside the hollow PLA tube and the gelatine.

In our study, it is important to be able to determine the position of the needle tip in the MR image. Therefore, the signal void caused by the needle tip should be of approximately the same size as the needle tip in reality. The second MR compatibility test showed the MR compatibility and visibility of the materials in the needle tip. The needle sample consisted of six 0.25-mm diameter Nitinol rod segments in a polyethylene terephthalate glycol-modified holder, which acted as a spacer to keep the Nitinol rod segments centrally aligned in a Falcon tube (Fig. 22b). The Falcon tube was filled up with 5 wt% gelatine, similar to the first MR compatibility test. In the prototype, the needle segments are bundled at the tip by a shrinking tube. In order to investigate the effect of the shrinking tube material on the MR image, four different shrinking tubes were tested. The shrinking tubes from top to bottom in Fig. 22 are Shrinking Tube 1-4 in Table III, respectively.

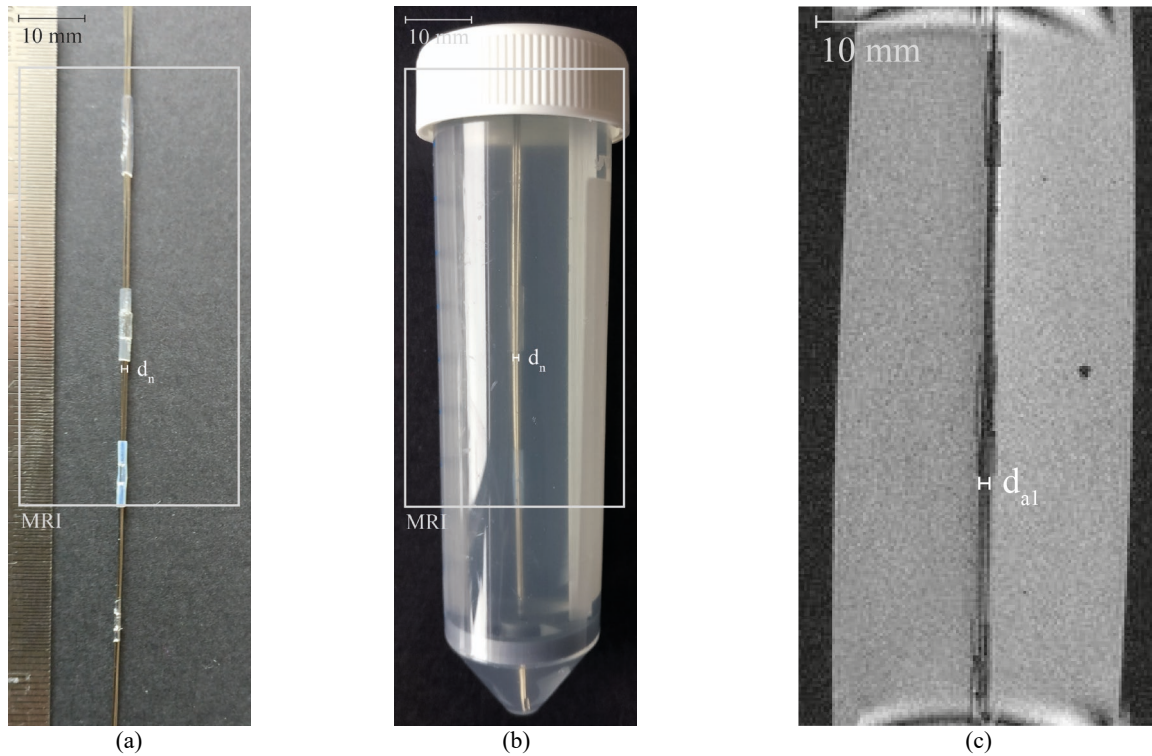


Fig. 22. (a) Photograph of the needle sample used in MR compatibility test 2, d_n is the diameter of the needle, the rectangle visualises what part can be seen in the MR images. (b) Photograph of the needle sample in a Falcon tube filled with 5 wt% gelatine. (c) MR image of the needle sample, d_{a1} is the diameter of the artefact of the needle.

Table III. List of shrinking tubes for MR compatibility test 2 to test the MR compatibility of the needle.

Shrinking Tube name	Expanded inner diameter [mm]	Outer diameter [mm]	Wall thickness [mm]	Material	Company
Shrinking Tube 1	1.14	1.54	0.20	Fluorinated ethylene propylene (FEP)	Zeus Inc.
Shrinking Tube 2	1.00	1.24	0.12	Polyolefin	Tyco electronics
Shrinking Tube 3	0.86	1.16	0.15	Polytetrafluoroethylene (PTFE)	Polyflour
Shrinking Tube 4	0.81	0.84	0.013	Polyethylene terephthalate (PET)	Vention Medical

These shrinking tubes were selected because of their small wall thickness and their difference in material. Fig. 22c shows that all four shrinking tubes and the needle sample barely showed an increased image artefact size. Shrinking Tube 4 was selected for the Ovipositor MRI-Needle prototype, as all four shrinking tubes consist of a suitable material for use in MRI, and Shrinking Tube 4 has the lowest wall thickness. Appendix I states the MR parameters set for the MR images in the MR compatibility tests and the effect of the angulation of the needle with respect to the direction of the magnetic field.

4.3 Prototype manufacturing

4.3.1 Needle

The needle consists of six superelastic straight annealed Nitinol rods with a diameter of 0.25 mm and a length of 276 mm, of which 76 mm was placed inside the actuation and steering unit and 200 mm outside to comply to design requirement 6 on the needle length. The Nitinol rods were glued (Pattex instant glue, Gold Gel) inside the needle segment holders (Fig. 19). The cyanoacrylate-based glue has a gel-structure, which allows for easy application; furthermore, it is inherently biocompatible [70]. Fig. 14 shows the needle segments' tips, sharpened to an angle of 40° with wire electrical discharge machining.

Fig. 14 shows that the six Nitinol rods are held together at the tip by a 10-mm long shrinking tube (Vention Medical, expanded inner diameter 0.814 mm, wall thickness 0.013 mm), i.e., Shrinking Tube 4 in Section 4.2. The shrinking tube was glued (Pattex instant glue, Gold Gel) to one of the Nitinol rods as described by Scali et al. [32]. The resulting insertion diameter of the needle including the shrinking tube is 0.84 mm, conform design requirement 7.

4.3.2 Actuation & steering unit

Fig. 19 shows the components of the actuation and steering unit that were 3D printed using SLA and FDM. The SLA printed parts were printed using the Formlabs Form 3B with a layer height of 0.050 mm. The FDM printed parts were printed using the Ultimaker 3 with a layer height of 0.1 mm.

The cylindrical SLA printed parts, i.e., the selector, cam bottom, and cam top, were printed orthogonal to the build plate, to ensure that their shape remains cylindrical and to avoid unnecessary support structures. Non-orthogonal placement relative to the build plate might result in sagging and drooping of the material due to gravity, and eventually in deviation from the cylindrical shape. The housing bottom and housing top were also printed orthogonal to the build plate to avoid unnecessary support structures.

The housing bottom and housing top were glued together (Pattex instant glue, Gold Gel) during assembling. Fig. 23 shows a photograph of the assembled prototype.

4.3.3 Support structure

A support structure for the Ovipositor MRI-Needle and the target tissue was required to facilitate the evaluation of the Ovipositor MRI-Needle performance inside an MRI scanner. The support structure should provide a steady base for the Ovipositor MRI-Needle that fits within the restricted space available inside the MRI scanner. Furthermore, the support structure should allow moving the tissue towards the needle with very low friction. Fig. 24 shows a simplified illustration of the components that make up the MRI scanner of Fig. 20. The MRI scanner's housing contains a cylindrical bore (inner diameter 95 mm). A horizontal, half-



Fig. 23. Photograph of the assembled prototype, the Ovipositor MRI-Needle. A transparent polymethyl methacrylate (PMMA) support structure supports the prototype. A white polylactic acid (PLA) guide tube supports the needle in the support structure.

round tube (inner radius 45 mm) can be slid into and out of the bore. A cylindrical radiofrequency (RF) coil (inner diameter 65 mm) is placed on top of the half-round tube. The MR image is taken inside the RF coil. During the performance evaluation of the Ovipositor MRI-Needle, we were interested in the position of the needle tip; therefore, the tissue was placed inside the RF coil. The Ovipositor MRI-Needle was attached to the half-round tube while aligning the needle with the tissue.

Fig. 25 shows our developed support structure that consists of an Ovipositor MRI-Needle holder, tube base 1, tube base 2, and needle guide tube. The PMMA support structure that carries the Ovipositor MRI-Needle, called

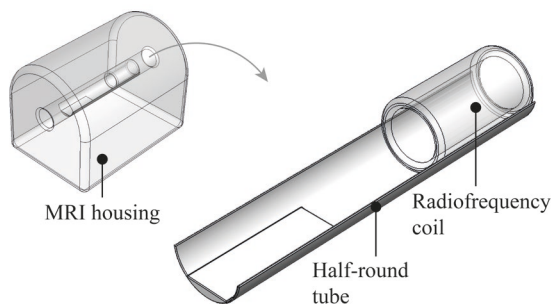


Fig. 24. Illustration of the MRI system used in this study, showing the MRI housing with a half-round tube and a radiofrequency coil that can be slid into and out of the MRI housing.

the Ovipositor MRI-Needle holder (Fig. 20), was produced using laser cutting. The Ovipositor MRI-Needle holder has a flat base; therefore, a component was required that flattens the half-round tube and that lifts the Ovipositor MRI-Needle such that the needle is centrally aligned in the MRI bore. Tube base 1 and 2 fulfil these functions. They were produced out of PLA using the Ultimaker 3. To prevent buckling of the needle before entering the tissue, the needle was supported by the needle guide tube (Fig. 23). The needle guide tube is a PLA tube with an inner diameter of 2 mm and an outer diameter of 3 mm. An extension piece was added to the manual translation ring to allow manual actuation of the Ovipositor MRI-Needle from outside the MRI-bore.

A low-friction structure was required to allow horizontal translation of the tissue inside the RF coil (Fig. 26). This structure had to constrain the rolling motion in the lateral direction but allow a low-friction rolling motion in the axial direction. The tissue had to be centrally aligned in the RF coil, as this position provides the most space for the tissue and results in the least distortions in the MR image.

In the low friction structure, the tissue was placed in a PLA box (height 23 mm, length 100 mm, width 60 mm, weight 58g) produced with a

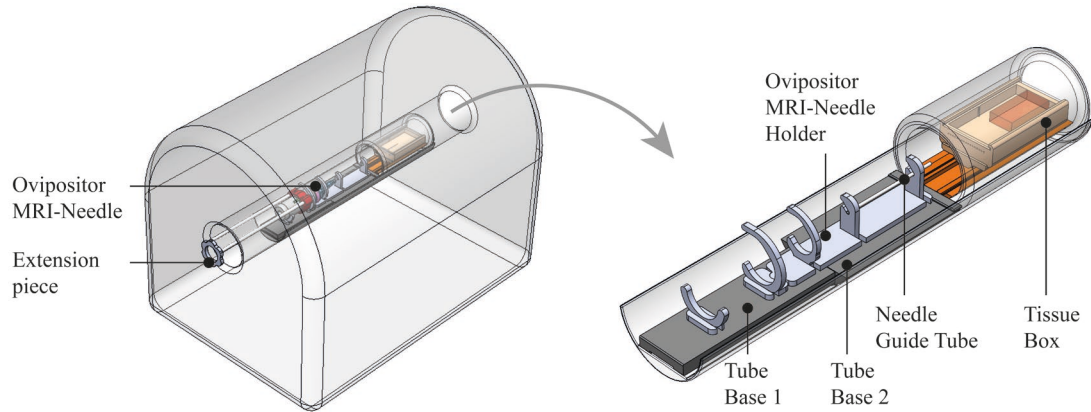


Fig. 25. Illustration of the MRI system used in this study with the support structures to attach the Ovipositor MRI-Needle to the half-round tube and allowing the tissue box to roll inside the radiofrequency coil. The extension piece allows manual actuation of the Ovipositor MRI-Needle from outside the MRI scanner.

Prusa 3D printer. The proximal side of the tissue box contained 17 insertion holes aligned on the x-axis at a 2.5-mm centre-to-centre distance. The insertion holes guided the needle into the tissue in the tissue box. Inside the RF coil, a set of guiding rails was placed. These RF base rails provide a stationary horizontal track. On top of the RF base rails, eight wheels (made from LEGO) were placed as rolling elements: four wheels horizontally aligned at the left and four at the right. Spacers aligned the wheels at a 25-mm centre-to-centre distance; wheel axes were not used. Underneath the tissue box, another set of rails was attached. These box rails provided upper rails for the wheels. The wheels rolled at an angle of 45° between the RF base rails and the box rails, which ensured, in combination with the weight of the tissue box, that the wheels were horizontally aligned.

The restricted space inside the RF coil demanded a solution for the rails and wheels that occupied little space while allowing a low-

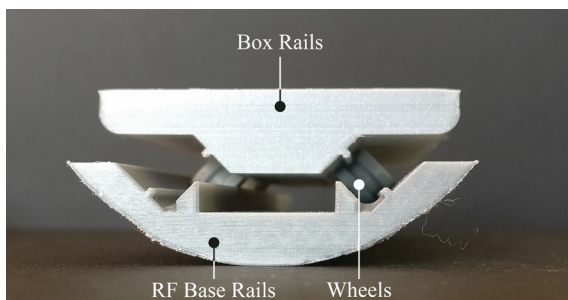


Fig. 26. Photograph of rails used to move the tissue sample. The RF base rails fit inside the radiofrequency coil of the MRI scanner. Wheels between the upper box rails and the lower RF base rails allow sliding of the box rails with respect to the RF base rails.

friction rolling motion. Furthermore, the tissue box on wheels had to remain centrally aligned on the rails when the needle was inserted through one of the off-centre insertion holes, resulting in an off-centre axial force that pulls the tissue towards the needle. For wheels placed at a 0°-angle, there exists a trade-off between narrow rails to keep the tissue box on wheels centrally aligned in the RF coil and wide rails to allow the wheels to roll smoothly and prevent jamming of the wheels when pulling the tissue from the off-centre insertion holes. The wheels at a 45°-angle keep the box rails' motion in the lateral direction aligned with the RF base rails, thereby preventing jamming of the wheels when pulling the tissue from the off-centre insertion holes. Flanges on the RF base rails keep the wheels on the RF base rails, preventing derailing.

Both the RF base rails and box rails were 3D printed parallel to the build plate of the Ultimaker 3 to ensure straight rails and a smooth rolling motion. If the rails were printed orthogonal to the build plate, the layers might have introduced a stair-case effect in the rails.

4.3 Functionality test

A functionality test in a gelatine substrate was conducted in order to assess whether the self-propelling mechanism of the Ovipositor MRI-Needle works (Fig. 27). The goal of the functionality test was to evaluate whether actuating the needle resulted in moving the cart with the gelatine substrate towards the actuation and steering unit due to the needle's self-propelling mechanism.

The test setup consisted of the Ovipositor MRI-Needle in the Ovipositor MRI-Needle holder, the needle guide tube, a gelatine substrate placed on the box rails on wheels, and a base tube that mimicked the cylindrical surface of the RF coil of the MRI scanner. Inside this base tube, the RF base rails were attached.

The gelatine substrate was created by mixing gelatine powder (Dr. Oetker Professional, the Netherlands) with boiled water (ca. 100°C). The concentration of the gelatine was 10 wt% to mimic tissue. The sample was cut to the right dimensions (width 50 mm, length 90 mm, height 10 mm) to fit on the box rails used in the functionality test. Before starting the actuation of the Ovipositor MRI-Needle, the needle was inserted manually to an initial insertion depth of 20 mm, following the experimental procedure described in Scali et al. [32]. The procedure for the functionality test was to actuate the needle for eight cycles and measure the start and end position of the needle tip with respect to the gelatine substrate.

Fig. 28 shows that actuation of the Ovipositor MRI-Needle over eight cycles resulted in a displacement of 18 mm of the gelatine substrate with respect to the needle tip. The theoretical

displacement after eight cycles of actuation is $8 \times 4 \text{ mm} = 32 \text{ mm}$. The difference between the theoretical and actual travelled distance is caused by the slip of the needle segments with respect to the gelatine substrate, as also described in Scali [32]. When the slip is constant and known, the presence of slip does not obstruct the operation of the device. The next step is to evaluate the Ovipositor MRI-Needle's performance in *ex vivo* human prostate tissue inside an MRI scanner to better understand the needle prostate tissue interaction.

5. Evaluation

5.1 Goal of the experiment

In a proof of principle experiment, the functioning of the developed Ovipositor MRI-Needle was evaluated in *ex vivo* human prostate tissue inside an MRI scanner. The performance was evaluated in terms of the slip of the needle with respect to the prostate tissue. More specifically, the slip ratio was calculated over an entire measurement as in Eq. 3:

$$slip_{ratio} = 1 - \left(\frac{d_m}{d_t} \right) \quad (3)$$

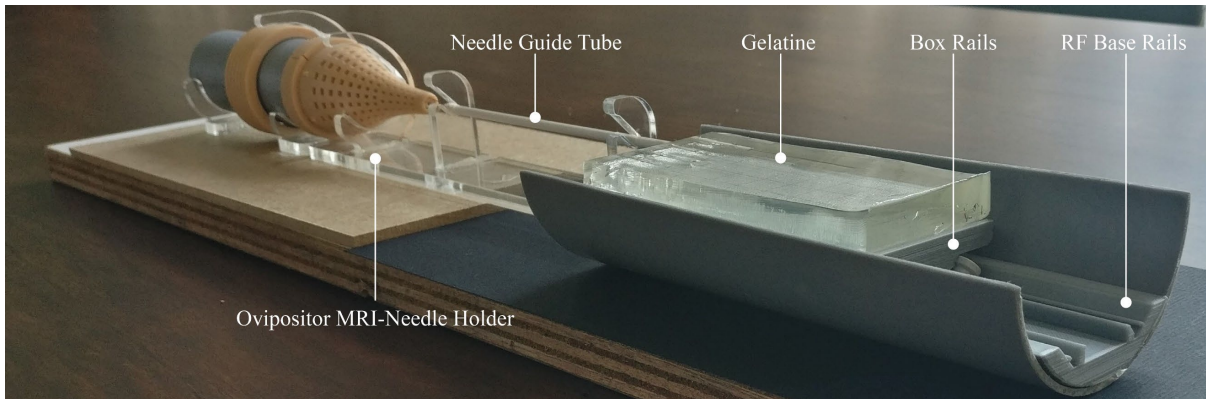


Fig. 27. Photograph of the experimental setup of the functionality test in gelatine.

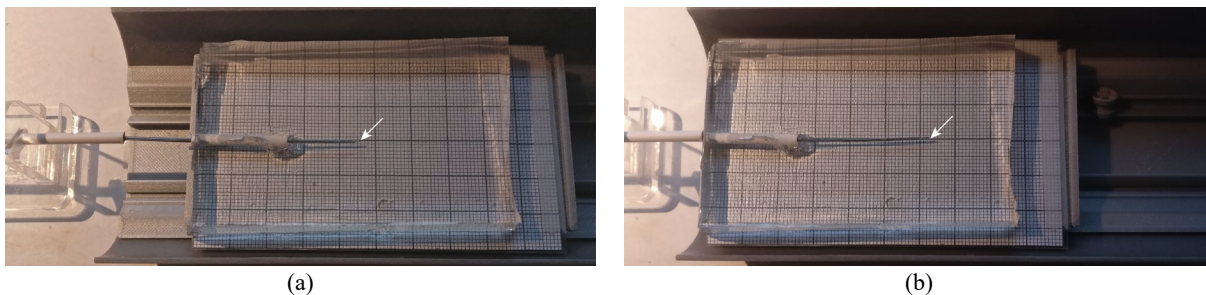


Fig. 28. Photographs of the functionality test of the prototype in gelatine. The white arrow indicates the position of the needle tip. (a) Start position with the needle tip at a 20-mm insertion depth. (b) End position with the needle tip at a 38-mm insertion depth after eight cycles of actuation.

where d_m and d_t are the measured and theoretically travelled distance, respectively.

5.2 Experimental setup

Fig. 29 shows the experimental setup consisting of the Ovipositor MRI-Needle, an *ex vivo* human prostate tissue sample embedded in agar in the tissue box, the support structure as described in Section 4.3.3, and a preclinical 7-T MRI system (MR Solutions Ltd). The Ovipositor MRI-Needle was attached to the Ovipositor MRI-Needle holder using double-sided tape. The RF base rails and tube base 1 and 2 were attached to the RF coil and the half-round tube of the MRI scanner using double-sided tape and Velcro.

The biological sample was prepared by placing a piece of *ex vivo* human prostate tissue (width 25 mm, length 50 mm, height 10 mm) in a box with liquid agar (2.5 wt%). The box was stored in the refrigerator overnight to fixate the tissue in the agar. The sample was cut to the right dimensions (width 50 mm, length 90 mm, height 10 mm, weight 52 g) to fit inside the tissue box used in the experiment. The sample was placed in the tissue box with the prostate tissue placed at the distal end of the tissue box aligned with the central insertion hole. The remaining part of the

tissue box was filled with agar to allow an initial insertion depth of 40 mm of the needle into the agar before entering the prostate tissue. One inner side of the tissue box contains a protrusion with the shape of half a cylinder at the needle's initial insertion depth to act as a reference point in the MR image in order to measure the needle tip's relative position (Fig. 30).

5.3 Experimental procedure

The experimental procedure for each measurement inside the prostate tissue was as follows:

1. An initial needle track of 40 mm was made in the agar in front of the prostate tissue using a rigid 18-Gauge needle, to ensure that the Ovipositor MRI-Needle could be inserted straight.
2. The Ovipositor MRI-Needle was inserted manually through an insertion hole in the tissue box for 40 mm in the initial needle track, to allow for the self-propelling mechanism to work.
3. The tissue box was placed on the wheels on the RF base plate inside the RF coil.
4. The holder containing the Ovipositor MRI-Needle was attached to tube base 1 and 2

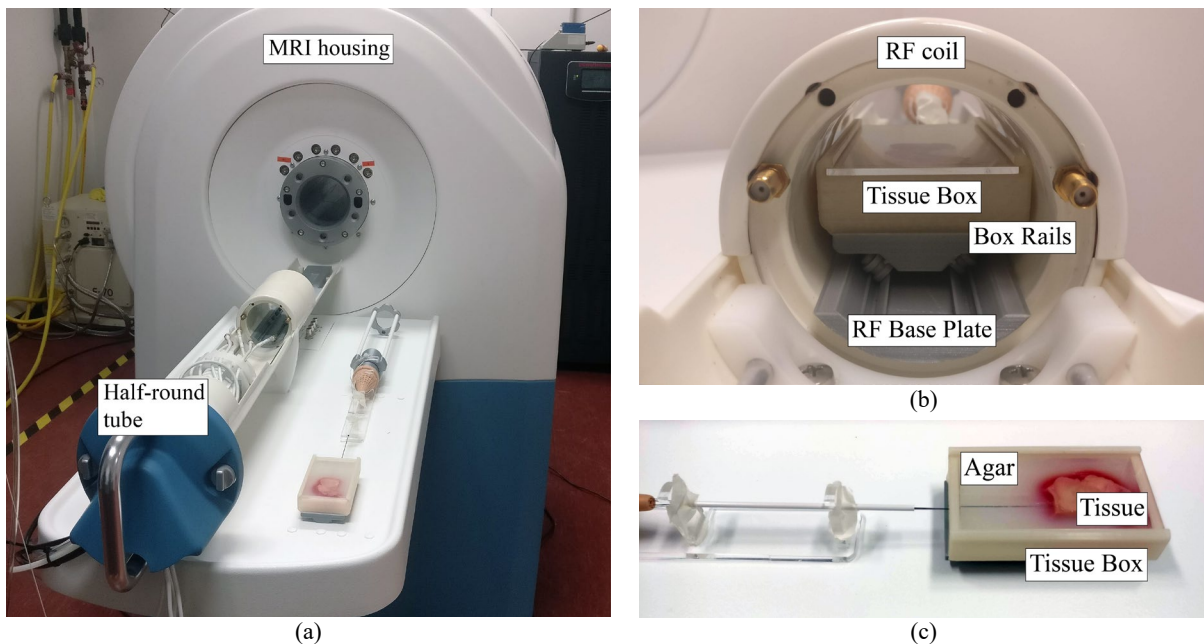


Fig. 29. Photographs of the experimental setup of the *ex vivo* prostate tissue experiment. (a) The instrument was placed in the half-round tube with a support structure in between. The half-round tube was slid into the MRI bore. (b) Close-up of the radiofrequency (RF) coil with the tissue box on the RF base plate. The wheels between the RF base plate and the Box Rails rolled at a 45°-angle. (c) Close up of the *ex vivo* prostate tissue embedded in solidified 2.5 wt% agar, with the needle inserted through the agar in front of the tissue.

- while horizontally aligning the insertion hole of the tissue box with the needle.
5. The experimental setup on the half-round tube was slid into the MRI bore to ensure visualisation of the needle.
 6. The MRI scanner was turned on to obtain the needle tip's start position in an MR image.
 7. The MRI scanner was turned off. The Ovipositor MRI-Needle was manually actuated for five cycles (60 translations) which corresponds to a theoretical distance travelled of 20 mm.
 8. The MRI scanner was turned on to capture the position of the needle tip in an MR image.
 9. The MRI scanner was turned off. If the first actuation resulted in a motion of the needle through the tissue, the Ovipositor MRI-Needle was manually actuated for another five cycles.

10. The MRI scanner was turned on to capture the position of the needle-tip in an MR image.

The needle was cleaned with water and alcohol after each measurement. A different insertion hole of the tissue box in a randomised order was used for each trial. All measurements were conducted over the course of one day.

5.4 Experimental results

MRI sequences were used in order to visualise the start and end position of the needle tip (Appendix I). In the MR images, we added colour indications for the components used for the measurements of the slip ratio (Fig. 30). Fig. 31 shows the MR images of the needle tip positions. The original MR images can be found in Appendix J. Table IV shows the measurements performed during the *ex vivo* prostate tissue experiment.

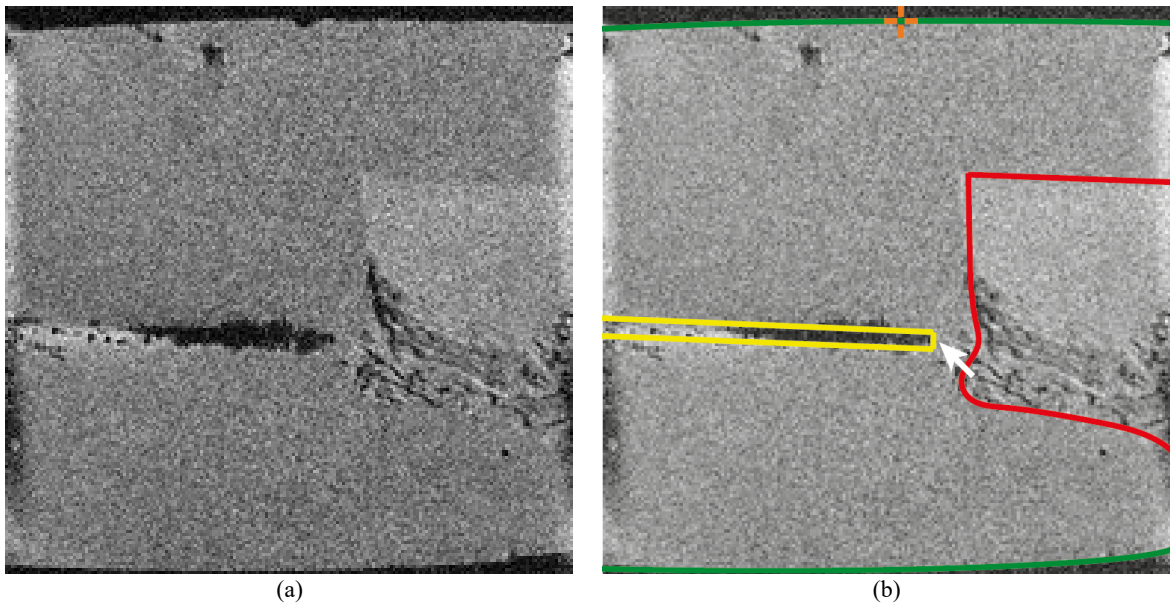


Fig. 30. An example to illustrate how the elements in the MR images used for evaluation were indicated. (a) The original MR image. (b) The adjusted MR image. The yellow, red, and green contours show the needle, the *ex vivo* prostate tissue, and the box sides, respectively. The arrow marks the needle tip. The orange crosshair shows the reference point in the side of the box that indicates a 40-mm insertion depth.

Table IV. Results of the *ex vivo* evaluation. For each measurement, the following information is reported: the insertion hole used on the tissue box, where hole 9 is the central hole, travelled distance [mm] of the box, number of cycles needed to travel that distance, theoretical travelled distance [mm] that the box would have travelled if no slip occurred, and $\text{slip}_{\text{ratio}}$.

Measurement	Insertion hole	Initial insertion depth [mm]	Travelled distance [mm]	Cycles	Theoretical travelled distance [mm]	$\text{slip}_{\text{ratio}}$
1 (excluded)	10	42.4	0	5	20	1.0
2	9	45.0	5.8	10	40	0.86
3 (excluded)	8	48.6	10.0	5	20	0.50
4	6	50.4	2.9	10	40	0.93
5	7	51.8	1.6	10	40	0.96

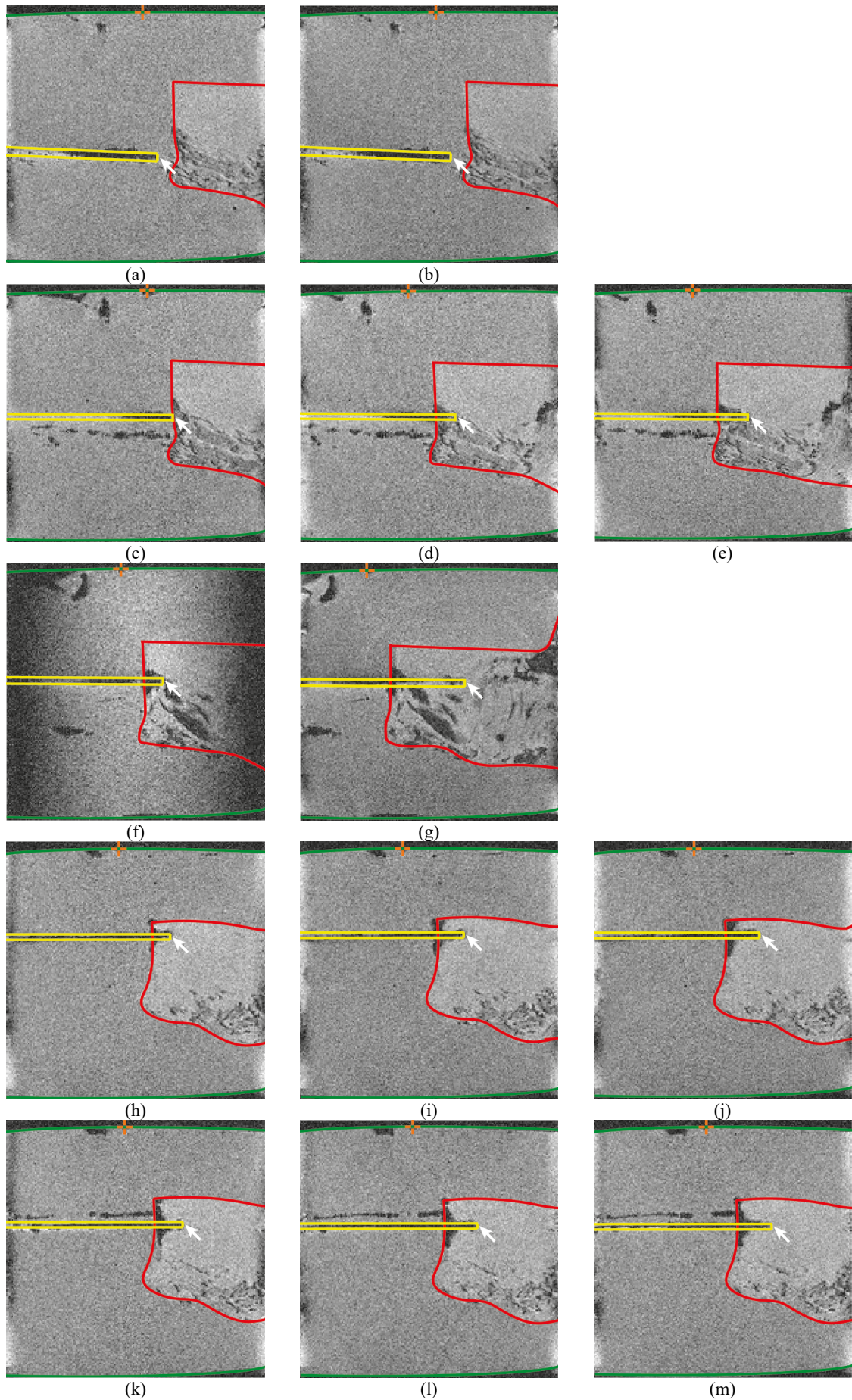


Fig. 31. MR images of the needle inside the agar and *ex vivo* prostate tissue. Each row represents one measurement number. The first column shows the initial frame where the tip is positioned inside the agar in front of the prostate tissue. The second column shows the frame after actuation for five cycles. The third column shows the frame after the second actuation for five cycles. The yellow, red, and green contours show the needle, the prostate tissue, and the box sides, respectively. The arrow marks the needle tip. The orange crosshair shows the reference point in the side of the box that indicates a 40-mm insertion depth.

The MR images show that the lower part of the tissue contained more tissue inhomogeneities than the upper part of the tissue (Figs 30,31). We could not distinguish the needle in the lower side of the tissue because of these tissue inhomogeneities. Therefore, only the upper part of the tissue was used for the experiment. A total of five measurements were conducted. A single measurement equals the insertion of the needle through one hole of the tissue box. For every measurement, the needle position was captured at the start, after actuation for five cycles of actuation, and after another five cycles of actuation if the first five cycles of actuation resulted in a self-propelling motion of the needle. The needle was able to propel itself through the prostate tissue in three out of five measurements. In the first measurement, the needle did not succeed in moving the tissue box. In the third measurement, the needle travelled below the tissue instead of through the tissue. Therefore, the first and third measurement were excluded. In the MR images of the second and fifth measurement, air bubbles in the needle track from previous measurements can be seen.

5.5 Interpretation of the results

In the first measurement, the needle could not penetrate the tissue, indicating that the cutting and friction forces acting on the protruding needle segment were higher than the friction forces on the retracting needle segments (Eq. 1). The tissue in front of the insertion hole used in the first measurement and more towards the lower side of the tissue box (Figs 31a,b) showed more tissue inhomogeneities than the tissue in front of the other insertion holes used in the experiment. The tissue sample used in this study was half of a slice of the prostate, which means that one side of the prostate tissue sample resembles the outer part of the prostate and the other side resembles the inner part of the prostate. The lower side of the tissue sample resembles the outer part of the prostate and the upper side the inner part of the prostate. Anatomically, the prostate is surrounded by more muscular and fibrous tissue that results in a lower signal intensity in the MR image [71]. The presence of the more muscular and fibrous tissue in the outer part of the prostate explains

the tissue inhomogeneities and the lower signal intensity in the MR image on the lower side of the tissue. Furthermore, in the first measurement, the needle was aligned in front of the outer part of the prostate sample with more muscular and fibrous tissue, which is more difficult to penetrate than the softer inner tissue. This explains why the needle was not able to penetrate the tissue in the first measurement.

After the second measurement, we could see that the needle had deformed the tissue by pushing to tissue forward. At the place where the needle entered the tissue, an image void appeared in the MR image for the second, third, and fourth measurement. This could be explained by the effect that the needle first compresses the tissue before entering the tissue. Compressing of the tissue resulted in air filling up the vacant space, which causes a signal void in the MR image.

In the third measurement, the needle moved below the tissue instead of propelling through the tissue (Figs 31f,g). The low slip ratio is likely to be caused by the low cutting force as the needle moved below the tissue, so it did not have to cut the tissue to propel through it.

The slip ratio of our needle in *ex vivo* prostate tissue is comparable to the slip ratio of the self-propelling needle developed by Scali [21] tested in *ex vivo* porcine tissue. Scali reported a slip ratio in the range of 0.87-0.90 for the continuously-moving needle in *ex vivo* porcine liver tissue [21]. We measured a slip ratio in the range of 0.86-0.96. The 2.5 wt% agar might have caused the high slip ratio for the second, fourth, and fifth measurement. Retraction of the rigid needle caused air to enter the track. The agar barely reformed into its initial shape after making a needle track with a rigid needle. When inserting the needle prototype, the needle might not have been able to generate enough friction in the track to propel itself because the formed track prevented the needle from touching the surrounding agar. Furthermore, the needle segments diverged during the experiment. Divergence of the needle segments increased the cutting force and thus, the slip ratio of the needle.

6. Discussion

6.1 Limitations

6.1.1 Limitations of the prototype

The clearance between the cam's V-shaped slot and the needle segment holders was set to 0.4 mm to allow the cam to rotate smoothly. The clearance causes the output stroke of the needle segments to deviate from the 4 mm cam-track stroke. The output stroke ranges from 3.6 to 4.4 mm.

In the Ovipositor MRI-Needle, we used the Dental Model V2 photopolymer resin (Formlabs) developed for creating crown and bridge dental models with high precision and accuracy. The use of the resin helped in the prototyping phase to print the internal components of the actuation and steering unit with high precision and accuracy. Biocompatible resins that are compatible with standard solvent disinfection and sterilisation methods, fulfilling design requirement 16, are also provided by Formlabs, e.g. BioMed Amber resin. However, the lowest possible print resolution is 50 μm for BioMed Amber resin, compared to 25 μm for Dental Model V2 resin, currently.

The needle segments were designed and sharpened in such a way that the needle segments point towards the middle (Fig. 32a). However, in the assembled prototype, the needle segments did not point towards the middle (Fig. 32b), which might have caused the needle segments to diverge and allow accumulation of tissue between the needle segments. Moreover, rotation of the needle segments is likely to be caused by misalignment of the needle segments

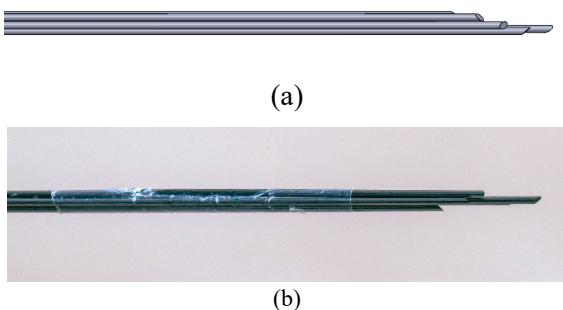


Fig. 32. Comparison of (a) an illustration of the designed configuration of the sharpened needle segments that point towards the middle and (b) a photograph of the configuration of the sharpened needle segments that do not point towards the middle in the assembled prototype.

along the length of the needle. Accumulation of tissue inside the shrinking tube might have caused the needle segments to stick to the shrinking tube, hindering the needle segments' protruding and retracting motions, thereby increasing the slip ratio of the needle.

The shrinking tube was placed almost at the tip of the needle, but when the remaining needle segments protruded, they advanced with respect to the shrinking tube, causing a larger part of the tip to protrude without the support of the shrinking tube. An increased length of the unsupported part increases the chance of the needle segments diverging and therefore of tissue accumulation between the needle segments.

6.1.2 Limitations of the experiment

The cam's V-shaped slot combined with the needle segments of equal length creates a constant needle segment offset at the tip, hence a variation on the bevel-shaped tip. Fig. 33 shows an illustration of the variation on the bevel-shaped tip caused by the cam. During the insertion of the needle to the initial insertion depth, the variation on the bevel-shaped tip results in a curved insertion, instead of a straight insertion. During the experiment, a rigid insertion tool (i.e., a needle with a sharp tip) was used to create a needle path to assist a straight initial insertion of the needle.

When the needle segment that is glued to the 10-mm long shrinking tube protrudes, the friction force of the protruding needle segment is increased compared to when one of the other needle segments protrudes, because of the surface area of the shrinking tube. Therefore, the initial insertion depth in the *ex vivo* tissue performance evaluation was set to 40 mm, to ensure the surface area of the protruding needle segment was less than the surface area of the retracting needle segments throughout the entire cycle. The initial manual insertion of 40 mm



Fig. 33. Illustration of the variation on the bevel-shaped tip caused by the cam.

inside the agar placed in front of the prostate tissue left 50 mm for evaluation of the needle motion. To increase the friction of the retracting needle segments, a microtextured directional surface topography could be added to the needle surface, as shown by Parittotokkaporn et al. [72].

In the experiment setup, the part of the needle that did not enter the tissue box was supported by a needle guide tube. The length of the tube is a trade-off between a long tube to prevent needle buckling and a short tube to allow a deep insertion of the needle into the tissue. A telescopic tube system with an adjustable length would overcome this trade-off issue. For future experiments, we would recommend using an MR-safe telescopic tube system to prevent buckling over a long length and allow for deep insertion of the needle.

In the MR images (Figs 31,34), the sides of the tissue box, which were straight in reality, seem curved, caused by the field inhomogeneities of the magnetic field. When using the far off-centre insertion holes of the tissue box, the shape of the needle in the MR image was affected more by the field inhomogeneities, than when using the central insertion hole centrally aligned in the RF coil. The field inhomogeneities caused the straight needle to show up bent in the MR images (Fig. 34). However, the position on the z-axis of the needle visualised in the MR image seemed unaffected by the field inhomogeneities, as the left and right sides of the box show up straight in the MR images (Fig. 31) Therefore, we assumed the measured distance of the needle to be unaffected by the field inhomogeneities.

In the experiment, we did not evaluate the steering performance in prostate tissue. The steering can be quantitatively evaluated using the radius of curvature of a circle fitted to the needle centreline or the ratio of needle deflection from the straight path to the insertion depth [29]. Future experiments should investigate the steering curvature that can be achieved in prostate tissue and whether this meets the requirements for the application in transperineal focal laser ablation. The maximum targeting error for prostate cancer treatment is 2.5 mm, based on the smallest clinically significant prostate tumour in pathology with a diameter of 5 mm [73]. To reach the target location inside the

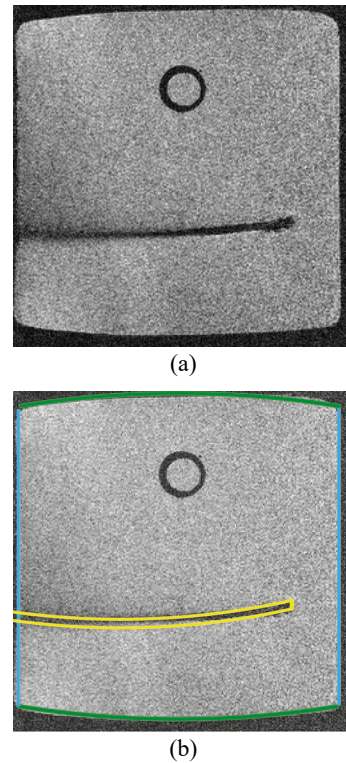


Fig. 34. MR image that shows the field inhomogeneities that cause the needle to show up bent in the image when using the far off-centre insertion holes of the tissue box. The lower and upper sides of the box show up bent in the MR image, however the left and right sides of the box show up straight in the MR image. The circle was used as a reference point to measure the insertion depth. (a) The original MR image. (b) The adjusted MR image. Yellow, green, and blue contours show the needle, the upper and lower sides of the box, and the left and right sides of the box, respectively.

prostate while avoiding the needle to touch the urethra, anterior wall of the rectum, and pelvic sidewall and compensating for the error introduced by the needle, the tissue-interaction forces, and extrinsically induced motion of the prostate, Moreira et al. [14] determined a required needle curvature of 0.015 cm^{-1} for prostate cancer biopsy.

6.2 Future work

6.2.1 Pneumatic actuation

In this work, we focused on locally advancing the six needle segments in a reciprocating motion with a discrete translating motion as the input. The input motion is induced by manually translating a ring that interacts with the selector. Our future work will focus on replacing the manual translation ring by annular bellows for pneumatic actuation of the needle motion. An

airtight bellows sample was fabricated using an SLA 3D printer (Formlabs Form 3B) and Durable resin (Formlabs). The bellows were printed with a 0.4-mm wall thickness in order to remain flexible (Fig. 35). The bellows were designed and printed as one part, with a locally increased wall thickness at the inner folds to help the bellows maintain their annular shape during contraction. The bellows were printed in their extended state and designed to contract when negative pressure is applied. Fig. 35b shows that in the under-vacuum state, the bellows did not maintain their annular shape. Further research will extend on how to adjust the bellows shape in order for the bellows to maintain their annular shape during contraction. Besides the bellows, the housing and the selector need to be replaced by an adapted version to fit with the bellows (Fig. 36). More information about the iterative design process for the bellows and the pneumatic actuation unit design for the Ovipositor MRI-Needle can be found in Appendices K and L.

6.2.2 Phantom studies

In this study, we evaluated the performance of the Ovipositor MRI-Needle in a single prostate

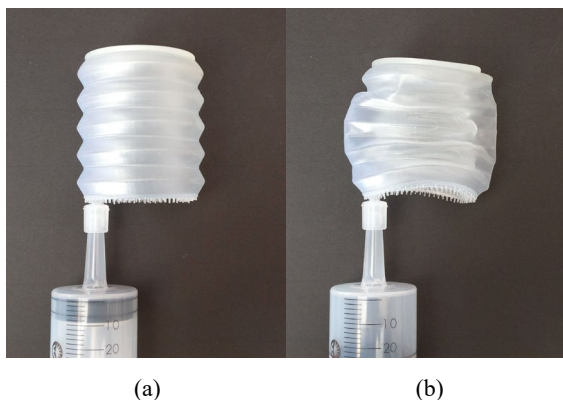


Fig. 35. Photographs of 3D-printed airtight annular bellows (a) in its neutral state and (b) in its under-vacuum state.

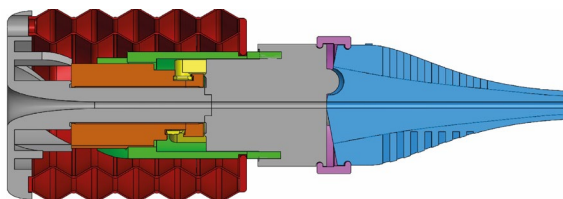


Fig. 36. Illustration of the cross-section of the assembly of the pneumatic actuation unit, including the bellows (in red), housing (in grey), and selector (in green).

sample. The mechanical properties of the prostate tissue of different men are not the same but comprise ranges of values. To ensure the Ovipositor MRI-Needle can self-propel through prostate tissue in all men, the Ovipositor MRI-Needle should be tested in more than one prostate sample. Because of the limited availability of *ex vivo* prostate tissue, a high-fidelity prostate phantom is essential for a larger study size. It is important to know the requirements for the phantom to decide on the type of phantom. The use of cadavers and meat phantoms often introduces issues for reasons such as cost, availability, and safety [74]. In the scientific literature, the main focus has been on developing phantoms with optical properties in the range of the optical properties of biological tissues [75-77]. For needle insertion tests, mechanical properties like friction, stiffness, and relaxation are important [78]. Gelatine is often used as a tissue-mimicking phantom, as it is easy to use and the stiffness can be controlled by changing the gelatine concentration [79]. Zhang et al. [80] reported a Young modulus for normal prostate tissue of 15.9 ± 5.9 kPa (n=8), at 150 Hz using stress relaxation tests. Barr et al. [81] reported a Young modulus for benign prostate tissue of 21.5 ± 11.5 kPa (n=242). The Young's modulus of 10 wt% gelatine is 17 kPa [32], which is in the same range as the Young modulus of normal prostate tissue. However, gelatine has a homogeneous and isotropic structure, whereas biological tissue is heterogeneous and anisotropic [21]. Biological phantoms like fruits and vegetables show a heterogeneous and anisotropic structure like meat phantoms and cadavers, and often do not introduce cost, availability, and safety issues. For future research and testing of future needle prototypes, an easily available and safe tissue-mimicking phantom based on the mechanical properties of prostate tissue would be useful.

6.2.3 Towards clinical use

Considering the needle's primary goal, the use in transperineal optical biopsy and focal laser ablation, the Ovipositor MRI-Needle poses challenges to the design for disposability of such an instrument. Design for disposable following design requirement 14 should be considered in future design iterations. The actuation and

steering unit contains ten parts produced using 3D printing technologies. Minimising the number of parts would ease the assembly process and make the device more suitable for low-cost disposable use. Furthermore, MR safety and compatibility of the components used should be addressed using the ASTM test methods described in F2503, F2502, F2213, and F2119. Radio frequency heating caused by the Nitinol needle should be evaluated experimentally, as the Nitinol needle is a long and electrically conductive structure that couples with the electric field of the RF coil in an MRI system [82]. The coupling induces high voltages at the end of the needle, which might cause heating of the surrounding tissue that poses a potential safety hazard to the patient [82, 83].

In this study, the actuation and steering unit was designed to be used in experiments where the *ex vivo* tissue was placed in a tissue box that moved towards the needle. To be applied in transperineal laser ablation, the needle will have to self-propel through the perineal skin and into the prostate, while the patient stays still inside the MRI-bore. The actuation and steering unit can be placed on a robotic arm to manipulate the needle towards the cancerous tissue. Future research should investigate the design adaptations to move the needle towards the target tissue, instead of moving the target tissue towards the needle.

In future versions of the Ovipositor MRI-Needle, the needle's tip should be sharper to decrease the cutting force, thus decreasing the slip and the tissue deformation. For the design of the needle's tip, the needles used for brachytherapy could be used as a design starting point. In brachytherapy, needles with a lancet point are used to minimise the insertion force [84].

After each measurement in the *ex vivo* prostate experiment, the needle was removed from the tissue. Fig. 37 shows the needle left a track behind in the agar. The track coloured red like the tissue fluid, indicating that retraction of the needle resulted in a trace of tissue fluid entering the track. In clinical practice, a trace of tissue fluid due to needle retraction might cause the dissemination of tumour cells into the needle track, which causes concern in the case of malignant tumours [85]. Subsequent sterilisation of the needle track can provide a solution to the cell dissemination in the needle track [85].

The MRI-ready, self-propelling, steerable needle is a platform technology that allows the positioning of a functional element in a target region in the body. One of the Nitinol needle segments can be replaced by a tube to inject a substance into the target region [32]. Another option is to place an MRI-ready optical laser fibre as the seventh needle segment in the centre with the six Nitinol needle segments around it,

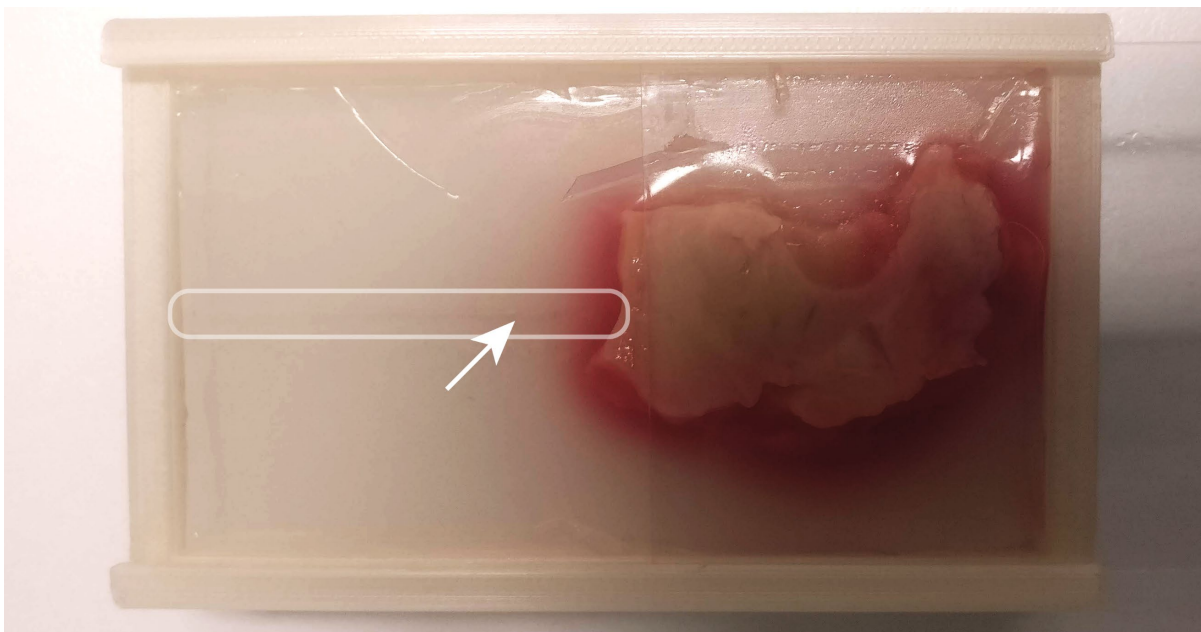


Fig. 37. Retraction of the needle left a trace of tissue fluid in the needle track in the *ex vivo* prostate tissue experiment.

forming a circle. The optical laser fibre allows the needle to be used for optical biopsy and focal laser ablation to treat prostate cancer. For focal laser ablation, the tip of the optical laser fibre reaches a temperature of approximately 90°C [55, 56]. Shape memory loss might occur when Nitinol is heated above a critical temperature [86]. Furthermore, the shrinking tube (Vention Medical) shrink temperature ranges from 85°C to 190°C, and its melt temperature is 235°C [87]. Shrinking or melting of the shrinking tube is undesirable in our design. The shrinking tube is glued to one needle segment using a cyanoacrylate-based glue. The temperature behaviour of the straight annealed Nitinol needle, the shrinking tube, and the glue should be investigated to assess their suitability in combination with optical laser fibres, conform design requirement 15.

Systems to enhance the visualisation of the needle tip's position under MRI guidance can be integrated into the needle's design. In this study, passive needle tracking was used. Passive tracking of the Nitinol needle can be enhanced by replacing the needle or needle tip by a tip composed of a material with a lower magnetic susceptibility than Nitinol, as presented by Al-Maatoq et al. [63, 88]. Another method to enhance the visualisation of the needle tip's position inside the tissue under MRI-guidance is active tracking. Active instruments with embedded RF coils or other sensors can generate conspicuous signals for localisation of the instrument [89]. Advantages of active tracking methods over passive ones are the high temporal and spatial resolution of the information generated, leading to shorter procedure times and improved procedure outcome [89]. Furthermore, when the needle produces image artefacts, precise determination of the needle position using passive methods is challenging [90]. Thus active tracking methods using embedded RF coils or other sensors can improve the needle-tip localisation.

Another option is using fibre Bragg grating on the optical fibre to detect the shape of the optical fibre at the core of the needle [91]. An advantage of fibre Bragg gratings over RF coils is that the optical fibre might already be part of the functionalised needle. Hence, no additional components would be required: the optical fibres

only need grating to enable shape reconstruction [92]. The wavelengths that satisfy the Bragg condition of the grating are back-reflected [93, 94]. The peak wavelength shifts in proportion to the strain of the fibre, which enables strain sensing and therefore shape reconstruction and position measurement [93, 94]. Park et al. [93] showed that the application of optical fibres with embedded fibre Bragg grating sensors inside an MRI system did not produce any image artefacts. Moreira et al. [94] developed a Nitinol needle embedded with fibre Bragg grating sensors that enable the localisation of the needle tip position in MR images. Experiments showed that the operator could reach the target with an error of 1.74 mm [94]. The application of fibre Bragg grating in the needle functionalised with an optical fibre might be a space-efficient option to improve needle-tip localisation.

7. Conclusion

In this work, we have presented the design and experimental validation of a self-propelling needle with an MRI-ready actuation system. We have shown that a discrete manual translating motion can actuate the reciprocating motion of the six parallel needle segments using a rotational selector inspired by the click-pen mechanism. A global system allows steering of the needle by shifting the needle segment tips to approximate a bevel-shaped tip. A continuous hollow core through the actuation and steering unit allows for needle functionalisation with an optical fibre for optical biopsy and focal laser ablation. The prototype's components, excluding the needle, are easy to manufacture by 3D printing using MR-safe materials solely. The needle consists of six sharpened Nitinol rods. It was possible to determine the needle tip's position in the MR image, as the Nitinol needle did not cause large image artefacts. The evaluation of the prototype, in *ex vivo* human prostate tissue in an MRI scanner, showed the needle could self-propel through the tissue in three out of five measurements. The prototype is a step forward in developing a self-propelling needle for MRI-guided transperineal focal laser ablation to treat prostate cancer.

Acknowledgements

We would like to thank David Jager from DEMO (Dienst Elektronische en Mechanische Ontwikkeling) at the TU Delft for sharpening the needle segments and Luigi van Riel, Gustav Strijkers, Bram Coolen, Martijn de Bruin, and Theo de Reijke from the AUMC (Amsterdam University Medical Centers) for the discussions about the application of the project in focal laser ablation for prostate cancer treatment and their help in designing the setup and performing the experiment.

References

- [1] E. N. Marieb and K. Hoehn, *Human anatomy & physiology*, Tenth edition ed. Pearson education, 2016.
- [2] P. Verze, T. Cai, and S. Lorenzetti, "The role of the prostate in male fertility, health and disease," *Nature Reviews Urology*, vol. 13, no. 7, p. 379, 2016.
- [3] F. Bray, J. Ferlay, I. Soerjomataram, R. L. Siegel, L. A. Torre, and A. Jemal, "Global cancer statistics 2018: GLOBOCAN estimates of incidence and mortality worldwide for 36 cancers in 185 countries," *CA: a cancer journal for clinicians*, vol. 68, no. 6, pp. 394-424, 2018.
- [4] P. Rawla, "Epidemiology of prostate cancer," *World journal of oncology*, vol. 10, no. 2, p. 63, 2019.
- [5] F. C. Hamdy *et al.*, "10-year outcomes after monitoring, surgery, or radiotherapy for localized prostate cancer," *N Engl J Med*, vol. 375, pp. 1415-1424, Oct. 2016.
- [6] O. Lodeizen *et al.*, "Ablation energies for focal treatment of prostate cancer," *World journal of urology*, vol. 37, no. 3, pp. 409-418, Mar. 2019.
- [7] A. Oto *et al.*, "MR imaging-guided focal laser ablation for prostate cancer: phase I trial," *Radiology*, vol. 267, no. 3, pp. 932-940, 2013.
- [8] P. Colin *et al.*, "Focal laser ablation of prostate cancer: definition, needs, and future," *Advances in urology*, vol. 2012, 2012.
- [9] K. K. Hodge, J. E. McNeal, and T. A. Stamey, "Ultrasound guided transrectal core biopsies of the palpably abnormal prostate," *The Journal of urology*, vol. 142, no. 1, pp. 66-70, 1989.
- [10] A. de la Taille *et al.*, "Prospective evaluation of a 21-sample needle biopsy procedure designed to improve the prostate cancer detection rate," *Urology*, vol. 61, no. 6, pp. 1181-1186, 2003.
- [11] G. Patelli, A. Ranieri, A. Paganelli, G. Mauri, and C. M. Pacella, "Transperineal laser ablation for percutaneous treatment of benign prostatic hyperplasia: a feasibility study," *Cardiovascular and interventional radiology*, vol. 40, no. 9, pp. 1440-1446, 2017.
- [12] A. Leibinger, M. J. Oldfield, and F. Rodriguez y Baena, "Minimally disruptive needle insertion: a biologically inspired solution," *Interface focus*, vol. 6, no. 3, p. 20150107, 2016.
- [13] R. M. Wright and K. Ramesh, "An axonal strain injury criterion for traumatic brain injury," *Biomechanics and modeling in mechanobiology*, vol. 11, no. 1-2, pp. 245-260, 2012.
- [14] P. Moreira *et al.*, "The miriam robot: A novel robotic system for mr-guided needle insertion in the prostate," *Journal of medical robotics research*, vol. 2, no. 04, p. 1750006, 2017.
- [15] S. P. DiMaio and S. E. Salcudean, "Needle insertion modeling and simulation," *IEEE Transactions on robotics and automation*, vol. 19, no. 5, pp. 864-875, 2003.
- [16] A. Sakes, D. Dodou, and P. Breedveld, "Buckling prevention strategies in nature as inspiration for improving percutaneous instruments: a review," *Bioinspiration & biomimetics*, vol. 11, no. 2, p. 021001, 2016.
- [17] N. Abolhassani, R. Patel, and M. Moallem, "Needle insertion into soft tissue: A survey," *Medical engineering & physics*, vol. 29, no. 4, pp. 413-431, 2007.
- [18] N. Abolhassani, R. V. Patel, and F. Ayazi, "Minimization of needle deflection in robot-assisted percutaneous therapy," *The international journal of medical Robotics and computer assisted surgery*, vol. 3, no. 2, pp. 140-148, 2007.
- [19] L. Frasson, F. Ferroni, S. Y. Ko, G. Dogangil, and F. R. y Baena, "Experimental evaluation of a novel steerable probe with a programmable bevel tip inspired by nature," *Journal of robotic surgery*, vol. 6, no. 3, pp. 189-197, 2012.
- [20] V. Viridyawan, M. Oldfield, and F. R. y Baena, "Laser Doppler sensing for blood vessel detection with a biologically inspired steerable needle," *Bioinspiration & biomimetics*, vol. 13, no. 2, p. 026009, 2018.
- [21] M. Scali, "Self-propelling needles: From biological inspiration to percutaneous interventions," 2020.
- [22] U. Cerkvėnik, B. Van de Straat, S. W. Gussekloo, and J. L. Van Leeuwen, "Mechanisms of ovipositor insertion and steering of a parasitic wasp," *Proceedings of the National Academy of Sciences*, vol. 114, no. 37, pp. E7822-E7831, 2017.

- [23] D. L. Quicke and M. G. Fitton, "Ovipositor steering mechanisms in parasitic wasps of the families Gasteruptionidae and Aulacidae (Hymenoptera)," *Proceedings of the Royal Society of London. Series B: Biological Sciences*, vol. 261, no. 1360, pp. 99-103, 1995.
- [24] L. Vilhelmsen, N. Isidoro, R. Romani, H. H. Basibuyuk, and D. L. Quicke, "Host location and oviposition in a basal group of parasitic wasps: the subgenual organ, ovipositor apparatus and associated structures in the Orussidae (Hymenoptera, Insecta)," *Zoomorphology*, vol. 121, no. 2, pp. 63-84, 2001.
- [25] D. Quicke, M. Fitton, J. Tunstead, S. Ingram, and P. Gaitens, "Ovipositor structure and relationships within the Hymenoptera, with special reference to the Ichneumonoidea," *Journal of Natural History*, vol. 28, no. 3, pp. 635-682, 1994.
- [26] D. Pollard, "Directional control of the stylets in phytophagous Hemiptera," in *Proceedings of the Royal Entomological Society of London. Series A, General Entomology*, 1969, vol. 44, no. 10-12: Wiley Online Library, pp. 173-185.
- [27] J. Vincent and M. King, "The mechanism of drilling by wood wasp ovipositors," *Biomimetics (USA)*, 1995.
- [28] T. Parittotokkaporn *et al.*, "Soft tissue traversal with zero net force: Feasibility study of a biologically inspired design based on reciprocal motion," in *2008 IEEE International Conference on Robotics and Biomimetics*, 2009: IEEE, pp. 80-85.
- [29] M. Scali, T. Pusch, P. Breedveld, and D. Dodou, "Ovipositor-inspired steerable needle: design and preliminary experimental evaluation," *Bioinspiration & Biomimetics*, vol. 13, no. 1, p. 016006, 2017.
- [30] L. Frasson, S. Ko, A. Turner, T. Parittotokkaporn, J. F. Vincent, and F. Rodriguez y Baena, "STING: a soft-tissue intervention and neurosurgical guide to access deep brain lesions through curved trajectories," *Proceedings of the Institution of Mechanical Engineers, Part H: Journal of Engineering in Medicine*, vol. 224, no. 6, pp. 775-788, 2010.
- [31] M. Scali. "Ovipositor needle II - Self-propelling & steering through tissue." <https://www.bitegroup.nl/category/maneuverable-devices/ovipositor-needle-ii/> (accessed January, 8, 2021).
- [32] M. Scali, P. Breedveld, and D. Dodou, "Experimental evaluation of a self-propelling bio-inspired needle in single-and multi-layered phantoms," *Scientific reports*, vol. 9, no. 1, pp. 1-13, 2019.
- [33] R. J. Stafford *et al.*, "Magnetic resonance guided, focal laser induced interstitial thermal therapy in a canine prostate model," *The Journal of urology*, vol. 184, no. 4, pp. 1514-1520, 2010.
- [34] U. Lindner *et al.*, "Focal laser ablation for prostate cancer followed by radical prostatectomy: validation of focal therapy and imaging accuracy," *European urology*, vol. 57, no. 6, pp. 1111-1114, 2010.
- [35] E. J. Blink, "mri: Physics," *Online PDF file*, pp. 0-75, 2004.
- [36] B. Quesson, J. A. de Zwart, and C. T. Moonen, "Magnetic resonance temperature imaging for guidance of thermotherapy," *Journal of Magnetic Resonance Imaging: An Official Journal of the International Society for Magnetic Resonance in Medicine*, vol. 12, no. 4, pp. 525-533, 2000.
- [37] B. Denis de Senneville, B. Quesson, and C. T. Moonen, "Magnetic resonance temperature imaging," *International Journal of Hyperthermia*, vol. 21, no. 6, pp. 515-531, 2005.
- [38] F. A. Jolesz, *Intraoperative imaging and image-guided therapy*. Springer Science & Business Media, 2014.
- [39] *ASTM F2503-13, Standard practice for marking medical devices and other items for safety in the magnetic resonance environment*, ASTM International, West Conshohocken, PA, 2013. [Online]. Available: www.astm.org
- [40] V. Groenhuis and S. Stramigioli, "Rapid prototyping high-performance MR safe pneumatic stepper motors," *IEEE/ASME transactions on mechatronics*, vol. 23, no. 4, pp. 1843-1853, 2018.
- [41] V. Groenhuis, F. J. Siepel, and S. Stramigioli, "Sunram 5: A Magnetic Resonance-Safe Robotic System for Breast Biopsy, Driven by Pneumatic Stepper Motors," in *Handbook of Robotic and Image-Guided Surgery*: Elsevier, 2020, pp. 375-396.
- [42] Y. Chen, I. Godage, H. Su, A. Song, and H. Yu, "Stereotactic systems for MRI-guided neurosurgeries: A state-of-the-art review," *Annals of biomedical engineering*, vol. 47, no. 2, pp. 335-353, 2019.
- [43] V. Groenhuis and S. Stramigioli, "Laser-cutting pneumatics," *IEEE/ASME transactions on mechatronics*, vol. 21, no. 3, pp. 1604-1611, 2015.
- [44] H. Sajima, H. Kamiuchi, K. Kuwana, T. Dohi, and K. Masamune, "MR-safe pneumatic rotation stepping actuator," *Journal of Robotics and Mechatronics*, vol. 24, no. 5, pp. 820-827, 2012.
- [45] L. Phee *et al.*, "Ultrasound guided robotic system for transperineal biopsy of the prostate," in *Proceedings of the 2005 IEEE international conference on robotics and automation*, 2005: IEEE, pp. 1315-1320.

- [46] T. P. Pusch, "From the wasp ovipositor to a 3D steerable needle for solid-tissue interventions," 2016.
- [47] U. Lindner, N. Lawrentschuk, and J. Trachtenberg, "Focal laser ablation for localized prostate cancer," *Journal of Endourology*, vol. 24, no. 5, pp. 791-797, 2010.
- [48] A. Swaan *et al.*, "Confocal laser endomicroscopy and optical coherence tomography for the diagnosis of prostate cancer: A needle-based, in vivo feasibility study protocol (Ideal phase 2a)," 2018.
- [49] *ASTM F2119-07(2013), Standard Test Method for Evaluation of MR Image Artifacts from Passive Implants*, ASTM International, West Conshohocken, PA, 2013. [Online]. Available: www.astm.org
- [50] C. Culmone, G. Smit, and P. Breedveld, "Additive manufacturing of medical instruments: A state-of-the-art review," *Additive Manufacturing*, vol. 27, pp. 461-473, 2019.
- [51] J. M. Walker, D. A. Elliott, C. D. Kubicky, C. R. Thomas Jr, and A. M. Naik, "Manufacture and evaluation of 3-dimensional printed sizing tools for use during intraoperative breast brachytherapy," *Advances in radiation oncology*, vol. 1, no. 2, pp. 132-135, 2016.
- [52] A. Gangi, H. Alizadeh, L. Wong, X. Buy, J.-L. Dietemann, and C. Roy, "Osteoid osteoma: percutaneous laser ablation and follow-up in 114 patients," *Radiology*, vol. 242, no. 1, pp. 293-301, 2007.
- [53] M. Johnson *et al.*, "Fabricating biomedical origami: A state-of-the-art review," *International journal of computer assisted radiology and surgery*, vol. 12, no. 11, pp. 2023-2032, 2017.
- [54] Y. Zhao, B. Zhu, Y. Wang, C. Liu, and C. Shen, "Effect of different sterilization methods on the properties of commercial biodegradable polyesters for single-use, disposable medical devices," *Materials Science and Engineering: C*, vol. 105, p. 110041, 2019.
- [55] S. Natarajan *et al.*, "Focal laser ablation of prostate cancer: phase I clinical trial," *The Journal of urology*, vol. 196, no. 1, pp. 68-75, 2016.
- [56] M.-F. Marqa, P. Colin, P. Nevoux, S. R. Mordon, and N. Betrouni, "Focal laser ablation of prostate cancer: numerical simulation of temperature and damage distribution," *Biomedical engineering online*, vol. 10, no. 1, p. 45, 2011.
- [57] R. N. Kent, "Writing instrument," Patent US3205863A, 1953.
- [58] M. Scali, T. P. Pusch, P. Breedveld, and D. Dodou, "Needle-like instruments for steering through solid organs: A review of the scientific and patent literature," *Proceedings of the Institution of Mechanical Engineers, Part H: Journal of Engineering in Medicine*, vol. 231, no. 3, pp. 250-265, 2017.
- [59] P. Breedveld. "I-Flex - Steering towards miniaturization limits." <https://www.bitegroup.nl/category/maneuverable-devices/i-flex/> (accessed 10 Nov., 2020).
- [60] C. Culmone, P. W. Henselmans, R. I. van Starkenburg, and P. Breedveld, "Exploring non-assembly 3D printing for novel compliant surgical devices," *Plos one*, vol. 15, no. 5, p. e0232952, 2020.
- [61] Y.-H. Kim, M. Choi, and J.-W. Kim, "Are titanium implants actually safe for magnetic resonance imaging examinations?," *Archives of plastic surgery*, vol. 46, no. 1, p. 96, 2019.
- [62] D. Stöckel, "Nitinol-A material with unusual properties," *Endovascular Update*, vol. 1, no. 1, pp. 1-8, 1998.
- [63] M. Al-Maatoq, A. Boese, H.-W. Henke, and M. Friebe, "Primary Design Concept for Non-metallic Needle for MRI Guided Spinal Applications," in *2019 41st Annual International Conference of the IEEE Engineering in Medicine and Biology Society (EMBC)*, 2019: IEEE, pp. 1994-1997.
- [64] C. Barras and K. Myers, "Nitinol—its use in vascular surgery and other applications," *European Journal of Vascular and Endovascular Surgery*, vol. 19, no. 6, pp. 564-569, 2000.
- [65] A. Melzer, S. Michitsch, S. Konak, G. Schaefer, and T. Bertsch, "Nitinol in magnetic resonance imaging," *Minimally Invasive Therapy & Allied Technologies*, vol. 13, no. 4, pp. 261-271, 2004.
- [66] T. Kahn and H. Busse, *Interventional magnetic resonance imaging*. Springer, 2012.
- [67] W. Jamróz, J. Szafraniec, M. Kurek, and R. Jachowicz, "3D printing in pharmaceutical and medical applications—recent achievements and challenges," *Pharmaceutical research*, vol. 35, no. 9, p. 176, 2018.
- [68] P. Ciet *et al.*, "Magnetic resonance imaging in children: common problems and possible solutions for lung and airways imaging," *Pediatric radiology*, vol. 45, no. 13, pp. 1901-1915, 2015.
- [69] M. E. Ladd, P. Erhart, J. F. Debatin, B. J. Romanowski, P. Boesiger, and G. C. McKinnon, "Biopsy needle susceptibility artifacts," *Magnetic resonance in medicine*, vol. 36, no. 4, pp. 646-651, 1996.
- [70] J. M. Korde and B. Kandasubramanian, "Biocompatible alkyl cyanoacrylates and their derivatives as bio-adhesives," *Biomaterials science*, vol. 6, no. 7, pp. 1691-1711, 2018.
- [71] H. Hricak *et al.*, "MR imaging of the prostate gland: normal anatomy," *American journal of*

- roentgenology, vol. 148, no. 1, pp. 51-58, 1987.
- [72] T. Parittotokkaporn, L. Frasson, A. Schneider, B. Davies, P. Degenaar, and F. R. y Baena, "Insertion experiments of a biologically inspired microtextured and multi-part probe based on reciprocal motion," in *2010 Annual International Conference of the IEEE Engineering in Medicine and Biology*, 2010: IEEE, pp. 3190-3193.
- [73] T. A. Stamey, F. S. Freiha, J. E. McNeal, E. A. Redwine, A. S. Whittemore, and H. P. Schmid, "Localized prostate cancer. Relationship of tumor volume to clinical significance for treatment of prostate cancer," *Cancer*, vol. 71, no. S3, pp. 933-938, 1993.
- [74] Z. Khashei Varnamkhasti, B. Konh, O. Haji Maghsoudi, Y. Yu, and L. Liao, "Ultrasound Needle Tracking Inside a Soft Phantom and Methods to Improve the Needle Tip Visualization," in *Frontiers in Biomedical Devices*, 2019, vol. 41037: American Society of Mechanical Engineers, p. V001T06A012.
- [75] G. Lamouche *et al.*, "Review of tissue simulating phantoms with controllable optical, mechanical and structural properties for use in optical coherence tomography," *Biomedical optics express*, vol. 3, no. 6, pp. 1381-1398, 2012.
- [76] U. G. Mueller-Lisse, S. Murer, U. L. Mueller-Lisse, M. Kuhn, J. Scheidler, and M. Scherr, "Everyman's prostate phantom: kiwi-fruit substitute for human prostates at magnetic resonance imaging, diffusion-weighted imaging and magnetic resonance spectroscopy," *European Radiology*, vol. 27, no. 8, pp. 3362-3371, 2017.
- [77] M. Larrison, A. DiBona, and D. E. Hogg, "Low-cost phantom for stereotactic breast biopsy training," *American Journal of Roentgenology*, vol. 187, no. 4, pp. 972-974, 2006.
- [78] T. R. Wedlick and A. M. Okamura, "Characterization of robotic needle insertion and rotation in artificial and ex vivo tissues," in *2012 4th IEEE RAS & EMBS International Conference on Biomedical Robotics and Biomechatronics (BioRob)*, 2012: IEEE, pp. 62-68.
- [79] G. Hocking, S. Hebard, and C. H. Mitchell, "A review of the benefits and pitfalls of phantoms in ultrasound-guided regional anesthesia," *Regional Anesthesia & Pain Medicine*, vol. 36, no. 2, pp. 162-170-162-170, 2011.
- [80] M. Zhang *et al.*, "Quantitative characterization of viscoelastic properties of human prostate correlated with histology," *Ultrasound in medicine & biology*, vol. 34, no. 7, pp. 1033-1042, 2008.
- [81] R. G. Barr, R. Memo, and C. R. Schaub, "Shear wave ultrasound elastography of the prostate: initial results," *Ultrasound quarterly*, vol. 28, no. 1, pp. 13-20, 2012.
- [82] W. R. Nitz, A. Oppelt, W. Renz, C. Manke, M. Lenhart, and J. Link, "On the heating of linear conductive structures as guide wires and catheters in interventional MRI," *Journal of Magnetic Resonance Imaging*, vol. 13, no. 1, pp. 105-114, 2001.
- [83] M. K. Konings, L. W. Bartels, H. F. Smits, and C. J. Bakker, "Heating around intravascular guidewires by resonating RF waves," *Journal of Magnetic Resonance Imaging*, vol. 12, no. 1, pp. 79-85, 2000.
- [84] Y. Wang, R. K. Chen, B. L. Tai, P. W. McLaughlin, and A. J. Shih, "Optimal needle design for minimal insertion force and bevel length," *Medical engineering & physics*, vol. 36, no. 9, pp. 1093-1100, 2014.
- [85] H. Wiksell *et al.*, "Prevention of tumour cell dissemination in diagnostic needle procedures," *British journal of cancer*, vol. 103, no. 11, pp. 1706-1709, 2010.
- [86] A. A. Adeleke and Y. Yao, "High-temperature shape memory loss in nitinol: a first principles study," *Physical Chemistry Chemical Physics*, vol. 21, no. 14, pp. 7508-7517, 2019.
- [87] M. Saab, "Using Thin-Wall Heat-Shrink Tubing in Medical Device Manufacturing," *Medical device and diagnostic industry*, vol. 21, pp. 54-62, 1999.
- [88] M. Al-Maatoq, J. W. Krug, and M. H. Friebe, "The tip is the key-rfa needle modification using peek for reduced susceptibility artifact in mri," 2015.
- [89] W. Wang, "Magnetic resonance-guided active catheter tracking," *Magnetic Resonance Imaging Clinics*, vol. 23, no. 4, pp. 579-589, 2015.
- [90] S. P. DiMaio *et al.*, "Needle artifact localization in 3T MR images," *Medicine Meets Virtual Reality 14: Accelerating Change in Healthcare: Next Medical Toolkit*, vol. 119, p. 120, 2006.
- [91] Y. Park *et al.*, "MRI-compatible Haptics: Feasibility of using optical fiber Bragg grating strain-sensors to detect deflection of needles in an MRI environment," *International Society for Magnetic Resonance in Medicine (ISMRM) 2008*, 2008.
- [92] R. Secoli, M. Robinson, M. Brugnoli, and F. Rodriguez y Baena, "A low-cost, high-field-strength magnetic resonance imaging-compatible actuator," *Proceedings of the Institution of Mechanical Engineers, Part H: Journal of Engineering in Medicine*, vol. 229, no. 3, pp. 215-224, 2015.
- [93] Y. Park *et al.*, "MRI-compatible Haptics: Strain sensing for real-time estimation of three

- dimensional needle deflection in MRI environments," in *International Society for Magnetic Resonance in Medicine (ISMRM), 17th Scientific Meeting and Exhibition*, 2009.
- [94] P. Moreira, K. J. Boskma, and S. Misra, "Towards MRI-guided flexible needle steering using fiber Bragg grating-based tip tracking," in *2017 IEEE International Conference on Robotics and Automation (ICRA)*, 2017: IEEE, pp. 4849-4854.
- [95] D. Stoianovici, A. Patriciu, D. Petrisor, D. Mazilu, and L. Kavoussi, "A new type of motor: pneumatic step motor," *IEEE/ASME Transactions On Mechatronics*, vol. 12, no. 1, pp. 98-106, 2007.
- [96] Y. Chen, C. D. Mershon, and Z. T. H. Tse, "A 10-mm MR-conditional unidirectional pneumatic stepper motor," *IEEE/ASME Transactions on Mechatronics*, vol. 20, no. 2, pp. 782-788, 2014.
- [97] Z. Guo, T. Lun, Y. Chen, H. Su, D. Chan, and K. Kwok, "Novel design of an MR-safe pneumatic stepper motor for MRI-guided robotic interventions," in *Proceedings of The Hamlyn Symposium on Medical Robotics*, 2016: Imperial College London and the Royal Geographical Society London. The Conference Proceedings' website is located at <http://hamlyn.doc.ic.ac.uk/hsmr/programme/symposium-proceedings>., pp. 25-28.
- [98] B. L. Boland, S. Xu, B. Wood, and Z. T. H. Tse, "High speed pneumatic stepper motor for mri applications," *Annals of biomedical engineering*, vol. 47, no. 3, pp. 826-835, 2019.
- [99] J. Bomers, D. Bosboom, G. Tigelaar, J. Sabisch, J. Fütterer, and D. Yakar, "Feasibility of a 2 nd generation MR-compatible manipulator for transrectal prostate biopsy guidance," *European radiology*, vol. 27, no. 4, pp. 1776-1782, 2017.
- [100] D. Stoianovici, D. Petrisor, C. Kim, and P. Sebrechts, "MRI-safe robot for transrectal prostate biopsy," Patent US9877788B2, 2013.
- [101] V. Groenhuis, F. J. Siepel, and S. Stramigioli, "Pneumatic stepper motor and device comprising at least one such pneumatic stepper motor " Patent US20200182267A1, 2017.
- [102] D. B. Comber, J. E. Slightam, V. R. Gervasi, J. S. Neimat, and E. J. Barth, "Design, additive manufacture, and control of a pneumatic MR-compatible needle driver," *IEEE Transactions on Robotics*, vol. 32, no. 1, pp. 138-149, 2016.
- [103] D. B. Comber, E. J. Barth, J. E. Slightam, and V. R. Gervasi, "Apparatus and method for moving an elongate rod," Patent US10321963B2, 2016.
- [104] T. P. Pusch, "From the wasp ovipositor to a 3d steerable needle for solid-tissue interventions - A design and experimental approach.," Master of Science, Mechanical Engineering, TU Delft, 2016.
- [105] M. Scali, P. A. Veldhoven, P. W. Henselmans, D. Dodou, and P. Breedveld, "Design of an ultra-thin steerable probe for percutaneous interventions and preliminary evaluation in a gelatine phantom," *PloS one*, vol. 14, no. 9, p. e0221165, 2019.
- [106] E. P. de Kater, "The design of a flexible friction-based transport mechanism - A bio-inspired transport mechanism for tissue transport in minimal invasive medical interventions," Master of Science, Mechanical Engineering and Biomedical Engineering, TU Delft, 2020.
- [107] M. Scali, D. Kreeft, P. Breedveld, and D. Dodou, "Design and evaluation of a wasp-inspired steerable needle," in *Bioinspiration, Biomimetics, and Bioreplication 2017*, 2017, vol. 10162: International Society for Optics and Photonics, p. 1016207.
- [108] O. J. North, "Medical robotics for use in MRI guided endoscopy," 2013.
- [109] J. B. Hopkins and M. L. Culpepper, "Synthesis of multi-degree of freedom, parallel flexure system concepts via Freedom and Constraint Topology (FACT)–Part I: Principles," *Precision Engineering*, vol. 34, no. 2, pp. 259-270, 2010.
- [110] J. B. Hopkins and M. L. Culpepper, "Synthesis of multi-degree of freedom, parallel flexure system concepts via freedom and constraint topology (FACT). Part II: Practice," *Precision Engineering*, vol. 34, no. 2, pp. 271-278, 2010.
- [111] "Using Durable Resin." Formlabs. https://support.formlabs.com/s/article/Using-Durable-Resin?language=en_US (accessed Sept. 9, 2020).
- [112] M. S. Choudhury, M. Jain, and S. L. Shah, "Stiction—definition, modelling, detection and quantification," *Journal of Process control*, vol. 18, no. 3-4, pp. 232-243, 2008.
- [113] A. Harnoy, B. Friedland, and S. Cohn, "Modeling and measuring friction effects," *IEEE Control Systems Magazine*, vol. 28, no. 6, pp. 82-91, 2008.
- [114] H. Zhang, "Surface characterization techniques for polyurethane biomaterials," in *Advances in polyurethane biomaterials*: Elsevier, 2016, pp. 23-73.
- [115] T. Cedorge and J. Colton, "Draft angle and surface roughness effects on stereolithography molds," *Polymer Engineering & Science*, vol. 40, no. 7, pp. 1581-1588, 2000.
- [116] M. Mahvash and P. E. Dupont, "Fast needle insertion to minimize tissue deformation and damage," in *2009 IEEE International Conference on Robotics and Automation*, 2009: IEEE, pp. 3097-3102.

- [117] E. Oberg, F. D. Jones, H. L. Horton, and H. H. Ryffel, *Machinery's handbook*, 30th edition ed. Industrial Press, 2016.
- [118] T. Penzkofer, N. Peykan, K. Schmidt, G. Krombach, and C. K. Kuhl, "How MRI compatible is "MRI compatible"? A systematic comparison of artifacts caused by biopsy needles at 3.0 and 1.5 T," *Cardiovascular and interventional radiology*, vol. 36, no. 6, pp. 1646-1657, 2013.
- [119] L. W. Bartels, H. F. Smits, C. J. Bakker, and M. A. Viergever, "MR imaging of vascular stents: effects of susceptibility, flow, and radiofrequency eddy currents," *Journal of Vascular and Interventional Radiology*, vol. 12, no. 3, pp. 365-371, 2001.
- [120] R. MacCurdy, R. Katzschmann, Y. Kim, and D. Rus, "Printable hydraulics: A method for fabricating robots by 3D co-printing solids and liquids," in *2016 IEEE International Conference on Robotics and Automation (ICRA)*, 2016: IEEE, pp. 3878-3885.
- [121] J. P. Whitney, M. F. Glisson, E. L. Brockmeyer, and J. K. Hodgins, "A low-friction passive fluid transmission and fluid-tendon soft actuator," in *2014 IEEE/RSJ International Conference on Intelligent Robots and Systems*, 2014: IEEE, pp. 2801-2808.
- [122] G. Dämmer, S. Gablenz, A. Hildebrandt, and Z. Major, "Design and shape optimization of PolyJet bellows actuators," in *2018 IEEE International Conference on Soft Robotics (RoboSoft)*, 2018: IEEE, pp. 282-287.
- [123] K. M. Digumarti, A. T. Conn, and J. Rossiter, "Euglenoid-inspired giant shape change for highly deformable soft robots," *IEEE Robotics and Automation Letters*, vol. 2, no. 4, pp. 2302-2307, 2017.
- [124] W. Jung, Y. Kang, S. Han, and Y. Hwang, "Biocompatible micro, soft bellow actuator rapidly manufactured using 3D-printed soluble mold," *Journal of Micromechanics and Microengineering*, vol. 29, no. 12, p. 125005, 2019.
- [125] H. F. Lau, "3D-Printed Inflatable Actuators: Design and Development of Soft Actuators for a Pneumatically-Actuated Soft Robotics Arm," 2019.
- [126] H. M. Anver, R. Mutlu, and G. Alici, "3D printing of a thin-wall soft and monolithic gripper using fused filament fabrication," in *2017 IEEE International Conference on Advanced Intelligent Mechatronics (AIM)*, 2017: IEEE, pp. 442-447.
- [127] R. Mutlu, C. Tawk, G. Alici, and E. Sariyildiz, "A 3D printed monolithic soft gripper with adjustable stiffness," in *IECON 2017-43rd Annual Conference of the IEEE Industrial Electronics Society*, 2017: IEEE, pp. 6235-6240.
- [128] U. Berger, "Direct manufacturing of pneumatic grippers by stereolithography," *Virtual and Rapid Manufacturing: Advanced Research in Virtual and Rapid Prototyping*, p. 463, 2007.

Appendix A. Functional analysis self-propelling needles

This functional analysis defines the underlying principles of the self-propelling, steerable needle developed by Scali [21] and the differences with the needle presented in this study. In the needle developed by Scali [21], the six needle segments were individually actuated by six linear stepper electromagnetic motors for both needle advancing and steering. The needle of this study is manually actuated for needle advancing as well as steering. We developed the actuation unit in such a way that the manual actuation for needle advancing can be replaced by pneumatic actuation in the next generation of the self-propelling needle. A schematic representation of the actuation of the needle developed by Scali [21] and the needle developed in this study is shown in Fig. A-1.

Subfunctions were identified that are required to position the MRI-ready, self-propelling needle. A schematic representation of these functions is shown in Fig. A-2. The subfunctions below the primary function of positioning the needle were determined to be:

- Control the needle positioning;
- Actuate the needle positioning;
- Perform the needle positioning.

The control unit controls both the steering and the needle advancing. In order to control the needle positioning is a subfunction that is outside the scope of this study. Ideally, the needle would be controlled by an operator using a human-machine interface that incorporates both a dosimetry platform and visual feedback of the position of the needle to set the desired needle-path.

Both for steering and needle advancing, an actuator is required. In the needle developed by Scali [21], steering is achieved by creating an offset between adjacent needle segments, a discrete bevel-tip, by individually advancing the needle segments using six electromagnetic motors. In order to advance the needle, the needle segments require actuation of a reciprocal back and forth motion over a specified distance called the “stroke”. All needle segments are constantly in motion: one needle segment moves forward until the stroke value is reached while the remaining five needle segments move $1/5^{\text{th}}$ of the stroke value backwards, similar to the continuous actuation mode described by Scali et al. [32]. The needle segments should be connected to the actuation unit, to transmit the motion of the actuation unit to the needle segments.

The final subfunction is related to performing the needle positioning inside the body. First, the needle segments should be interconnected in a circular configuration with the desired dimensions for insertion into the prostate. To allow for steering of the needle in the right direction, knowledge about the orientation of the endpoint of the needle segments is required. When the operator knows which needle segment at the proximal end of the needle corresponds with which needle segment on the distal end of the needle (i.e., inside the body of the patient), the operator knows what side to steer to perform a steering motion in the desired direction.

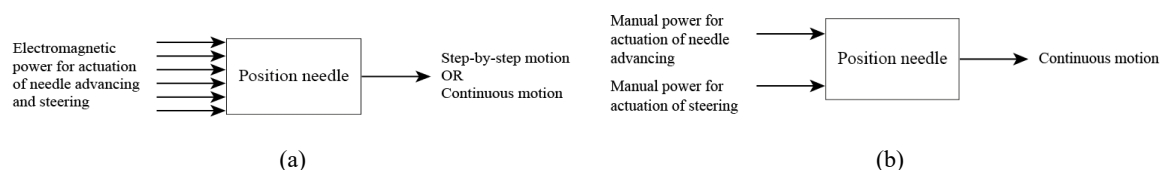


Fig. A-1. Schematic representation showing the primary function of the steerable needle and the energy going in and out of the instrument, comparison with (a) the design by Scali [21] and (b) the design presented in this study.

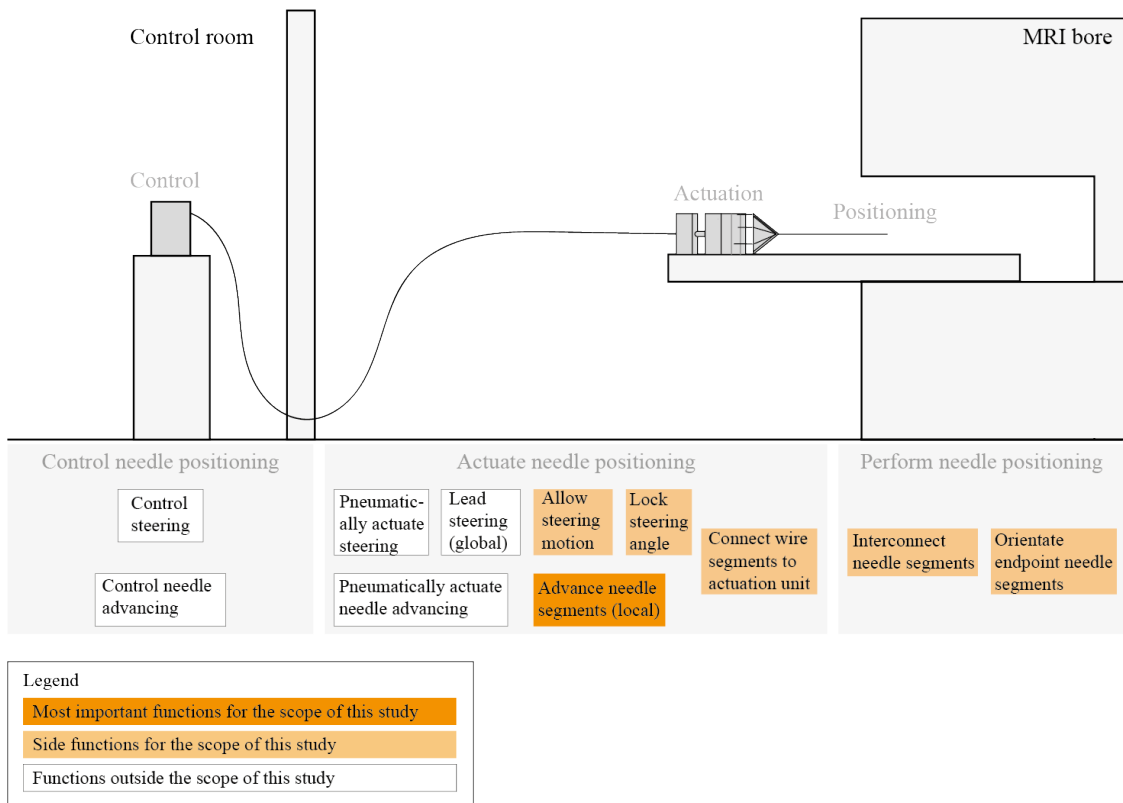


Fig. A-2. Schematic representation of the lower-level functions of the MRI-ready, self-propelling, steerable needle.

Appendix B. State of the art pneumatic actuators

A major challenge in the development of a pneumatic robotic system used in the MRI scanner is the design of an actuator that is MRI-ready and is small enough to fit inside the MRI scanner. Pneumatic actuators found in the scientific and patent literature describe different working mechanisms. In this appendix, we discuss a selection of pneumatic actuators described in the scientific and patent literature.

Most pneumatic actuators found in the scientific and patent literature were driven by pistons [40, 44, 92, 95-101]. Only one pneumatic actuator was found that uses bellows instead of pistons as the actuation mechanism. Comber et al. [102, 103] developed hollow annular-shaped and helix-shaped bellows placed in series for a translating and rotating motion, respectively. The bellows were produced using selective laser sintering (3-D Systems Sinterstation 2500 plus) and expand under positive pressure and contract because of the restoring force of the material stiffness. A classification of the pneumatic actuation mechanisms found in the scientific and patent literature based on the type of motion they actuate can be seen in Table B-I.

Motion conversion mechanisms were applied to convert the motion of the pneumatic actuator to the required motion of the instrument. Five pneumatic actuators were found that use gear-type mechanisms to convert the translating motion of pneumatic pistons to a rotation [40, 44, 95-97]. The PneuStep developed by Stoianovici et al. [95, 100] uses three diaphragm cylinders connected to an internal spur gear. The pneumatic rotation stepper motor developed by Sajima et al. [44] uses three pneumatic cylinders connected to an axial gear. Groenhuis et al. [40, 101] developed a rotational stepper motor using four cylinders, produced using laser cutting and fused deposition modelling (FDM) with the Ultimaker 2, which interact with a spur gear. Chen et al. [96] developed an actuator that uses a click-pen mechanism to convert the translating motion of a piston into a rotation. The click-pen mechanism consists of a lower pushrod that interacts with both the upper pushrod and the outer guide pipe and causes rotation of the upper pushrod and output shaft. The upper pushrod is pressed down by a spring. Guo et al. [97] adapted this mechanism to a bidirectional actuator using two pistons, two direction gears, and an input and output gear, produced using Polyjet printing (Objet 260, Stratasys).

Two pneumatic actuators were found that convert a translating motion of pistons to a rotating motion using a crankshaft. Secoli et al. [92] produced an acrylonitrile butadiene styrene (ABS) crankshaft using FDM (MakerBot Replicator, Makerbot Inc.); furthermore, three plastic pistons are used. Boland et al. [98] produced an actuator using stereolithography (SLA) (Form 2, Formlabs) consisting of four cylinders and a crankshaft.

Bomers et al. [99] developed an actuator that converts the translating motion of five pneumatic cylinders with cone tips to either a screw-motion or translation by the interaction with a two-dimensional pattern of holes on a rod. The combination of cylinders that are actuated causes either a rotation or a translation. Groenhuis et al. [40, 101] also developed an actuator that converts the translating motion of pistons to a translating stepper motion using four pistons and a rack. The classification of these motion conversion mechanisms can be seen in Table B-II.

Table B-I. Classification pneumatic actuation mechanisms.

Motion actuation	1. Translation		2. Rotation
Mechanism found in literature	1.1 Piston [40, 44, 92, 95-101]	1.2 Bellows [102, 103]	2.1 Helicoid bellows [102, 103]

The wedge-type gears (Table B-II) are space-efficient as they allow for a cylindrical shape and a hollow axial centre of the device, providing space for functionalisation of the needle, therefore the wedge-type gears were used as a starting point for the conceptual design of the needle actuation unit.

Table B-II. Classification motion conversion mechanisms in pneumatic actuators using pistons.

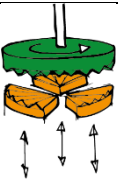


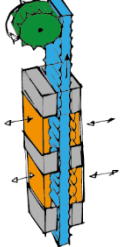

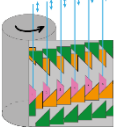
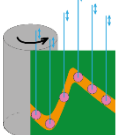


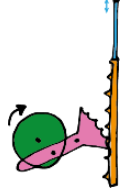


Motion conversion	1. Translation to translation		2. Translation to rotation		3. Translation to screw motion
Mechanism found in scientific literature	1.1 Holes in rod [98]	1.2 Rack [40,101]	2.1 Wedge gears	2.2 Crankshaft [92,98]	3.1 Holes in rod [98]
		2.1.1 Axial gear [44]	2.1.2 Spur gear [40,95,100,101]	2.1.3 Click-pen [96,97]	

Appendix C. Idea generation

This appendix comprises the design options for the functions explained in Appendix A.



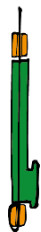

C.1 Needle segment motion actuation

Different combinations of motion conversion mechanisms can be used to convert a discrete translating motion to the sequential translation of the needle segments.

Solutions →	1	2	3	4	5
Subfunctions ↓					
Locally advance needles					
1.a) Convert reciprocating motion into global rotating motion	Axial gear 	Spur gear Circumferential teeth  Mutilated pinion 		Translational stepper and rack and pinion 	Click pen 
1.b) Locally advance needles in translating motion	Teeth height 	Cam 			
2) 6x locally advance translating motion	Rack and pinion 	Slider crank 	Quick return 	Lead screw slider 	Reciprocating rack and pinion 

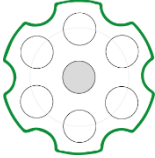
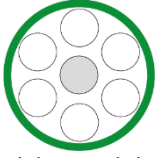
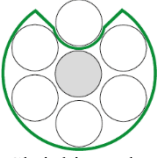
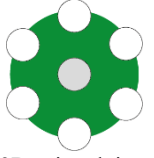
C.2 Connect needle segments to actuation unit

The needle segments can be connected to the actuation unit using an external mechanism such as a set screw [32, 104] or beads, but these mechanisms require additional space. An internal connection using glue was considered to be the most space-efficient, and it eased manufacturing.

Solutions →	1	2	3	4
Subfunctions ↓				
Connect needle segments to needle segment holders	Clamping point by set screw [32, 104]	Self-clamping system [60]	Clamp bottom and top with bead	Glue rod in hole [105, 106]
				

C.3 Interconnect needle segments

The six needle segments had to be bundled in a circle at the needle-tip. The interconnection has to allow a translating motion of the needle segments in the z-direction relative to each other. The interconnection should have a minimum wall thickness, to minimise the normal force acting on the interconnection that increases its cutting force when protruding through the tissue. An interlocking flower-shaped ring or a stainless steel ring as incorporated in previous prototypes developed by Scali [29] is not MR safe. An SLA printed polylactic acid (PLA) ring is MR safe but has a high surface area compared to a shrinking tube applied in a previous prototype developed by Scali et al. [32]. A polyethylene terephthalate (PET) shrinking tube (Vention Medical) is inherently MR safe and has a wall thickness of 0.013 mm. The resulting insertion diameter of the needle including the shrinking tube is 0.839 mm.



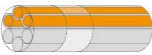


Solutions →	1	2	3	4
Subfunctions ↓				
Interconnect needle segments				
	Aluminium interlocking flower-shaped ring: OD 1.2 mm, radius arrangement needle segments 0.38 mm [29]	Stainless steel ring: OD 1.0 mm, ID 0.9 mm [107]	Shrinking tube (Vention Medical) fixated with Pattex instant glue, Gold Gel: ID 0.813 mm, OD 0.839 mm, T 0.013 mm [32]	3D printed, i.e., stereolithography (Formlabs Form 3B), ring with holes: OD 1.15 mm

OD = outer diameter
ID = inner diameter
T = wall thickness

C.4 Provide orientation endpoint needle

The needle consists of six flexible Nitinol rods with a length of 200 mm. The needle segments at the distal tip might rotate relative to their position at the proximal end of the device. To allow for accurate steering control, the operator needs to know the needle position and orientation of the needle segments at the distal end relative to the needle segments at the proximal end to set the correct steering direction. MRI-guided focal therapy relies on the MR images to determine the position of the needle. MRI-guided instrument tracking can be achieved by a variety of passive, active, and hybrid methods. The simplest method of determining the position of the needle is to acquire an image of the needle, which was employed in this study. The signal void produced by the presence of the needle shows up in MR images and can be tracked [108]. A calibration procedure similar to the trial and error process consisting of

minute retractions and reinsertions utilised by the wasp ovipositor [22] can be visualised using MRI. The calibration procedure should involve some steering actuation to allow for determination of the orientation of the needle segments at the distal tip relative to the needle segments at the handle, assuming the needle segments do not switch place relative to each other.

Solutions → Subfunctions ↓	1	2	3	4	5
Provide orientation endpoint needle segments	Static		Dynamic		
	3/6 needle segments coloured with paramagnetic coating	½ shrinking tube coloured with paramagnetic coating	Fill 3/6 needle segments with paramagnetic filler gel	Fibre Bragg Grating	Calibration procedure
					

C.5 Allow steering

To allow for a global steering unit, a system that allows a yaw and pitch motion, but prevents a roll motion is required. In Hopkins and Culpepper’s freedom and constraint topology, this complies to a disk of rotations as the freedom space [109, 110] (Fig. C-1). The disk of rotations was used as a starting point for the design of the structure to allow steering. The use of compliant and rigid connections was considered. The additive manufacturability of a compliant system that allows a pitch and roll motion leads to more complex manufacturing; therefore, a spin-like system with bulges and notches to prevent the yaw motion was chosen.

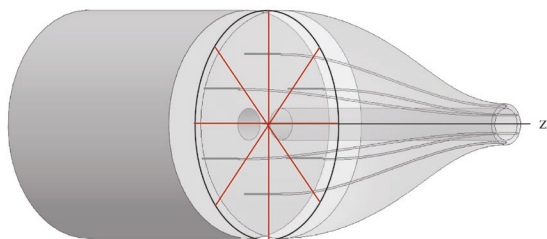
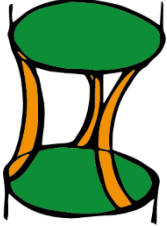
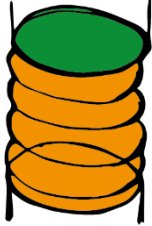
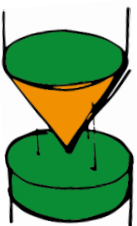
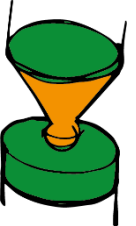
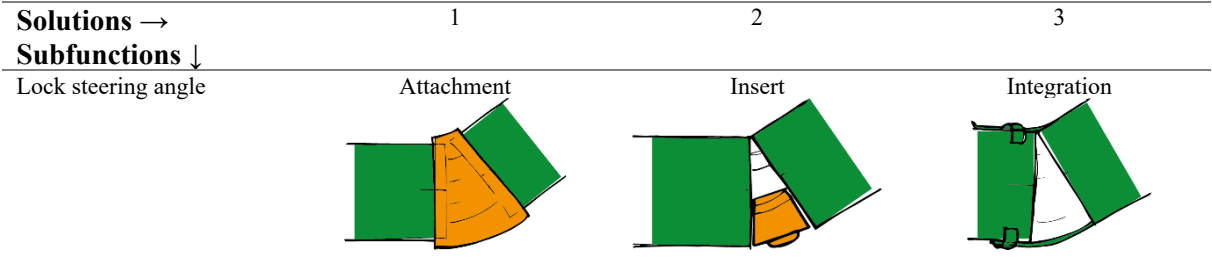


Fig. C-1. Visualisation of the freedom space to allow a yaw and pitch motion of the housing with respect to the cone for steering. The freedom space is a disk of rotations (red).

Solutions → Subfunctions ↓	1	2	3	4
Allow global steering	Compliant		Rigid	
	Flexures	Tubing	Spin	Ball bearing
				

C.6 Lock steering angle

For locking the steering angle, an external, internal, and a system integrated with the actuation unit were considered. The internal and integrated systems would minimise the space required but would risk interference with the needle segments; therefore, an external system was chosen.



Appendix D. Concepts rotational selector

In the main text one concept for a rotational selector is presented. This appendix presents two other concepts for the rotational selector.

D.1 Axial gear concept

The first concept contains three gear parts that interact with an axial gear through a wedge mechanism (Figs D-1 and D-2). Three actuators actuate the three gears for a translating motion. During actuation one of the gears is actuated in the positive z-direction, while the other gears are actuated in the negative z-direction (Fig. D-2a). Sequentially actuating the three gears with in the positive z-direction results in a rotation of the axial gear around the z-axis (Fig. D-2b). One sequence of actuating the three gears with positive pressure results in a 12° -rotation of the axial gear because the axial gear has 30 teeth (Fig. D-2c). The axial gear contains a cam. The needle segments are attached to needle segment holders that interact with the cam. The cam converts the rotating motion of the axial gear into the translating sequence of the needle segment holders in the z-direction. A rotation of 360° of the cam equals one cycle where all needle segments are moved over the stroke distance in the positive z-direction during 60° of the cam rotation and are moved over the stroke distance in the negative z-direction during the remaining 300° of the cam rotation.

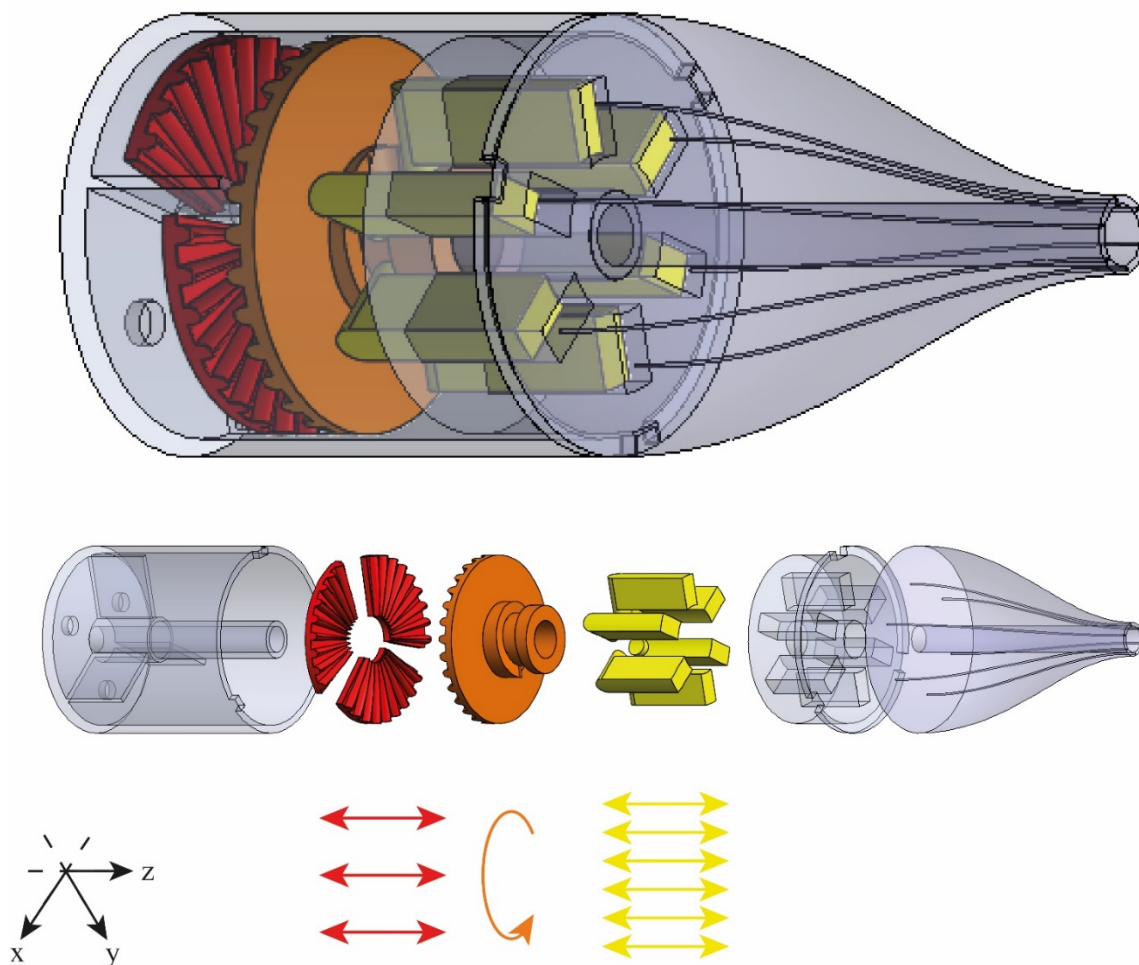


Fig. D-1. The arrows show the motion space for the component in the same colour. (a) Sketch showing the axial gear concept with the translating motion of three lower gears (in red) in z-direction that actuates rotation of the upper gear and cam (in orange) around the z-axis, this actuates the sequential translation of the needle holders (in yellow) in the z-direction

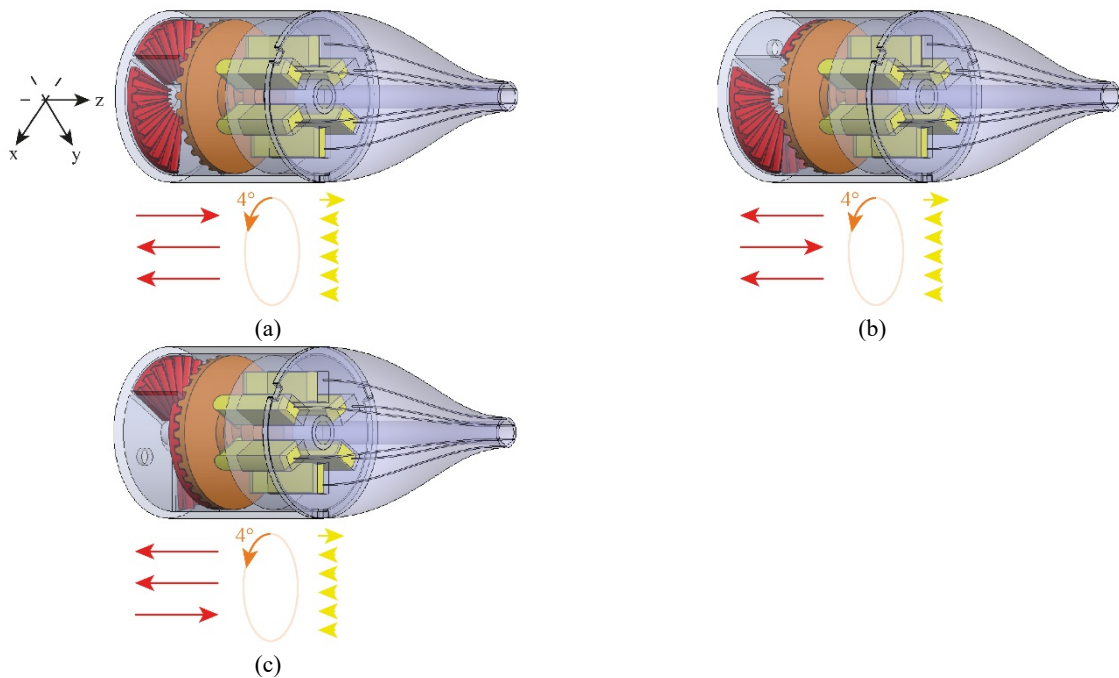


Fig. D-2. Motion sequence for one step of the cycle of concept 1. The visualisation of the concept shows the initial position of the components of the concept in that specific part of the motion sequence. The arrows show the upcoming motion for the component in that colour. (a) One gear (in red) is moved in the positive z-direction. The teeth of the actuated gear push against the teeth of the axial gear. As a result, the axial gear (in orange) rotates 4° around the z-axis. The needle segment holders interact with the cam on the axial gear and translate in the z-direction. One needle segment holder moves in the positive z-direction and the remaining five needle segment holders move in the negative z-direction. (b) The subsequent gear is moved in the positive z-direction. Resulting again in rotation of the axial gear and translations of the needle segments. (c) The third gear is moved in the positive z-direction. Resulting again in rotation of the axial gear and translations of the needle segments. The gears are subsequently actuated by positive air pressure to interact with the axial gear.

D.2 Spur gear concept

The second concept contains four toothed pistons (Figs D-3 and D-4). The toothed piston acts as a bellows because of the flexible sidewalls. Each piston is connected to the opposite piston, hence expansion of the air chamber of the first piston results in contraction of the third air chamber and the other way around, likewise for the second and fourth air chambers. Actuation of the first air chamber results in expansion of that air chamber (Fig. D-4a). The expansion results in contact between that piston and the spur gear. First, the piston of the first chamber interacts with the spur gear, followed by the piston of the second chamber (Fig. D-4b), and so on, causing the rotation of the spur gear around its z-axis. One sequence of actuating the four pistons results in a 72° -rotation of the spur gear because the spur gear has five teeth. The spur gear contains a cam. The needle segment holders interact with the cam, so the required motion sequence of the needle segments is obtained. The four flexible-walled air chambers require four actuators for a translating motion.

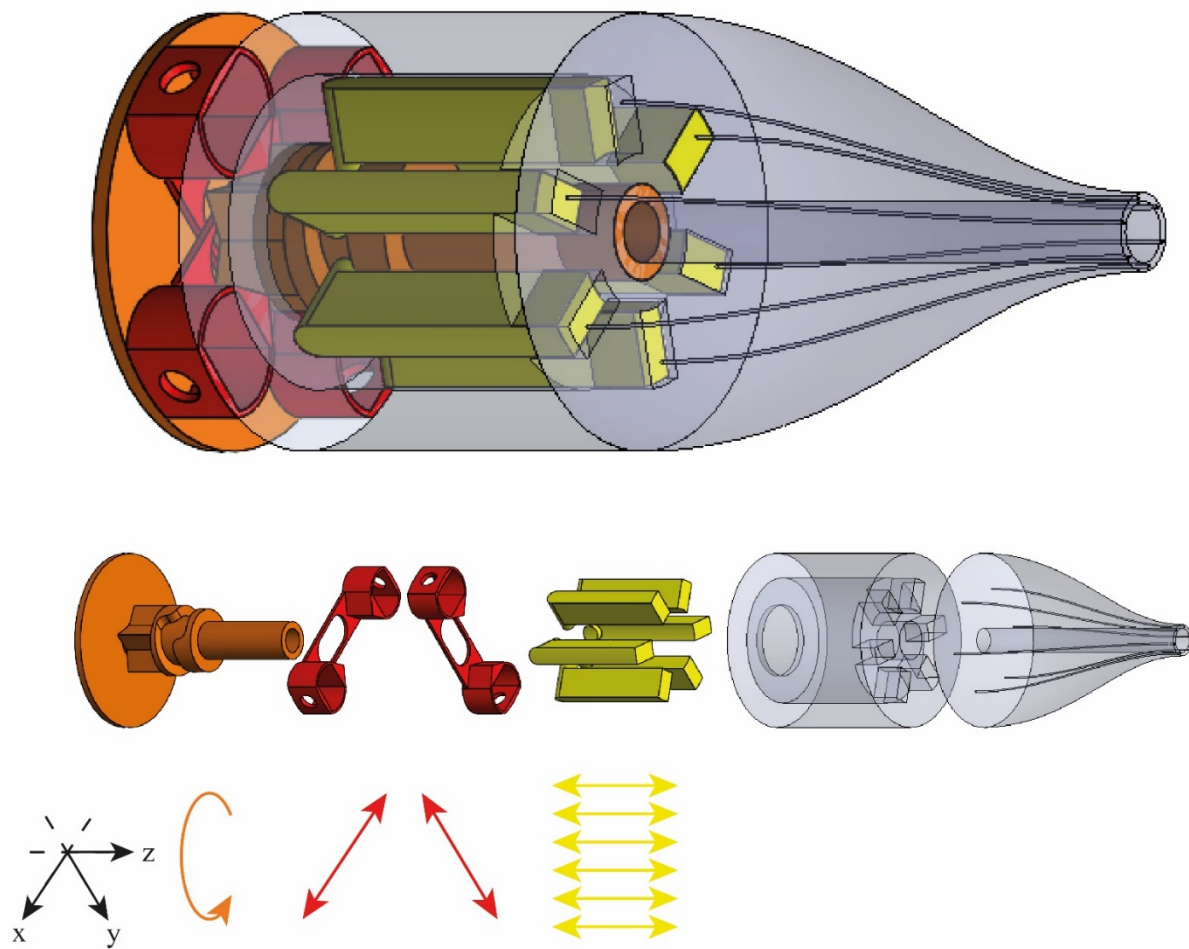


Fig. D-3. Sketch showing the spur gear concept with the translating motion of two piston-couples (in red) in x- and y-direction that actuate the rotation of the gear and cam (in orange) around the z-axis, this actuates the sequential translation of the needle holders (in yellow) in the z-direction.

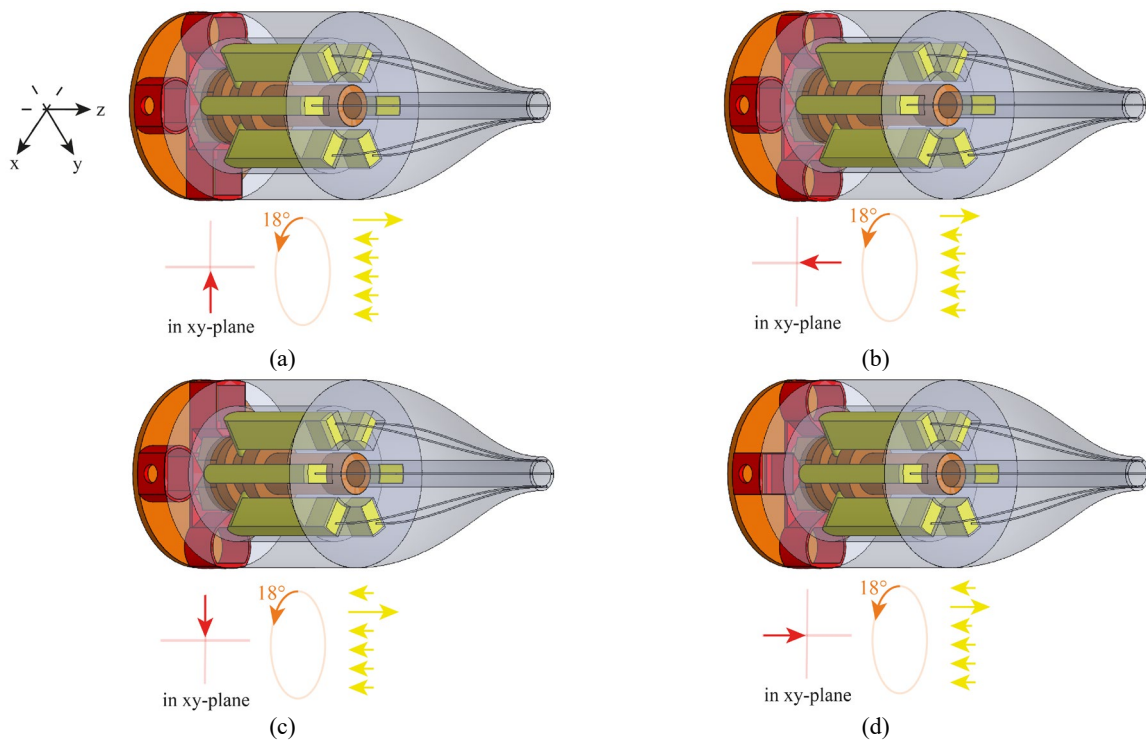


Fig. D-4. Motion sequence for one step of the cycle of concept 2. The visualisation of the concept shows the initial position of the components of the concept in that specific part of the motion sequence. The arrows show the upcoming motion for the component in that colour. (a) The first air chamber is actuated (in red), this expands the air chamber resulting in the piston contacting the spur gear (in orange). This contact causes the spur gear with the cam to rotate around the z-axis. The needle segment holders (in yellow) interact with the cam on the axial gear and translate in the z-direction. One needle segment holder moves in the positive z-direction and the remaining five needle segment holders move in the negative z-direction. (b) The subsequent air chamber is actuated and thus expanded which proceeds the rotation of the axial gear and the translation of the needle segment holders. (c) The third air chamber is actuated, resulting in proceeding movements of the spur gear and the needle segment holders. (d) Lastly, the fourth air chamber is actuated, again resulting in proceeding movements of the spur gear and the needle segment holder. The sequence starts again by actuating the first air chamber.

Appendix E. Design iterations concept prototyping

To test whether the translating actuation in the z-direction results in a translating sequence of the needle segment holders in the z-direction the actuation unit was prototyped using the fused deposition modelling (FDM) technology with the Ultimaker 2 and the Prusa and using the stereolithography (SLA) technology with the Formlabs Form 3B printer.

E.1 Prototype 1

The components of the first prototype (height (H) 155.5 mm, outer diameter (OD) 100 mm) were 3D printed using FDM (Ultimaker 2) in PLA (Figs E-1,2). The goal of the prototype was to test whether the translating motion of the selector results in rotation of both the selector itself and the ratchet and if these rotations eventually lead to a translating sequence of the needle segment holders.

The first prototype showed that the up-down manual translating actuation of the selector leads to rotation of the selector and the ratchet and eventually a translating sequence of the needle segment holders. However, the holders make an additional vertical motion to overcome the height of the teeth of the ratchet. Furthermore, a form fit shape of the ratchet in the selector would help to transmit the rotating motion of the selector to the ratchet.



Fig. E-1. Photograph of the first prototype of the actuation unit.

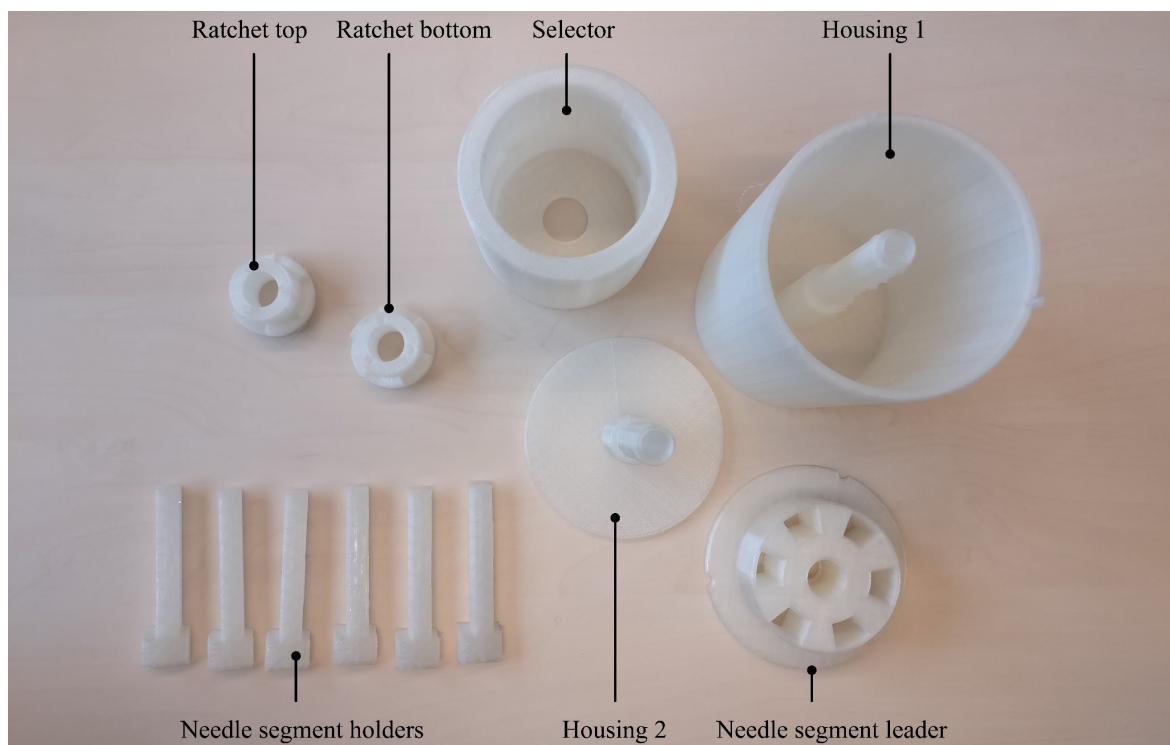


Fig. E-2. Photograph of the components that make up the first prototype of the actuation unit.

E.2 Prototype 2

The components of the second prototype (H 60 mm, OD 50 mm) were 3D printed using FDM (Ultimaker 2) in PLA (Figs E-3,4). This prototype differs from the first prototype as the teeth of the selector that cause the rotation are not the same teeth as the teeth that interact with the needle segment holders. The change of the mechanism has as a result that the needle segment holders do not have to overcome the barrier of each tooth, but can slide along a smooth path, more like a cam. An additional advantage is the possibility to adjust the steepness of the slope of the teeth that cause the rotation, to allow interaction with less friction, than when the teeth interacted directly with the needle segment holders. The goal of the second prototype was to test whether the outcome motion of the needle holders was the desired motion in a circular sequence without the additional upwards motion.

The second prototype showed the correct outcome motion; the additional motion upwards every step was removed. However, the motion did not go smoothly; the angles of the teeth should be increased. Otherwise, the mechanism works like a wedge mechanism and generates too much friction. Furthermore, the needle segment holder that interacts with the cam should be round and with a precise fit, to allow for a smooth sliding motion of the needle segment holders in the cam slot.



Fig. E-3. Photograph of the second prototype of the actuation unit.

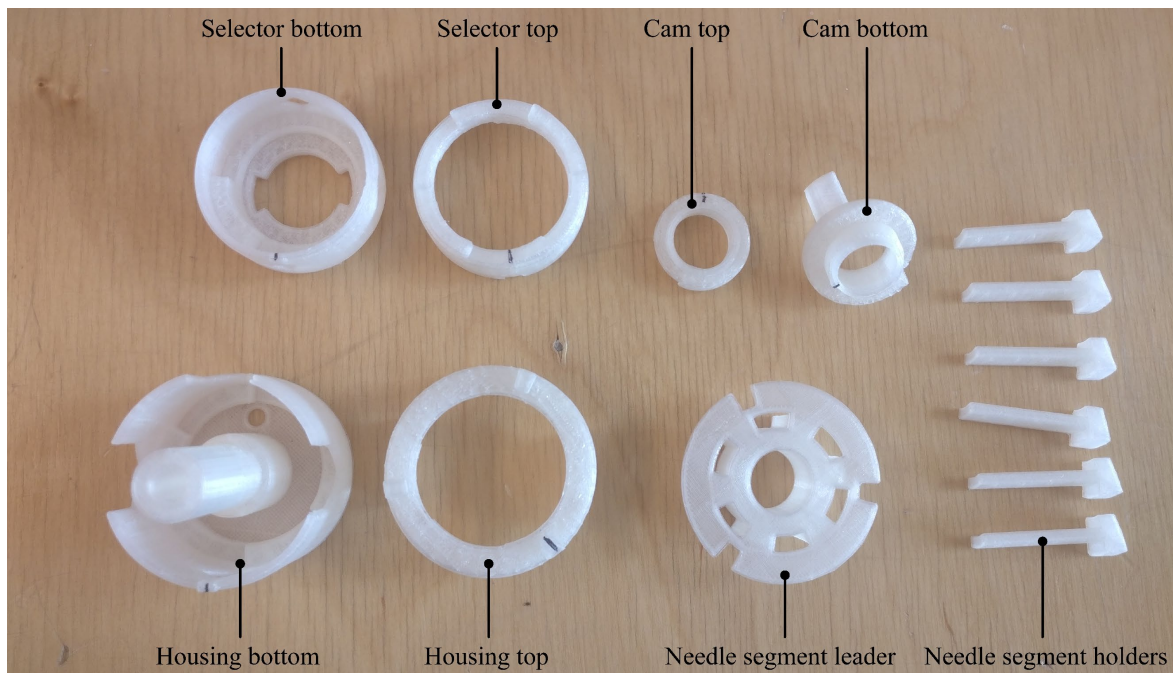


Fig. E-4. Photograph of the components that make up the second prototype of the actuation unit.

E.3 Prototype 3

The components of the third prototype (H 83.5 mm, OD 34.8 mm) were 3D printed using FDM (Prusa) in polyethylene terephthalate glycol-modified (PETG) (Figs E-5,6). The angles of the teeth of the selector and the housing were changed to 45°, to allow for smoother compared to the second prototype. To minimise the outer dimensions, the tolerances of this prototype are tighter than the tolerances of the second prototype. The clearance for moving parts was set to 0.2 mm, for example, a 9.8-mm diameter pin in a 10-mm hole. The clearance for form-fit parts was set to 0.1 mm, for example, a 9.9-mm pin in a 10-mm hole.

The third prototype showed that the clearance set for the moving parts was too tight, the clearance should be doubled to 0.4 mm, for example, a 9.6-mm diameter pin in a 10-mm hole. Furthermore, the slot of the cam should be shaped in such a way that the needle segment holders cannot leave the slot radially. Lastly, to prevent jamming, the needle segment holders should remain covered by the selector.



Fig. E-5. Photograph of the third prototype of the actuation unit.

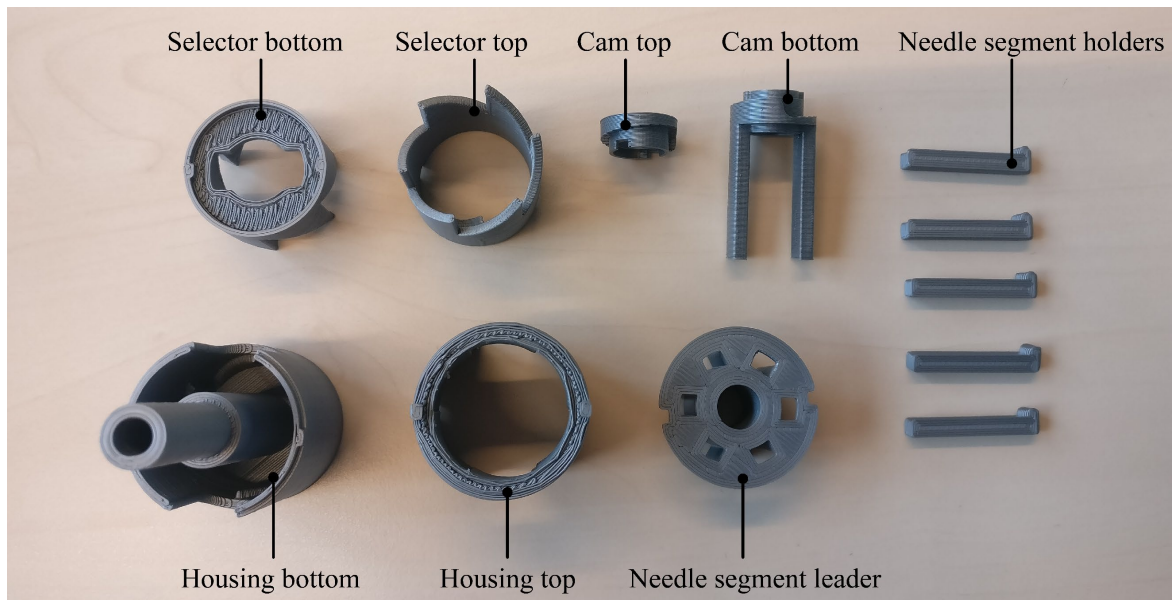


Fig. E-6. Photograph of the components that make up the third prototype of the actuation unit.

E.4 Prototype 4

The components of the fourth prototype (H 93.5 mm, OD 35 mm) were 3D printed using FDM (Prusa) in PETG (Figs E-7,8). To smoothen the motion within the actuation mechanism, some design guidelines were taken into account: (1) rotating parts require two peripheral rims with maximum interstitial space, (2) translating parts require a sliding bar, and (3) rotating and translating parts require three half-sphere protrusions. These guidelines minimise the friction by minimising the interaction surface. The cam was 3D printed twice. The first cam moved the needle segment holders over the complete required stroke length during one translation, i.e., the forward motion. The second cam moved the needle segment holders over the required stroke length during the combination of the forward and backward translation.

The first cam for the fourth prototype showed that the needle segment holders got jammed in their upward stroke, the second cam allowed for a smooth motion.



Fig. E-7. Photograph of the fourth prototype of the actuation unit.

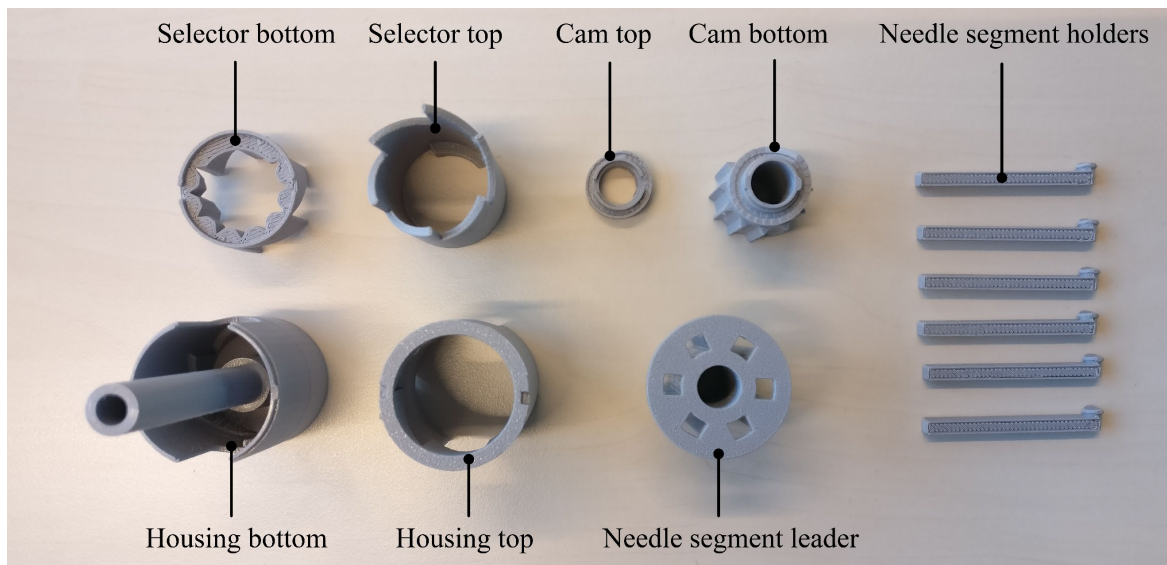


Fig. E-8. Photograph of the components that make up the fourth prototype of the actuation unit.

E.5 Prototype 5

The components of the fifth prototype (H 93.5 mm, OD 35 mm) were 3D printed using SLA (Formlabs Form 3B) in Durable Resin (Figs E-9,10). The properties of Durable resin are comparable to polypropylene [111]. The goal of the fifth prototype was to test whether the 3D printed parts using SLA allow for interaction with less friction as compared to the 3D printed parts using FDM of the fourth prototype. The SLA process using the Formlabs Form 3B printer allows for a lower layer height compared to the FDM processes using the Ultimaker 2 or the Prusa. Furthermore, the selector was printed as one part, because the support generation process in the SLA process allows for smooth teeth on both sides of the selector in one part.

The components of the fifth prototype were a bit wrapped because of the SLA process. The parts designed to be cylindrical were not printed cylindrical, causing the selector to get jammed inside the housing. Printing the cylindrical parts in their vertical position might prevent this problem, instead of printing the cylindrical parts angulated relative to the base plate as suggested by the Formlabs software. However, the surface of the SLA printed parts was smoother than the FDM printed parts. The layers were less visible and perceptible when touching the components of the fifth prototype.



Fig. E-9. Photograph of the fifth prototype of the actuation unit.

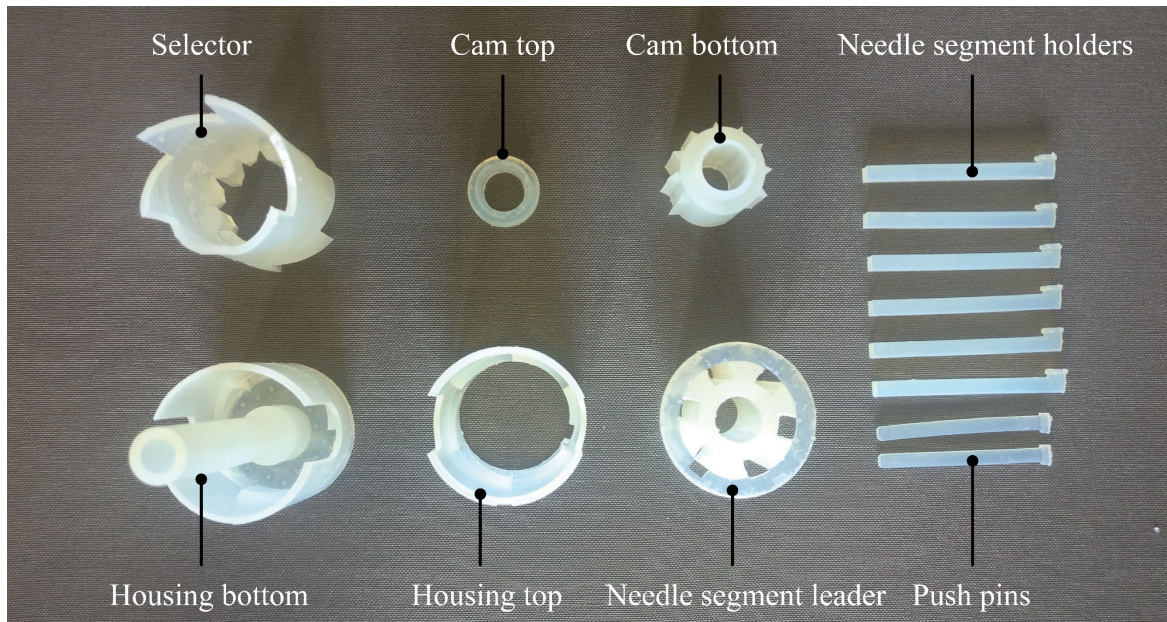


Fig. E-10. Photograph of the components that make up the fifth prototype of the actuation unit.

E.6 Conclusions concept prototyping

Fig. E-11 shows the five prototypes used for the iterative design process of the actuation unit. In the first prototype, the teeth of the selector caused both the rotation of the ratchet and the translating motion of the needle segment holders, which imposes an additional upwards motion on the needle segment holders to overcome the barrier of the teeth in each step. In the second prototype, the additional upwards motion was removed by adding a path to create a cam out of the ratchet that causes the translating motion of the needle holders. The teeth of the selector now solely cause the rotation of the cam. In prototype 3, the angles of the teeth were changed to 45° to lower the friction of the teeth of the selector with the teeth of the housing. Furthermore, in the iterative design process of prototype 3, 4, and 5 the clearance for the moving parts relative to each other was set to 0.4 mm, which showed to be optimal for parts produced using SLA through a trial-and-error process to allow for a smooth motion. Furthermore, the shape of the cam-track was changed, so it enclosed the head of the needle segment holders (i.e., the cam-followers) and constrained their motion in the z-direction during the entire cycle.



Fig. E-11. Photograph of the five iterations of the actuation unit using additive manufacturing. Prototype 1 and prototype 2 were FDM printed in PLA using the Ultimaker 2. Prototype 3, and prototype 4 are FDM printed in polyethylene terephthalate glycol (PETG) using the Prusa. Prototype 5 is SLA printed in Durable Resin using the Formlabs 3B.

Appendix F. Functioning internal mechanism

F.1 Selector torque

The teeth of the selector act on the teeth of the housing through a wedge mechanism. The manual translation of the manual translation ring and thus the selector in the positive z -direction results in contact between the selector's teeth at the right side and the housing top. The contact creates a force in the z -direction and the x - y plane because of the inclined surfaces of the teeth of the selector and the housing top. The force component in the x - y plane causes the output torque that rotates the selector around its z -axis. The force component in the z -direction equals the driving force caused by the manual actuation (Fig. F-1).

The manual translation of the manual translation ring in the negative z -direction causes the selector to translate in the negative z -direction. As a result of the translation, the selector gets in contact with the left teeth of the housing, resulting in forces that cause a torque again in the same direction. The selector contains six teeth on the left side and six teeth on the right side. Each tooth comprises 60° of the circular cross-section of the selector. Upon a selector movement of $\Delta z = 25$ mm, the selector rotates by the step size $\gamma = 30^\circ$. The theoretical output torque, \mathbf{T} , as a function of the manual actuation force, \mathbf{F}_{man} , ignoring friction losses, can be found using the work balance [40] (Eq. F-eq1).

$$\mathbf{T}\gamma = \mathbf{F}_{man}\Delta z \quad (\text{F-eq1})$$

The force component in the x - y plane that causes rotation of the selector is determined by dividing the theoretical output torque by the radius of the selector (equation F-eq2).

$$\mathbf{F}_{xy} = \frac{\mathbf{T}}{r} \quad (\text{F-eq2})$$

where r is the radius of the selector, which is 14.3 mm for the centreline of the cross-section of the selector.

F.2 Selector friction

To motion of the teeth of the selector relative to the surface of the teeth of the housing causes a friction force. Every time the selector touches the upper or lower teeth of the housing and the sliding starts, stiction and Coulomb friction come into play. Stiction is the higher friction force threshold in a static situation compared to a dynamic situation because the two surfaces stick to each other [112], this results in a discontinuity in the Coulomb friction model at zero relative velocity [113]. The Coulomb model [113] is the most basic friction model, where the friction force is given by equation F-eq3.

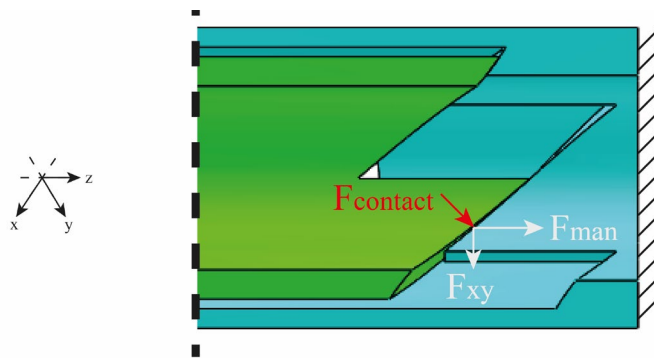


Fig. F-1. The contact force between the selector tooth and housing tooth, $\mathbf{F}_{contact}$, causes a force in the z -direction, \mathbf{F}_{man} , and a force in the x - y plane, \mathbf{F}_{xy} .

$$\mathbf{F}_f = \mu \mathbf{F}_n \quad (\text{F-eq3})$$

where μ is the friction coefficient, and \mathbf{F}_n is the normal force. The relative motion of the selector to the housing is not taken into account in the standard Coulomb friction model. The friction coefficient depends on the materials nature and surface roughness [114]. The normal force can be computed from the manual actuation force using trigonometry (Eq. F-eq4, Fig. F-2).

$$\mathbf{F}_n = \cos(\delta) \mathbf{F}_{man} \quad (\text{F-eq4})$$

In practice, the friction coefficient of the selector teeth surface is likely to be higher than a clean and dry plastic surface. Because the selector was 3D printed in the z-direction using stereolithography (SLA), a staircase effect appeared on the teeth's sliding surface, increasing the surface roughness, which increases the friction between the selector and the housing. The teeth height is a trade-off between a low friction force and a low selector stroke. A greater teeth height gives a larger angle δ (for $0 < \delta < \frac{1}{2}\pi$), which results in a lower normal force, \mathbf{F}_n , hence a lower friction force \mathbf{F}_f . A larger angle δ , and a decreased layer height, also result in lower surface roughness due to the staircase effect introduced by the SLA printing process [115]. Fig. F-3 shows why the surface roughness, and therefore the resulting friction force, changes with angle δ and the layer height l . However, a greater teeth height also results in a larger selector stroke, as the selector needs to overcome the height of the teeth during translation in the z-direction to allow rotation around the z-axis. The teeth height was chosen to be 16.5 mm, resulting in teeth angle δ of 45° .

F.3 Manual actuation speed

The prototype was designed for manual actuation, unlike the self-propelling needle developed by Scali [21] that was developed to be actuated by six electromagnetic motors. With the manual actuation, the insertion speed could not be controlled exactly. Hence, we assumed that the needle motion does not depend on the insertion speed of the needle. In other words, the non-constant, low speed of the manually actuated needle does not affect the motion of the needle. Higher insertion speeds cause less tissue deformation during cutting or penetrating of a substrate due to viscoelastic properties of the substrate [116]. The motion of the needle does not depend on the speed when there is no viscoelastic behaviour, when the tissue is in a relaxation state, so when the speed of the needle is low enough. Scali [21] actuated the needle with an insertion speed of 2 mm/s, which corresponds to a stroke speed of 12 mm/s, for six needle segments in continuous motion. The manually actuated needle has a designed stroke of 4 mm, one cycle requires 12 translations with the manual translation ring to protrude all needle segments, where

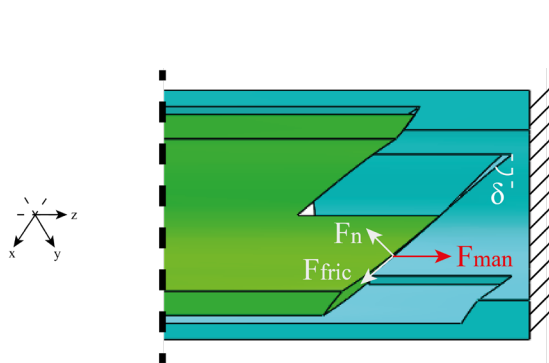


Fig. F-2. The manual force, \mathbf{F}_{man} , in the positive z-direction when the selector is moved in the positive z-direction and is in contact with the housing. This results in a normal force, perpendicular to the teeth surface and a friction force parallel to the teeth surface.

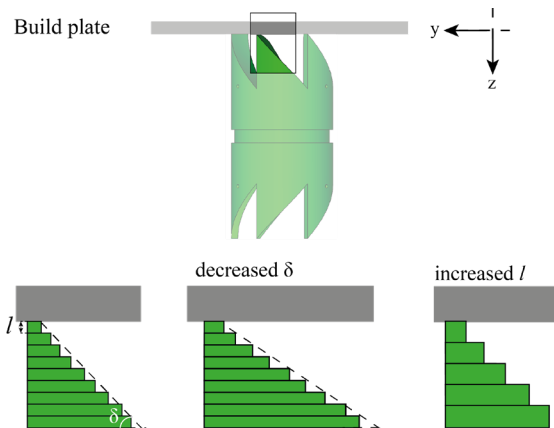


Fig. F-3. Effect of decreased angle δ and increased layer height l on the staircase effect caused by the SLA printing process.

moving the manual translation ring forward and backward was counted as two translations. The frequency of the manual actuation is in the range of 1-6 Hz, which corresponds to an insertion speed of 0.33-2.0 mm/s and a stroke speed of 2.0-12.0 mm/s. These manual actuation speeds are in the same range as the actuation speeds applied by Scali et al. [21, 32]; therefore we assumed that the speed does not affect the motion of the needle.

F.4 Cam profile

The cam converts the rotating motion of the selector into the required translating motion of the needle segments. The heads of the needle segment holders act as cam-followers. The cam was designed as closed-track cam (i.e., form-closed), which has as an advantage that there is a positive drive throughout both the rise and return cycle, unlike an open-track cam combined with a spring [117]. If the cam had an open-track, undercutting would have occurred, as the radius of curvature of the follower path, $\rho = 2.5$ mm, is smaller than the radius of the follower, $r_f = 2.7$ mm. The closed-track cam prevents undercutting, as the concave portion of the cam profile, the working surface, is part of the cam top at the transition from the rise interval to the return interval. Whereas at the transition from the return interval to the rise interval, the working surface is part of the cam bottom (Fig. F-4). Undercutting would have happened at the transition from the rise to the return interval if the working surface would be the cam bottom during the entire cycle.

To analyse the action of the cam, we looked at the time-displacement and associated velocity and acceleration curves. The velocity and acceleration curves were based on respectively the first and second time-derivatives of the time-displacement curve. The velocity curve (Fig. F-5) shows a constant velocity for the needle segment holders during the return interval. The return interval comprises $1 \frac{2}{3} \pi$ of the cycle. For the transition to the rise interval, and vice versa, accelerations are required. Fig. F-5 shows that there is no constant velocity during the rise interval; however, the acceleration is kept finite by the design of a circular tangent arc in the displacement curve. The design was based upon the parabolic motion curve, which reduced the acceleration from infinity to a finite constant value to avoid impact loads [117]. The displacement, velocity, and acceleration curves were produced using MATLAB (version 2019a) (Appendix G)

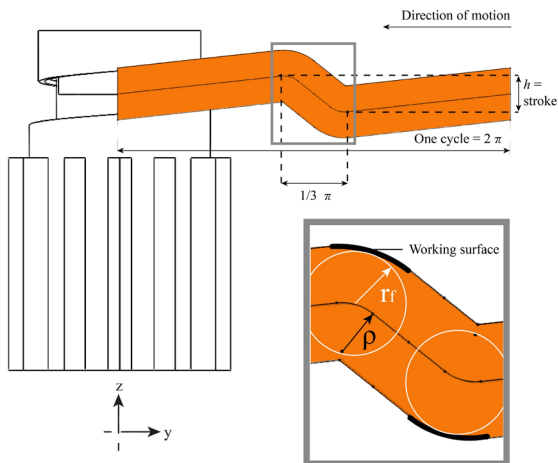


Fig. F-4. Cam path design, h is the stroke of the needle segment holders, ρ is the curvature of the follower path, and r_f is the radius of the follower. The direction of motion of the needle segment holders with respect to the cam is indicated with an arrow.

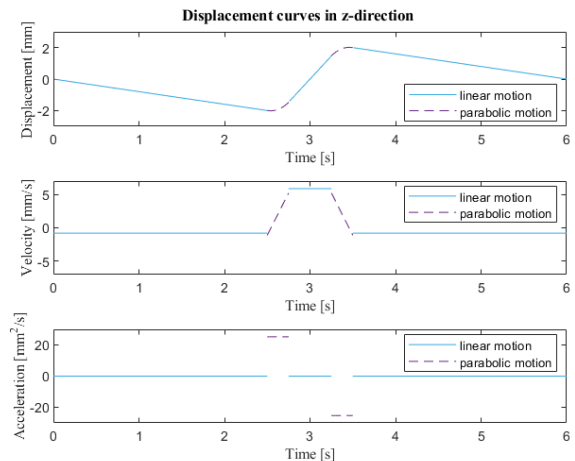


Fig. F-5. Cam displacement, velocity, and acceleration curves for the needle segment holders in the z-direction. The parabolic motion (purple dashed) avoids impact at the beginning and end of the stroke. The remaining parts of the stroke consist of linear motions (blue solid).

Appendix G. MATLAB code cam analysis

This appendix contains the MATLAB code for the analysis of the displacement, velocity, and acceleration curves of the cam. The code requires the data describing the position coordinates of the cam track retrieved from Solidworks (Position_coordinates510.xlsx).

```
%% Cam displacement
% MATLAB code for plotting the displacement curves for the needle pins in the
groove of the cam.
% Author:      Jette Bloemberg
% Last update: 21/10/2020
%%

% Initialization
clf, hold off, clear all, clc
format long

% import the dataset for the x-, y- and t- coordinates, for respectively
% the position in the x-direction, y-direction and the time, retrieved from
% the solidworks model of the barrel cam path.
dataset = xlsread('Position_coordinates510.xlsx','sheet1','A1:J512');
x = dataset(:,10);
y = dataset(:,2);
t = dataset(:,9);

% Position displacement diagram
figure(1)
% linear return motion 2 mm - 0 mm
x1 = x(1:38);
y1 = y(1:38);
t1 = t(1:38);
p1 = polyfit(x1,y1,1);
X1 = x1(1):-0.01:x1(38);
Y1 = polyval(p1,X1);
plot(X1,Y1,'color','#F6780A')
s1 = sprintf('y1 = (%.1f) x + (%.1f)',p1(1),p1(2));
title('Position cam needle segment holders','FontName','Times')
xlabel('Displacement x [mm]','FontName','Times')
ylabel('Displacement z [mm]','FontName','Times')
hold on

% parabolic motion 2 mm
x2 = x(38:188);
y2 = y(38:188);
t2 = t(38:188);
p2 = polyfit(x2,y2,2);
X2 = x2(1):-0.01:x2(151);
Y2 = polyval(p2,X2);
plot(X2,Y2,'color','#F6780A')
s2 = sprintf('y2 = (%.1f) x^2 + (%.1f) x + (%.1f)',p2(1),p2(2),p2(3));
hold on

% linear rise motion -2 mm - 2 mm
x3 = x(188:215);
y3 = y(188:215);
t3 = t(188:215);
p3 = polyfit(x3,y3,1);
X3 = x3(1):-0.01:x3(28);
Y3 = polyval(p3,X3);
plot(X3,Y3,'color','#F6780A')
s3 = sprintf('y3 = (%.1f) x + (%.1f)',p3(1),p3(2));
hold on

% parabolic motion -2 mm
x4 = x(215:488);
y4 = y(215:488);
t4 = t(215:488);
```

```

p4 = polyfit(x4,y4,2);
X4 = x4(1):-0.01:x4(274);
Y4 = polyval(p4,X4);
plot(X4,Y4,'color','#F6780A')
s4 = sprintf('y4 = (%.1f) x^2 + (%.1f) x + (%.1f)',p4(1),p4(2),p4(3));

% linear return motion 0 mm - -2 mm
x5 = x(488:511);
y5 = y(488:511);
t5 = t(488:511);
p5 = polyfit(x5,y5,1);
X5 = x5(1):-0.01:x5(24);
Y5 = polyval(p5,X5);
plot(X5,Y5,'color','#F6780A')
s5 = sprintf('y5 = (%.1f) x + (%.1f)',p5(1),p5(2));
title('Position cam needle segment holders','FontName','Times')
xlabel('Displacement y [mm]','FontName','Times')
ylabel('Displacement z [mm]','FontName','Times')
xlim([0 44])
ylim([-3 3])
daspect([1 1 1])

% Displacement, velocity and acceleration curves
figure(2)
% Displacement curve
subplot(3,1,1)
% linear return motion 2 mm - 0 mm
T1 = t1(1):-0.01:t1(38);
p_T1 = polyfit(t1,y1,1);
Y_T1 = polyval(p_T1,T1);
plot(T1,Y_T1,'color','#36A9E1')
xlabel('Time [s]','FontName','Times')
ylabel('Displacement [mm]','FontName','Times')
xlim([0 6])
ylim([-3 3])
hold on
s_T1 = sprintf('y_T1 = (%.1f) x + (%.1f)',p_T1(1),p_T1(2))

% parabolic motion 2 mm
T2 = t2(1):-0.01:t2(151);
p_T2 = polyfit(t2,y2,2);
Y_T2 = polyval(p_T2,T2);
plot(T2,Y_T2,'--','color','#662483')
hold on
s_T2 = sprintf('y_T2 = (%.1f) x^2 + (%.1f) x + (%.1f)',p_T2(1),p_T2(2),p_T2(3))

% linear rise motion -2 mm - 2 mm
T3 = t3(1):-0.01:t3(28);
p_T3 = polyfit(t3,y3,1);
Y_T3 = polyval(p_T3,T3);
plot(T3,Y_T3,'color','#36A9E1')
hold on
s_T3 = sprintf('y_T3 = (%.1f) x + (%.1f)',p_T3(1),p_T3(2))

% parabolic motion -2 mm
T4 = t4(1):-0.01:t4(274);
p_T4 = polyfit(t4,y4,2);
Y_T4 = polyval(p_T4,T4);
plot(T4,Y_T4,'--','color','#662483')
hold on
s_T4 = sprintf('y_T4 = (%.1f) x^2 + (%.1f) x + (%.1f)',p_T4(1),p_T4(2),p_T4(3))

% linear return motion 0 mm - -2 mm
T5 = t5(1):-0.01:t5(24);
p_T5 = polyfit(t5,y5,1);
Y_T5 = polyval(p_T5,T5);
plot(T5,Y_T5,'color','#36A9E1')
s_T5 = sprintf('y_T5 = (%.1f) x + (%.1f)',p_T5(1),p_T5(2))

```



```

legend({'linear motion','parabolic motion'},'location','best')

% velocity curve
subplot(3,1,2)
syms tt
% linear return motion 2 mm - 0 mm
y1_t = p_T1(1)*tt + p_T1(2);
v1_t = diff(y1_t,tt)
fplot(v1_t,[t1(38) t1(1)],'color','#36A9E1')
xlabel('Time [s]','FontName','Times')
ylabel('Velocity [mm/s]','FontName','Times')
xlim([0 6])
ylim([-7 7])
hold on

% parabolic motion 2 mm
y2_t = p_T2(1)*tt^2 + p_T2(2)*tt + p_T2(3);
v2_t = diff(y2_t,tt)
fplot(v2_t,[t2(151) t2(1)],'--','color','#662483')
hold on

% linear rise motion -2 mm - 2 mm
y3_t = p_T3(1)*tt + p_T3(2);
v3_t = diff(y3_t,tt)
fplot(v3_t,[t3(28) t3(1)],'color','#36A9E1')
hold on

% parabolic motion -2 mm
y4_t = p_T4(1)*tt^2 + p_T4(2)*tt + p_T4(3);
v4_t = diff(y4_t,tt)
fplot(v4_t,[t4(274) t4(1)],'--','color','#662483')
hold on

% linear return motion 0 mm - -2 mm
y5_t = p_T5(1)*tt + p_T5(2);
v5_t = diff(y5_t,tt)
fplot(v5_t,[t5(24) t5(1)],'color','#36A9E1')
hold off
legend({'linear motion','parabolic motion'},'location','best')

% acceleration curve
subplot(3,1,3)
% linear return motion 2 mm - 0 mm
a1_t = diff(v1_t,tt);
fplot(a1_t,[t1(38) t1(1)],'color','#36A9E1')
xlim([0 6])
ylim([-30 30])
xlabel('Time [s]','FontName','Times')
ylabel('Acceleration [mm^2/s]','FontName','Times')
hold on

% parabolic motion 2 mm
a2_t = diff(v2_t,tt);
fplot(a2_t,[t2(151) t2(1)],'--','color','#662483')
hold on

% linear rise motion -2 mm - 2 mm
a3_t = diff(v3_t,tt);
fplot(a3_t,[t3(28) t3(1)],'color','#36A9E1')
hold on

% parabolic motion -2 mm
a4_t = diff(v4_t,tt);
fplot(a4_t,[t4(274) t4(1)],'--','color','#662483')
hold on

% linear return motion 0 mm - -2 mm
a5_t = diff(v5_t,tt);

```

```
fplot(a5_t,[t5(24) t5(1)],'color','#36A9E1')
hold off
legend({'linear motion','parabolic motion'},'location','best')
sgtitle('Displacement curves in z-
direction','FontName','Times','fontweight','bold','fontsize',10)
```

Appendix H. Technical drawings manual actuator

The following technical drawings can be found in this appendix:

- Assembly drawing:
 - Manual actuator
- Part drawings:
 - Double cone outside
 - Lock ring (no offset)
 - Housing top
 - Manual translation ring
 - Housing bottom
 - Double cone inside
 - Cam top
 - Needle segment holder
 - Selector
 - Cam bottom
 - Lock ring (4 mm offset)

4

3

2

1

F

E

D

C

B

A

F

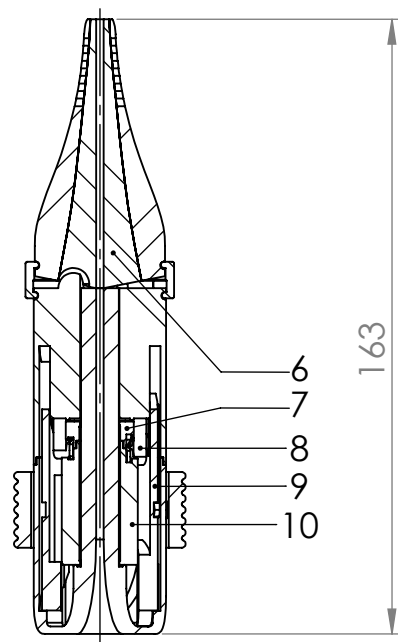
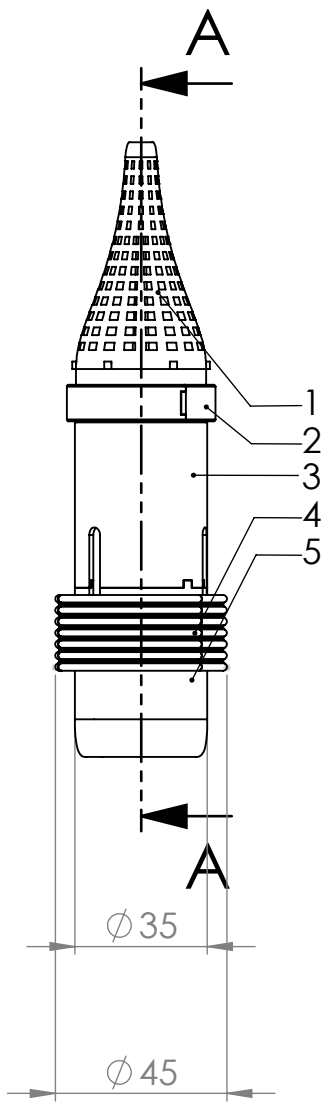
E

D

C

B

A



Scale 1:5

SECTION A-A

ITEM NO.	PART NUMBER	DESCRIPTION	QTY.
1		Double cone outside	1
2		Lock ring (no offset)	2
3		Housing top	1
4		Manual translation ring	3
5		Housing bottom	1
6		Double cone inside	1
7		Cam top	1
8		Needle segment holder	6
9		Selector	1
10		Cam bottom	1

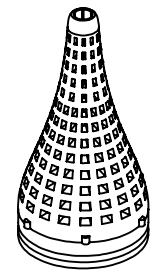
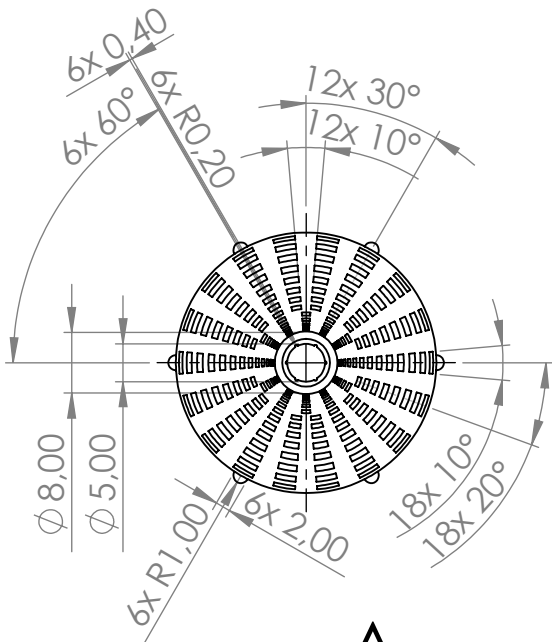
UNLESS OTHERWISE SPECIFIED: DIMENSIONS ARE IN MILLIMETERS SURFACE FINISH: TOLERANCES: LINEAR: ANGULAR:			FINISH:	DEBURR AND BREAK SHARP EDGES	DO NOT SCALE DRAWING	REVISION
NAME	SIGNATURE	DATE			TITLE:	
DRAWN						
CHK'D						
APP'VD						
MFG						
Q.A				MATERIAL:	DWG NO.	
					Manual actuator A4	
				WEIGHT:	SCALE:1:2	SHEET 1 OF 1

4

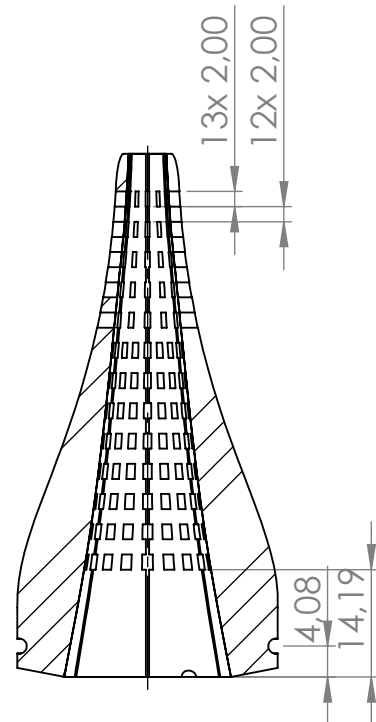
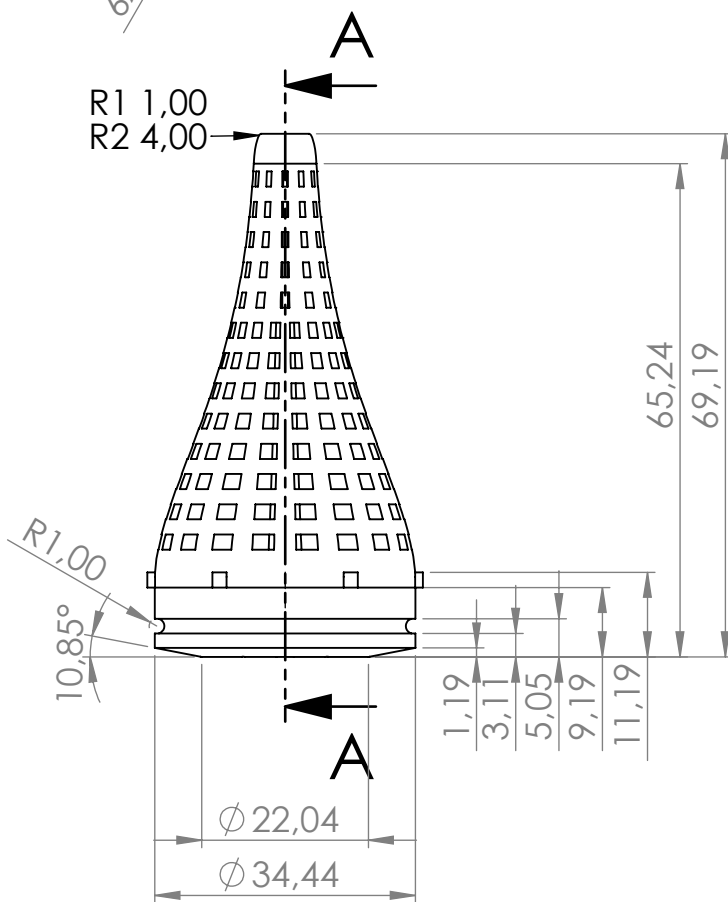
3

2

1



Scale 1:2



SECTION A-A

UNLESS OTHERWISE SPECIFIED:
DIMENSIONS ARE IN MILLIMETERS
SURFACE FINISH:
TOLERANCES:
LINEAR:
ANGULAR:

FINISH:

DEBURR AND
BREAK SHARP
EDGES

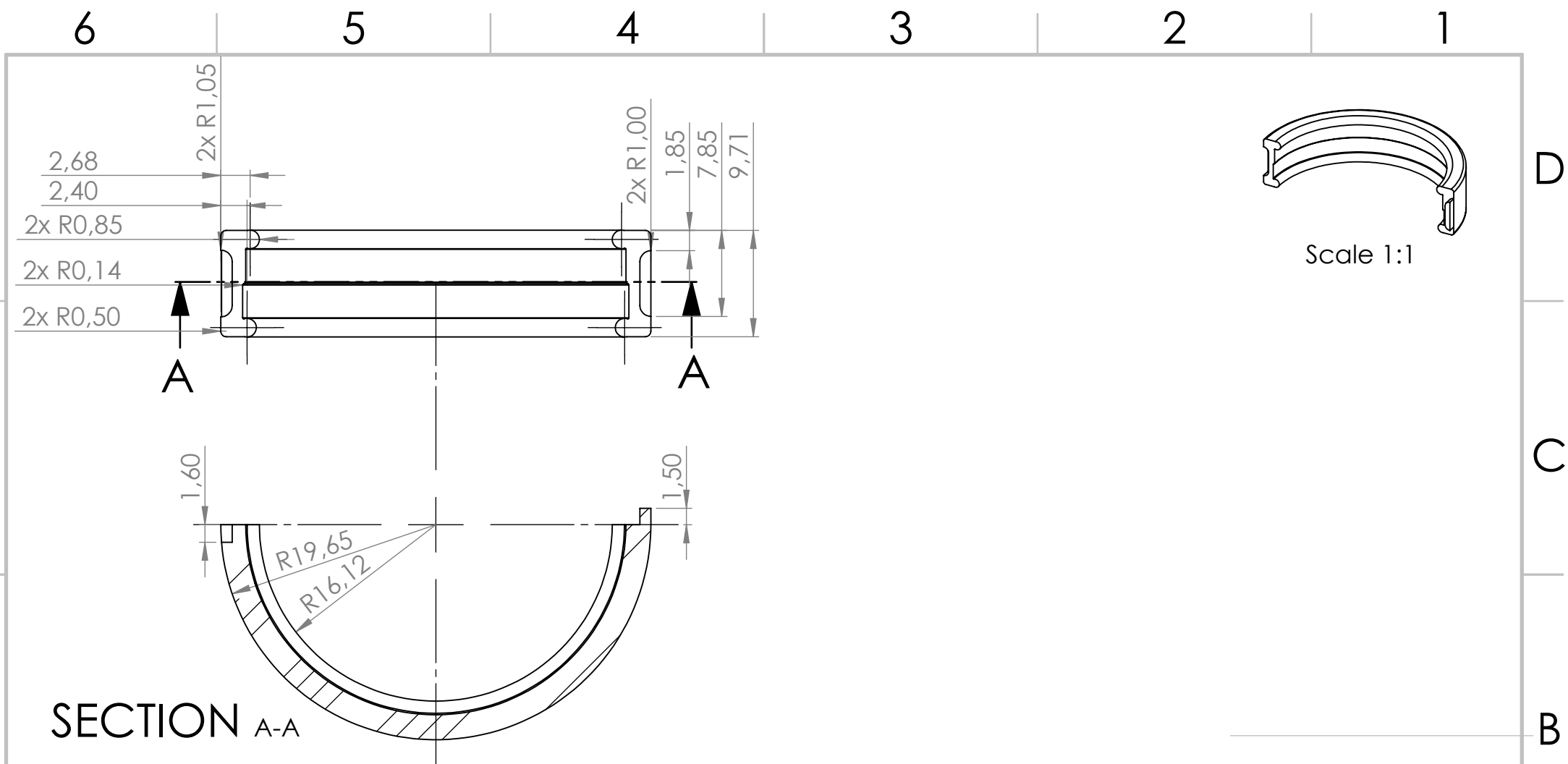
DO NOT SCALE DRAWING

REVISION

NAME	SIGNATURE	DATE		
DRAWN				
CHK'D				
APPV'D				
MFG				
Q.A				
MATERIAL:			DWG NO.	
Dental Model V2			A4	
QUANTITY: 1			Double cone outside	
WEIGHT:			SCALE:1:1	
			SHEET 1 OF 1	

TITLE:

Double cone outside



SECTION A-A

UNLESS OTHERWISE SPECIFIED: DIMENSIONS ARE IN MILLIMETERS SURFACE FINISH: TOLERANCES: LINEAR: ANGULAR:				FINISH:		DEBURR AND BREAK SHARP EDGES		DO NOT SCALE DRAWING		REVISION	
								TITLE:			
DRAWN				NAME		SIGNATURE		DATE			
CHK'D											
APPV'D											
MFG											
Q.A								MATERIAL: Dental Model V2		DWG NO.	
								QUANTITY: 2		Lock ring (no offset) ⁴	
								WEIGHT:		SCALE:2:1	
										SHEET 1 OF 1	

4

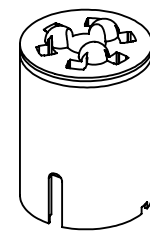
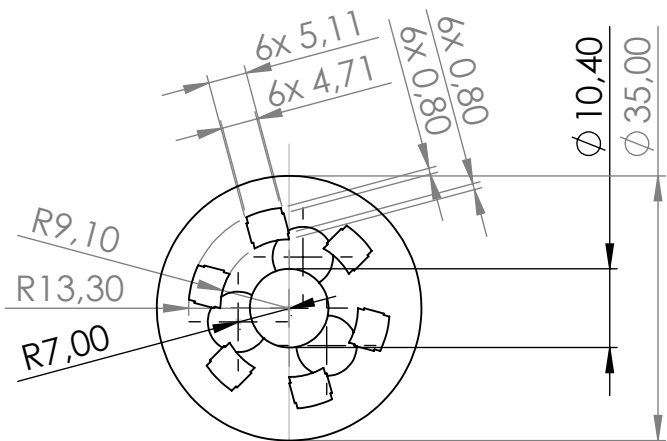
3

2

1

F

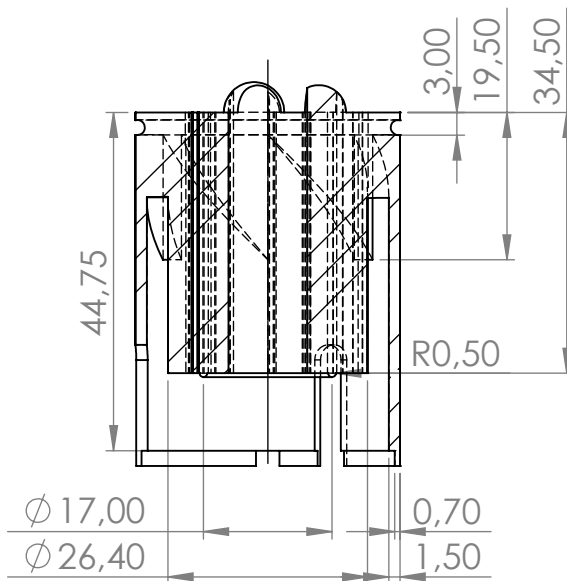
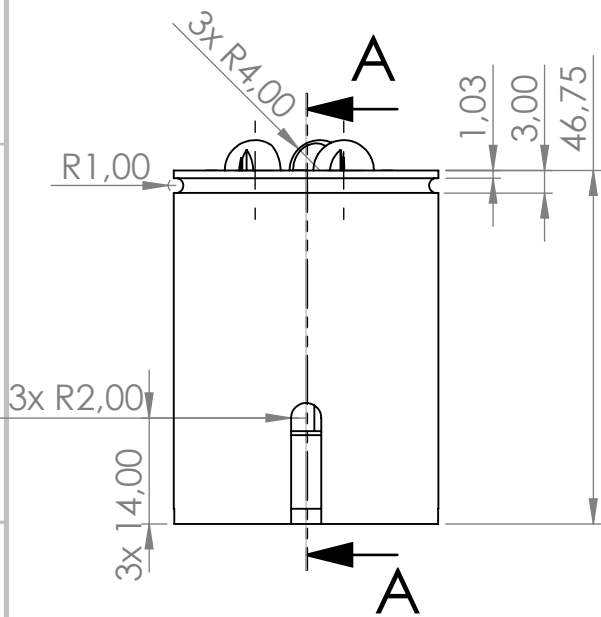
F



Scale 1:2

E

E



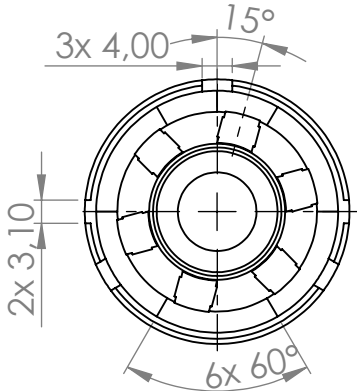
SECTION A-A

D

D

C

C



B

B

UNLESS OTHERWISE SPECIFIED: DIMENSIONS ARE IN MILLIMETERS SURFACE FINISH: TOLERANCES: LINEAR: ANGULAR:			FINISH:		DEBURR AND BREAK SHARP EDGES		DO NOT SCALE DRAWING		REVISION		
DRAWN			SIGNATURE		DATE		TITLE:				
CHK'D											
APPV'D											
MFG											
Q.A							MATERIAL:		DWG NO.		
							PLA		Housing top		
							QUANTITY:1		A4		
							WEIGHT:		SCALE:1:1		
									SHEET 1 OF 1		

A

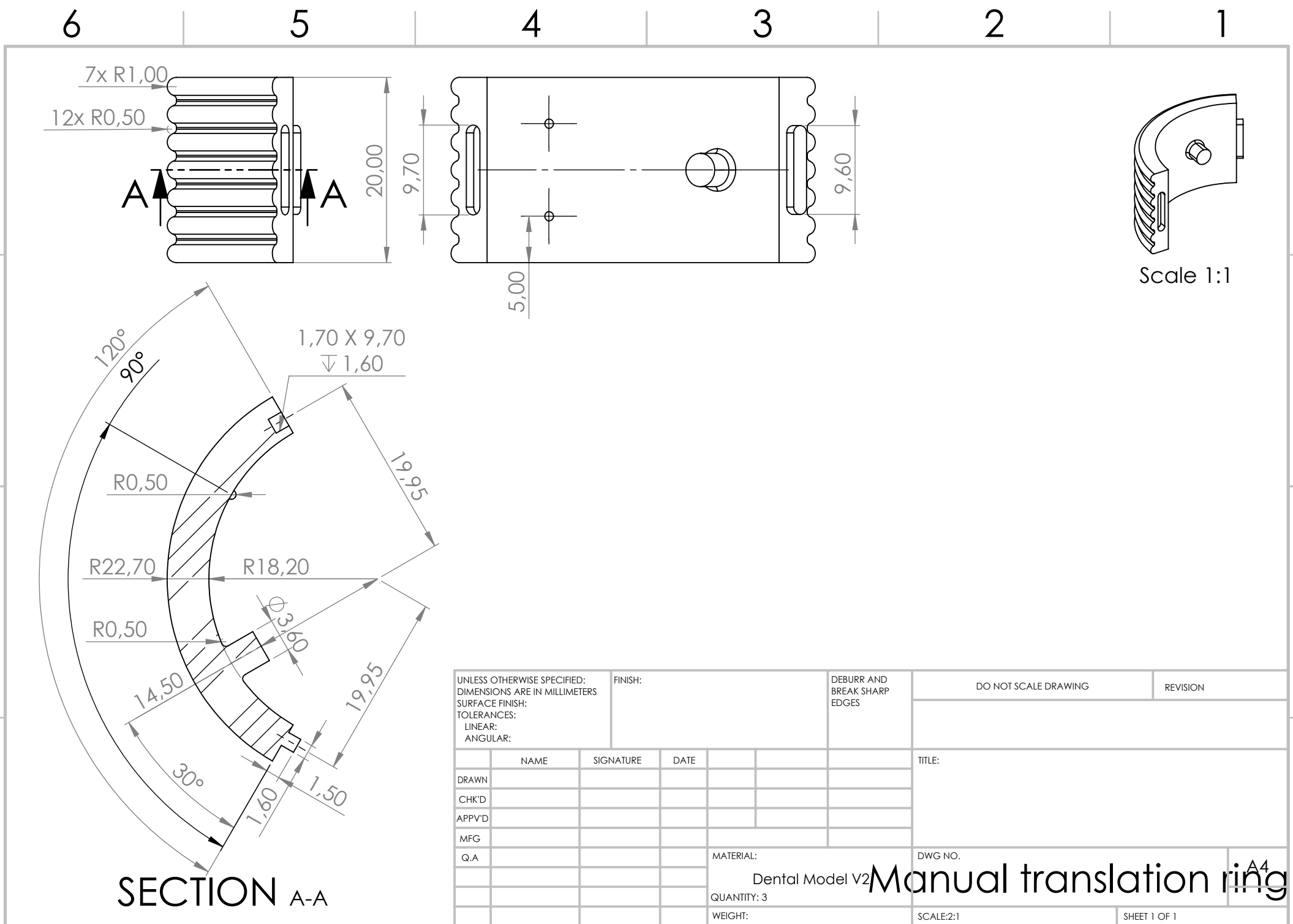
A

4

3

2

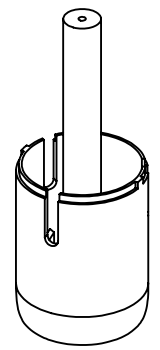
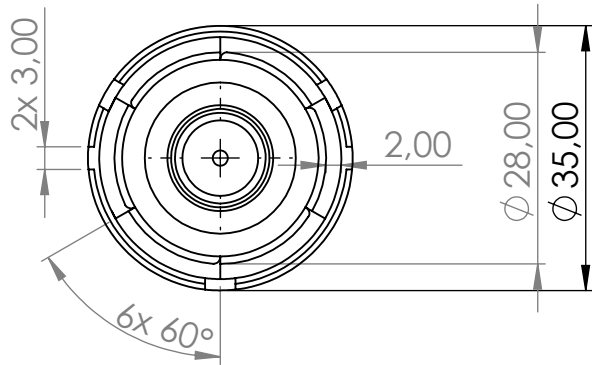
1



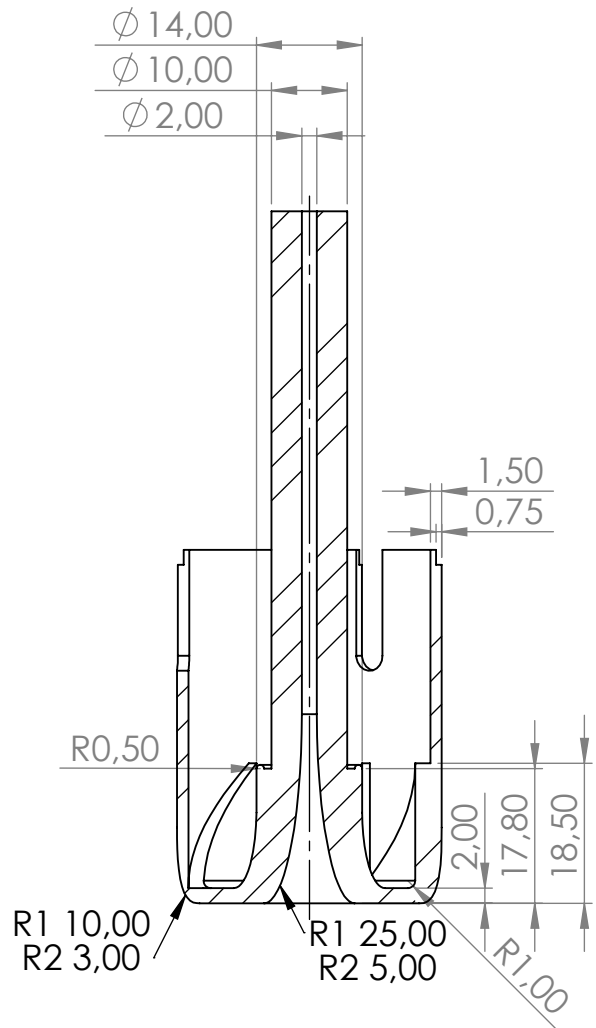
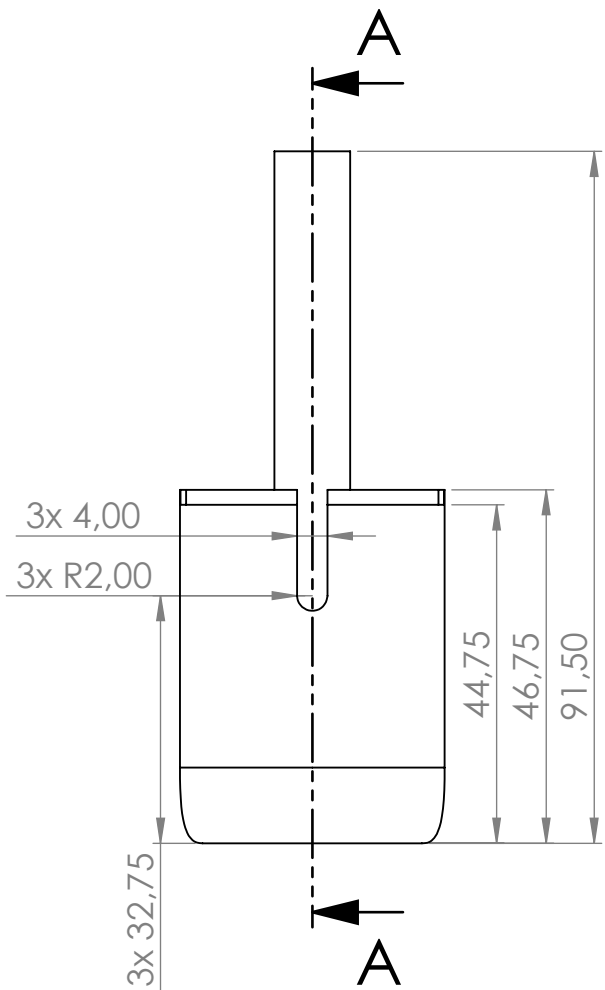
4 3 2 1

F
E
D
C
B
A

F
E
D
C
B
A



Scale 1:2



SECTION A-A

UNLESS OTHERWISE SPECIFIED: DIMENSIONS ARE IN MILLIMETERS SURFACE FINISH: TOLERANCES: LINEAR: ANGULAR:			FINISH:	DEBURR AND BREAK SHARP EDGES	DO NOT SCALE DRAWING	REVISION
NAME	SIGNATURE	DATE	TITLE:			
DRAWN			DWG NO. Housing bottom A4			
CHK'D						
APPV'D						
MFG						
Q.A						
MATERIAL: PLA			QUANTITY: 1		SCALE: 1:1	
WEIGHT:					SHEET 1 OF 1	

4

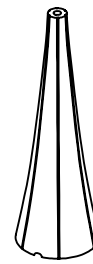
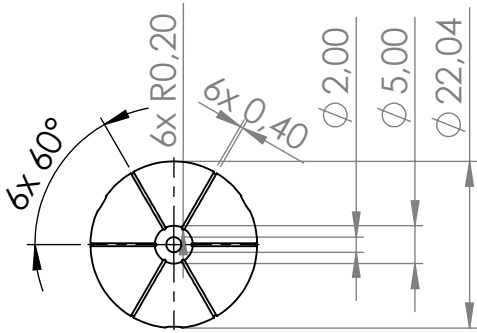
3

2

1

F

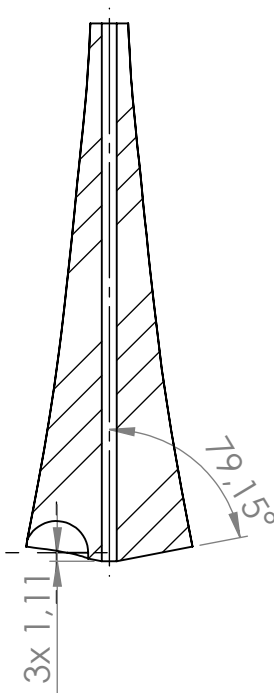
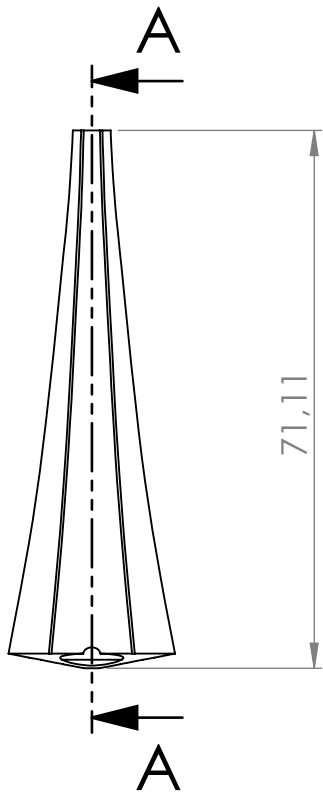
F



Scale 1:2

E

E



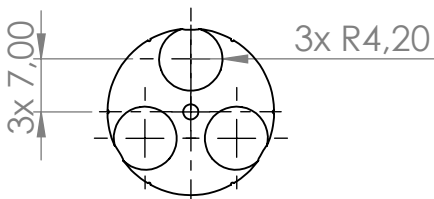
SECTION A-A

D

D

C

C



B

B

UNLESS OTHERWISE SPECIFIED: DIMENSIONS ARE IN MILLIMETERS SURFACE FINISH: TOLERANCES: LINEAR: ANGULAR:			FINISH:	DEBURR AND BREAK SHARP EDGES	DO NOT SCALE DRAWING	REVISION
NAME	SIGNATURE	DATE	TITLE:			
DRAWN			MATERIAL: Dental Model V2 QUANTITY: 1 WEIGHT:			
CHK'D						
APPV'D						
MFG						
Q.A			DWG NO.	Double cone inside		A4
			SCALE:1:1	SHEET 1 OF 1		

A

A

4

3

2

1

4

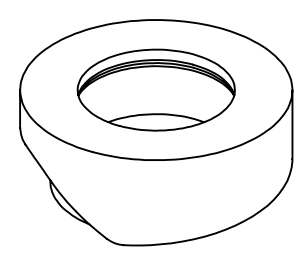
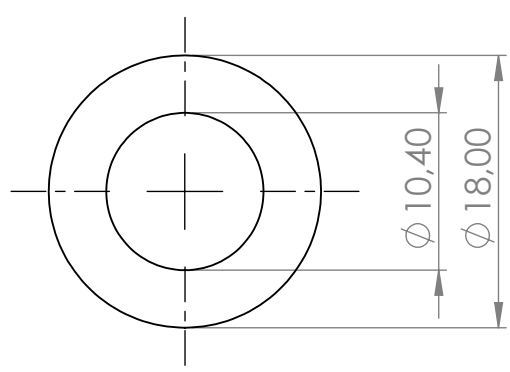
3

2

1

F

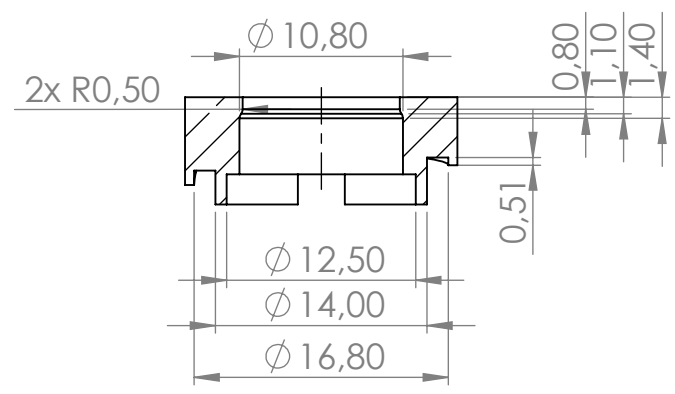
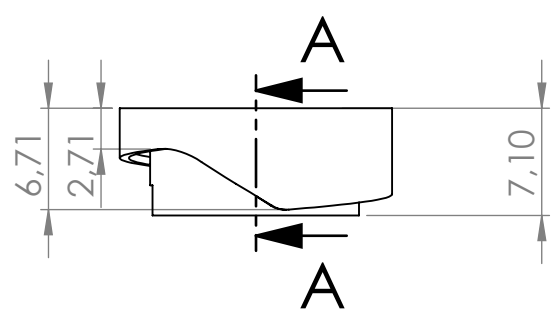
F



Scale 1:1

E

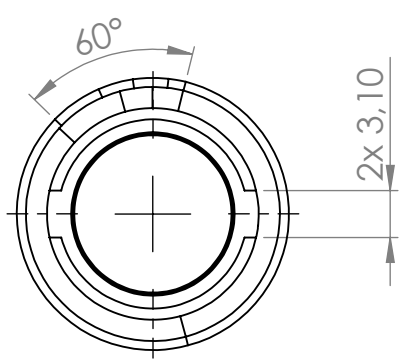
E



SECTION A-A

D

D



C

C

B

B

UNLESS OTHERWISE SPECIFIED: DIMENSIONS ARE IN MILLIMETERS SURFACE FINISH: TOLERANCES: LINEAR: ANGULAR:			FINISH:		DEBURR AND BREAK SHARP EDGES		DO NOT SCALE DRAWING		REVISION		
DRAWN			SIGNATURE		DATE		TITLE:				
CHK'D											
APPV'D											
MFG											
Q.A							MATERIAL:		DWG NO.		A4
							Dental Model V2		Cam top		
							QUANTITY: 1		SCALE:2:1		SHEET 1 OF 1
							WEIGHT:				

A

A

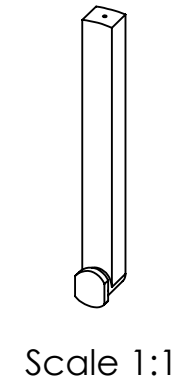
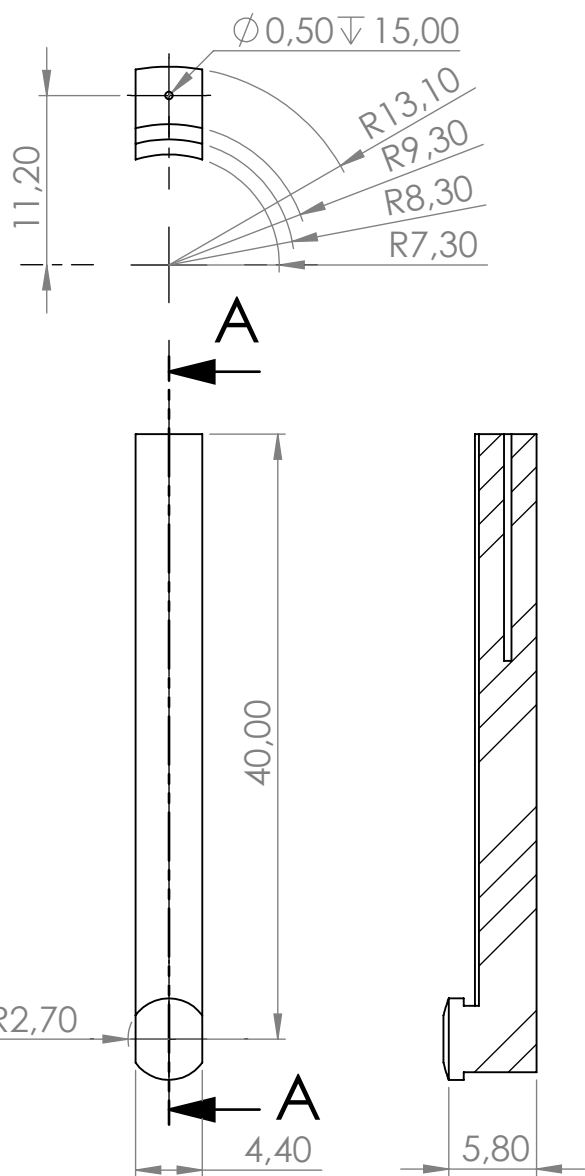
4

3

2

1

6 5 4 3 2 1



SECTION A-A

UNLESS OTHERWISE SPECIFIED: DIMENSIONS ARE IN MILLIMETERS SURFACE FINISH: TOLERANCES: LINEAR: ANGULAR:				FINISH:		DEBURR AND BREAK SHARP EDGES		DO NOT SCALE DRAWING		REVISION	
DRAWN				NAME		SIGNATURE		DATE		TITLE:	
CHK'D											
APP'VD											
MFG											
Q.A											
				MATERIAL:		Dental Model V		DWG NO.		A4	
				QUANTITY:		6		SCALE:2:1		SHEET 1 OF 1	
				WEIGHT:							

Needle segment holder

6 5 4 3 2 1

4

3

2

1

F

F

E

E

D

D

C

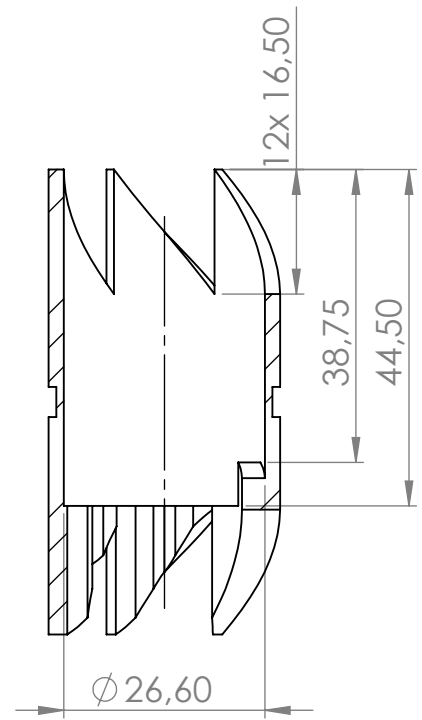
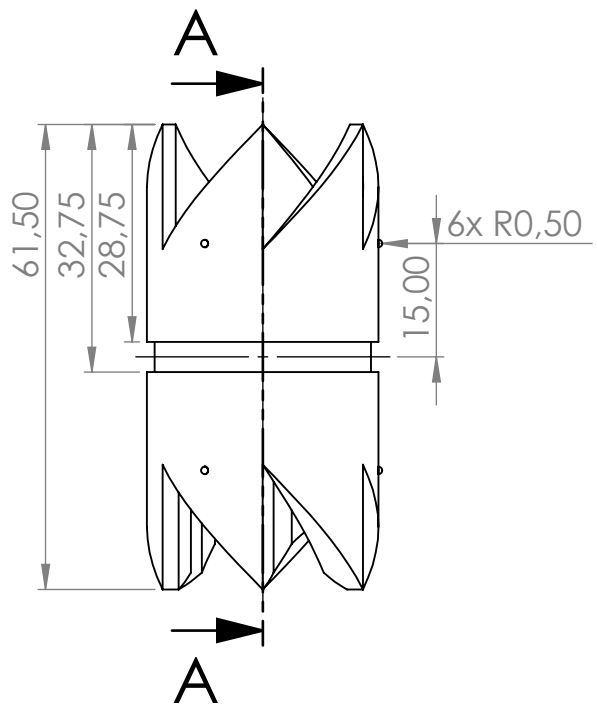
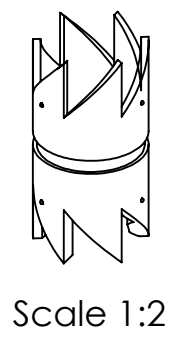
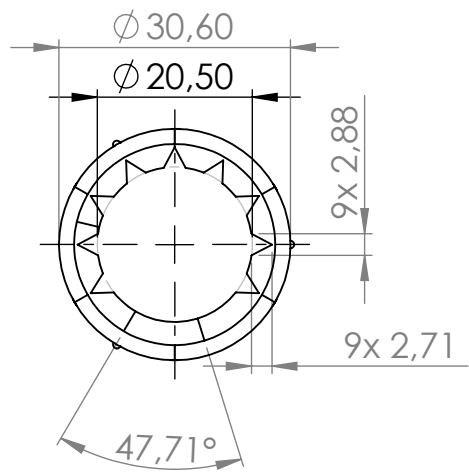
C

B

B

A

A



SECTION A-A

UNLESS OTHERWISE SPECIFIED: DIMENSIONS ARE IN MILLIMETERS SURFACE FINISH: TOLERANCES: LINEAR: ANGULAR:			FINISH:		DEBURR AND BREAK SHARP EDGES		DO NOT SCALE DRAWING		REVISION	
DRAWN			SIGNATURE		DATE		TITLE:			
CHK'D										
APPV'D										
MFG										
Q.A							MATERIAL:		DWG NO.	
							Dental Model V2		Selector	
							QUANTITY: 1		A4	
							WEIGHT:		SCALE:1:1	
									SHEET 1 OF 1	

4

3

2

1

4

3

2

1

F

F

E

E

D

D

C

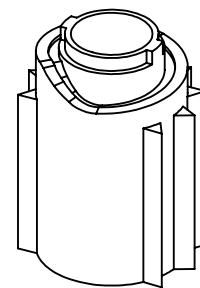
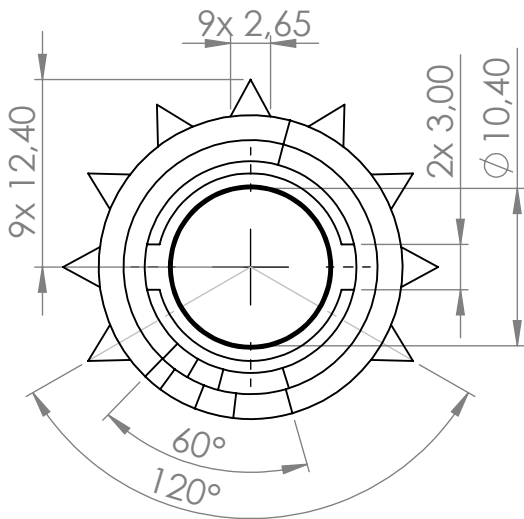
C

B

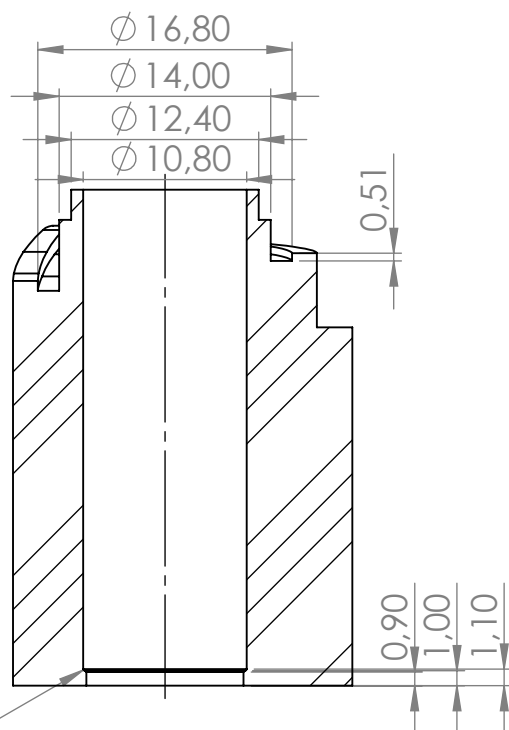
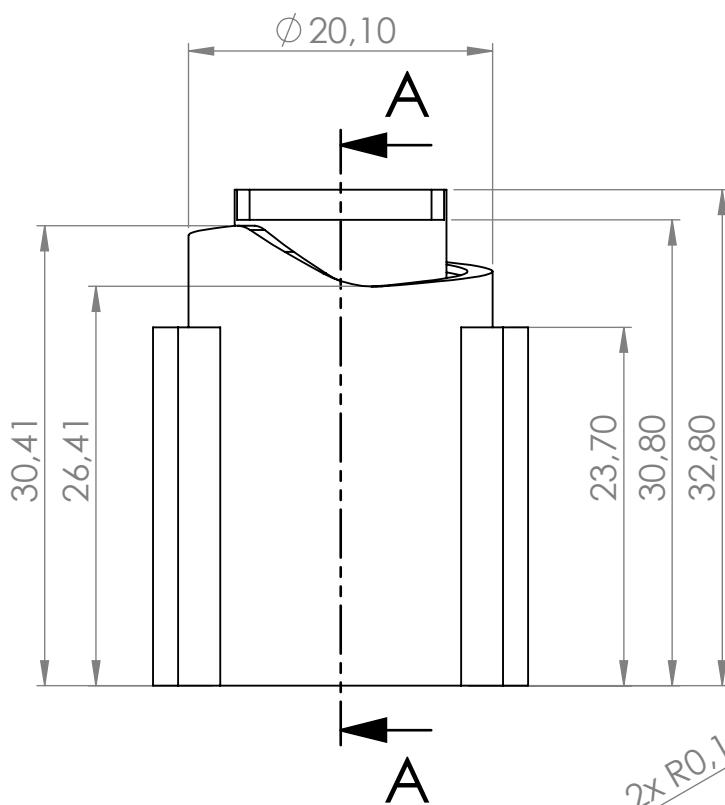
B

A

A



Scale 1:1



SECTION A-A

UNLESS OTHERWISE SPECIFIED:
DIMENSIONS ARE IN MILLIMETERS
SURFACE FINISH:
TOLERANCES:
LINEAR:
ANGULAR:

FINISH:

DEBURR AND
BREAK SHARP
EDGES

DO NOT SCALE DRAWING

REVISION

NAME	SIGNATURE	DATE		
DRAWN				
CHK'D				
APP'V'D				
MFG				
Q.A				
MATERIAL:			PLA	
QUANTITY:			1	
WEIGHT:				

TITLE:

DWG NO.

Cam bottom

A4

SCALE:2:1

SHEET 1 OF 1

4

3

2

1

4

3

2

1

F

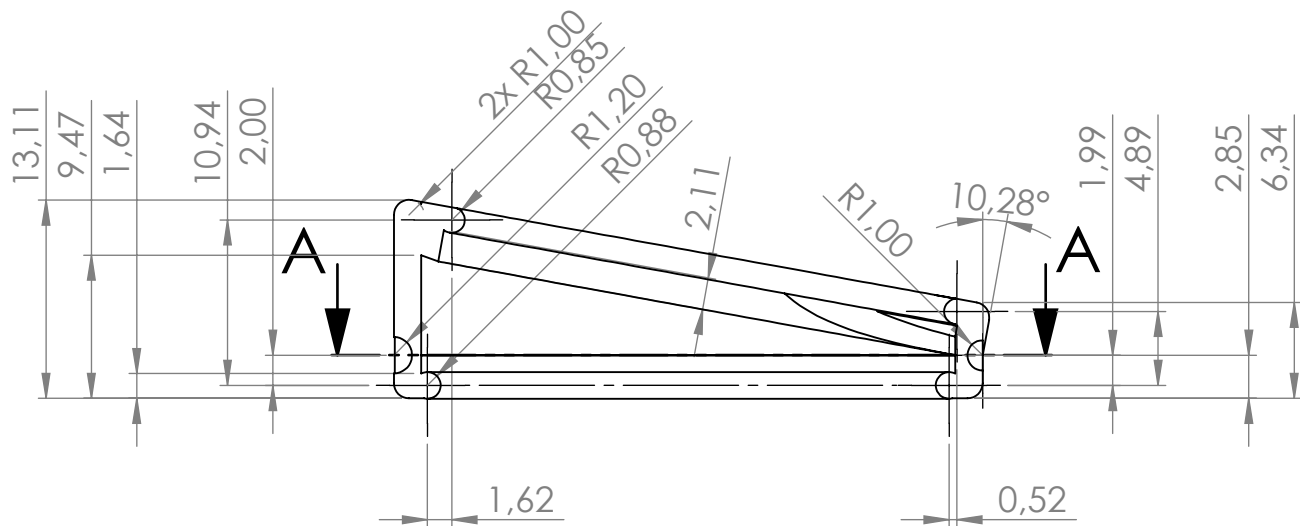
F



Scale 1:1

E

E

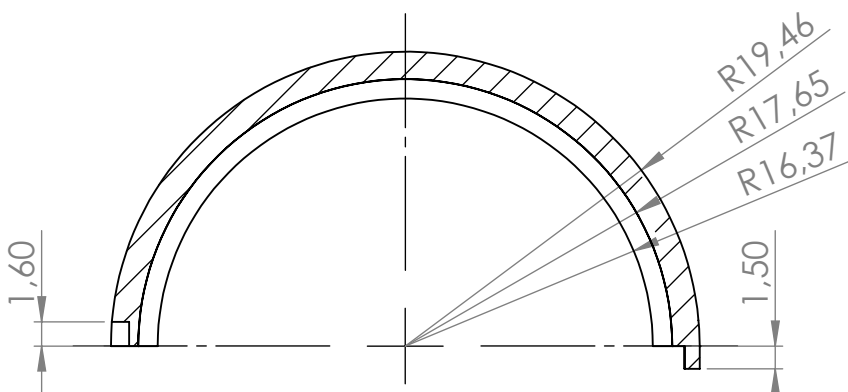


D

D

C

C



SECTION A-A

B

B

UNLESS OTHERWISE SPECIFIED: DIMENSIONS ARE IN MILLIMETERS SURFACE FINISH: TOLERANCES: LINEAR: ANGULAR:			FINISH:	DEBURR AND BREAK SHARP EDGES	DO NOT SCALE DRAWING	REVISION
NAME	SIGNATURE	DATE			TITLE:	
DRAWN						
CHK'D						
APPV'D						
MFG						
Q.A				MATERIAL: Dental Model V2	DWG NO.	Dental Model V2
				QUANTITY: 2	Lock ring (4 mm offset)	
				WEIGHT:	SCALE:2:1	QUANTITY: 2
						SHEET 1 OF 1

A

A

4

3

2

1

Appendix I. Magnetic resonance parameters

This appendix contains the magnetic resonance (MR) parameters set for the MR compatibility tests and *ex vivo* experiment in this study.

I.1 Nomenclature

The meaning of the parameters was retrieved from Blink [35] (Table I-I). For more information about magnetic resonance imaging (MRI) physics, we refer the reader to Blink [35].

Table I-I. Definitions of important parameters and terms in MRI.

Parameter/term	Meaning
TR	Repetition time, cycle time between two corresponding pulses.
TE	Echo time, time between the middle of the first pulse to the middle of the echo.
TI	Inversion time, time between the 180° inverting pulse and the 90° pulse.
Number of averages	Number of times the scan is repeated, tool used to increase the amount of signal in the image, but it also affects the acquisition time.
Flip angle	The number of degrees the net magnetisation is rotated, in the range from 1-180°.
Field of view	How much of the patient/component that is inside the MRI scanner we can see in the MR image.
Matrix size	Acquisition matrix, it determines the spatial resolution of the MR image.
Slice thickness	The axial resolution of the scan. The slice thickness influences the amount of signal and the sharpness of the MR image. Increasing the slice thickness increase the signal but lowers the resolution.
Slice spacing	The movement of the scanner for scanning the next slice.
Spin echo	90° pulse followed by a 180° pulse to rephase the spins
Gradient echo	Single radiofrequency pulse with a gradient polarity reversal to rephase the spins.
3D FLASH	Three-dimensional fast low-angle shot imaging MRI sequence. It is a fast gradient echo sequence that combines a low-flip angle radio-frequency excitation pulses and subsequent gradient reversal.
T1 relaxation	What happens in the Z direction with the magnetisation vector. Also called spin-lattice relaxation because the energy is released to surrounding tissue (lattice).
T2 relaxation	What happens in the X-Y plane with the magnetisation vector. Also called spin-spin relaxation because it depends on the interactions between protons in the surrounding. T2 is quicker than T1.
β_0	Main magnetic field.

I.2 MR compatibility tests

Table I-II shows the MR parameters set for the MR images of the MR compatibility tests.

Table I-II. MR parameters for MR compatibility tests of the prototype materials and needle sample used in this study.

Parameter	3D gradient echo, prototype materials	3D gradient echo, needle materials
TR [ms]	15	20
TE [ms]	0	0
TI [ms]	1000	1000
Number of averages	1	8
Flip angle [°]	25	20
Field of view [mm x mm]	32.00x64.00 x0.50	32.00x64.00 x0.25
Matrix size	256x256	256x128
Slice thickness [mm]	0.50	0.25
Slice spacing [mm]	0.50	0.25

As had been demonstrated in previous publications [69, 118], the angle of the needle with regards to the direction of the main magnetic field, affected the size of the needle artefact. Figs I-1c and I-1d and Table I-III show that an increased angulation of the needle with respect to the magnetic field resulted in an increased artefact diameter of the needle. When aligning the needle with the magnetic field, the image artefacts became of almost the same size as the actual needle, comparable to the results stated by Penzkofer et al. [118] and Bartels et al. [119] for needles and vascular stents, respectively. In the *ex vivo* experiment, the needle was aligned with the direction of the main magnetic field, to minimise image artefacts caused by the Nitinol needle

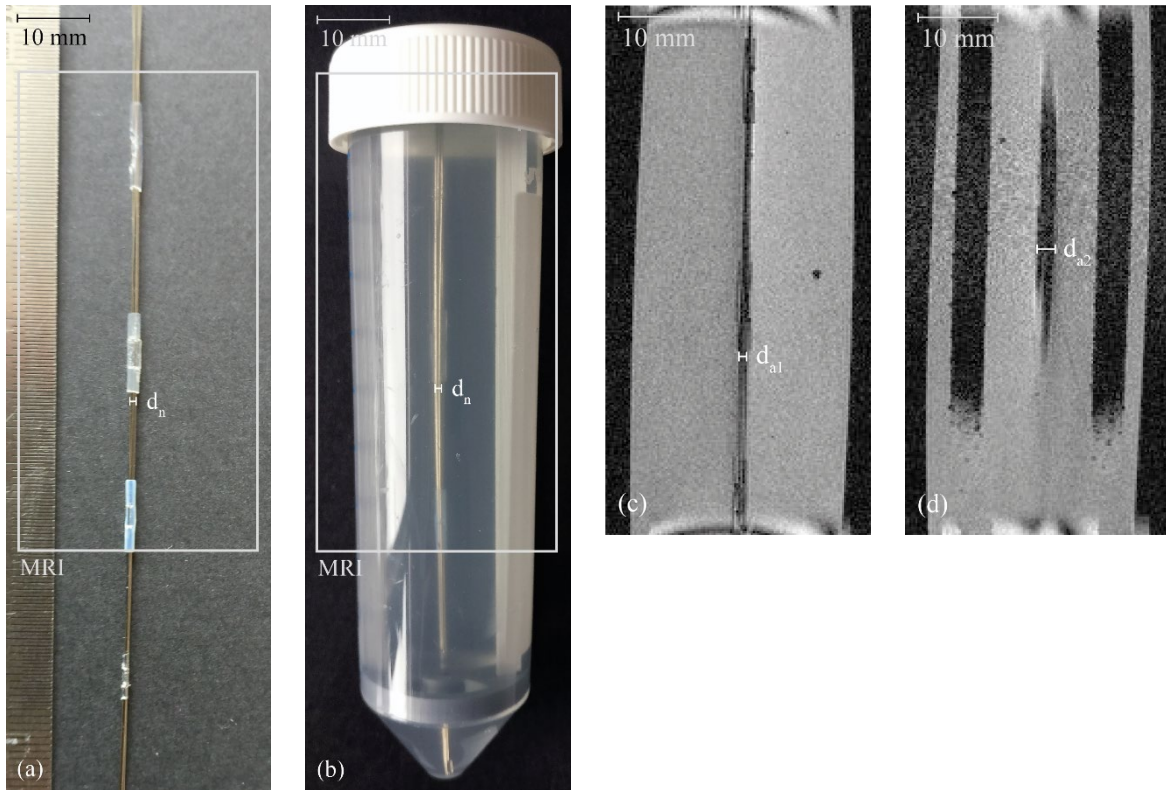


Fig. 1-1. (a) Photograph of the needle sample used in MR compatibility test 2, d_n is the diameter of the needle, the rectangle visualises what part can be seen in the MR images. (b) Photograph of the needle sample in a Falcon tube filled with 5 wt% gelatine. (c) MR image of the needle sample where the needle is placed parallel to the direction of the magnetic field, d_{a1} is the diameter of the artefact of the needle. (d) MR image of the needle sample where the needle is placed under an angle with regards to the direction of the magnetic field, d_{a2} is the diameter of the artefact of the needle.

Table I-III. Needle diameter and artefact size of the diameter compared for the needle parallel to the direction of the magnetic field, β_0 , and at an angle with regards to B_0 .

Image	Photograph, d_n	MRI parallel to magnetic field, d_{a1}	MRI angle with respect to magnetic field, d_{a2}
Diameter [mm]	1.0	1.1	2.4

1.3 Ex vivo experiment

Table I-VI shows the MR parameters set for the MR images of the *ex vivo* prostate experiment.

Table I-VI. MR parameters for *ex vivo* prostate experiment.

Parameter	T1 weighted fast spin echo	3D gradient echo
TR [ms]	100	20
TE [ms]	0	0
TI [ms]	1000	1000
Number of averages	1	2
Flip angle [°]	40	10
Field of view [mm x mm]	60.00x60.00 x1.00	52.00x52.00 x0.29
Matrix size	192x160	192x192
Slice thickness [mm]	1.00	0.29
Slice spacing [mm]	6.00	0.29
Acquisition time [min:s]	0:16	6:09

Appendix J. Original MR images *ex vivo* experiment

This appendix contains the original MR images of the *ex vivo* prostate tissue experiment and the measurements performed during the experiment, including the measurements after every set of five cycles. In Section 5, the MR images contain colour indications for the needle, tissue, sides of the box, and the reference point in the box to measure the slip ratio. Fig. J-I shows the original MR images without the colour indications.

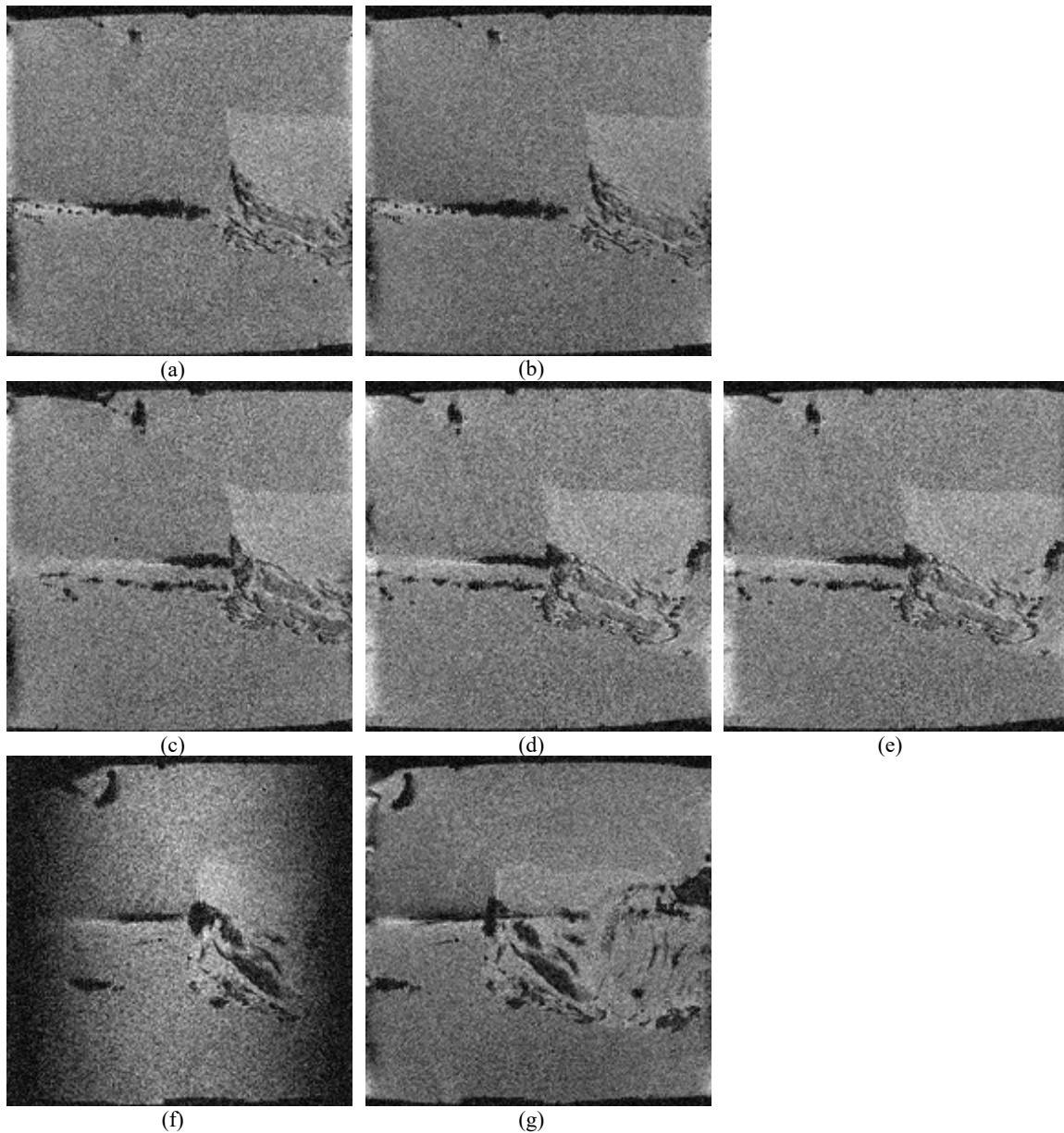


Fig. J-1. MR images of the needle inside *ex vivo* prostate tissue embedded in agar. Each row represents one measurement number. The first column shows the initial frame where the tip is positioned inside the agar in front of the prostate tissue. The second column shows the frame after actuation for five cycles. The third column shows the frame after the second actuation for five cycles. The figure continues on the next page.

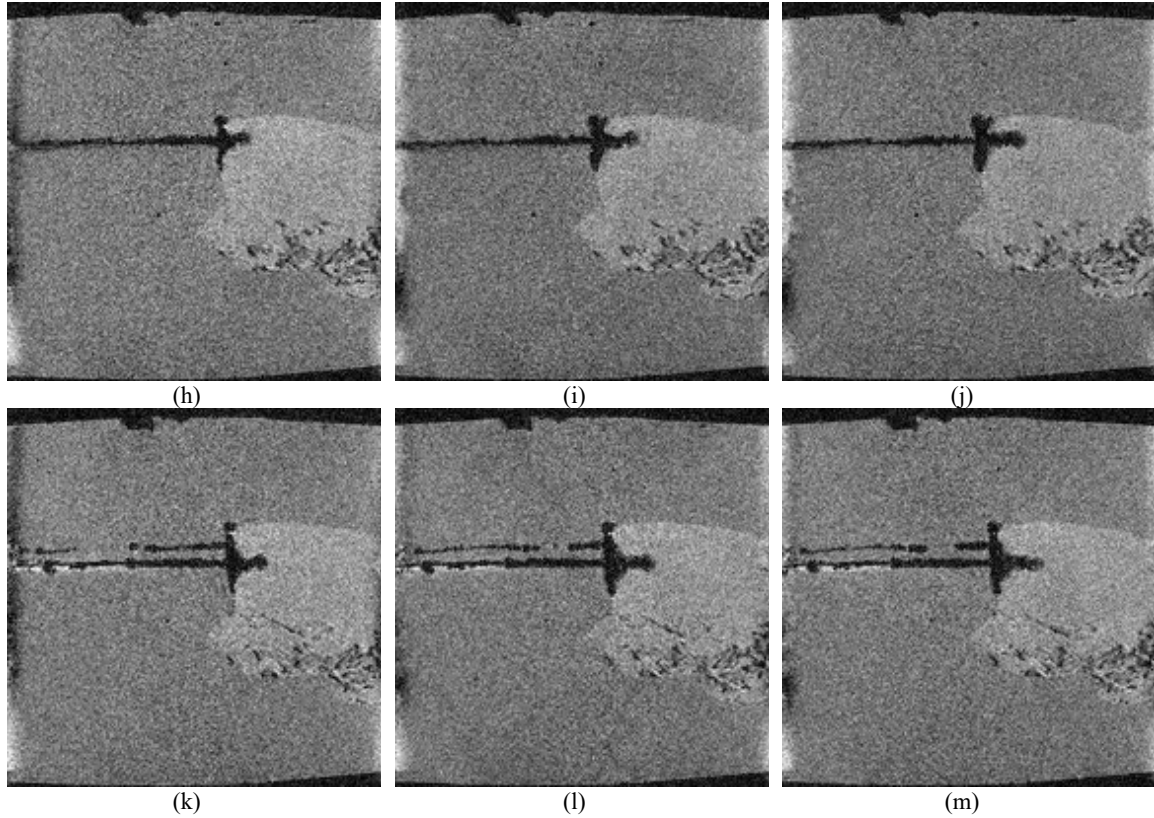


Fig. J-1. MR images of the needle inside the agar and *ex vivo* prostate tissue. Each row represents one measurement number. The first column shows the initial frame where the tip is positioned inside the agar in front of the prostate tissue. The second column shows the frame after actuation for five cycles. The third column shows the frame after the second actuation for five cycles.

Table J-I shows the results of the *ex-vivo* evaluation, including the results after every set of five cycles of actuation.

Table J-I. Results of the *ex vivo* evaluation. For each measurement, the following information is reported: the insertion hole used on the box, where hole 9 is the centre hole, travelled distance [mm] of the box, number of cycles needed to travel that distance, theoretical travelled distance [mm] that the box would have travelled if no slip occurred, and $slip_{ratio}$. The travelled distance, theoretical travelled distance and $slip_{ratio}$ are shown for the entire measurement and for each set of five cycles.

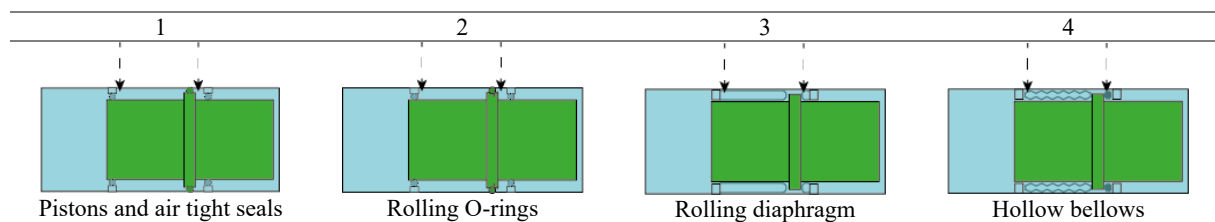
Measurement number	Insertion hole	Initial insertion depth [mm]	Travelled distance [mm] of the box	Cycles	Theoretical travelled distance [mm]	$slip_{ratio}$
1	10	42.4	0	5	20	1.0
2	9	45.0	5.8	10	40	0.86
			2.7	1 st 5 cycles	20	0.87
			3.1	2 nd 5 cycles	20	0.85
3	8	48.6	10.0	5	20	0.50
4	6	50.4	2.9	10	40	0.93
			1.9	1 st 5 cycles	20	0.91
			1.0	2 nd 5 cycles	20	0.95
5	7	51.8	1.6	10	40	0.96
			1.4	1 st 5 cycles	20	0.93
			0.2	2 nd 5 cycles	20	0.99

Appendix K. Design pneumatic actuator

K.1 Design directions

For pneumatic actuation, mechanical designs such as bellows actuators, rolling diaphragm actuators, and pistons in combination with O-rings were described in the scientific literature [120, 121]. Pistons require sealing tolerances. Sealing tolerances are difficult to achieve with an additive manufacturing process, and they introduce high friction forces [120]. Rolling diaphragm actuators exhibit low friction and do not require seals [121]. However, the available printable photopolymers cannot sustain the high material strains required by the mechanical design of the rolling diaphragm actuators [120]. Bellows actuators do not require seals and conceive a frictional force only in case of a linear guide in contact with the bellows [122]. Table K-I visualises the different design directions to make the Ovipositor MRI-Needle pneumatically actuated.

Table K-I. Design directions for pneumatic actuation of the Ovipositor MRI-Needle.



K.2 State of the art 3D-printed soft bellows

In the scientific literature, bellows actuators were produced using either direct additive manufacturing or additive manufactured moulds [123, 124]. Dämmer et al. [122] produced TangoBlackPlus (TB+) and Agilus30 (A30) soft bellows structures using PolyJet printing. The bellows had a wall thickness of 2 mm and were actuated with positive air pressure with the pressure difference, Δp , varied between 0 and 14 kPa. The results showed that the A30 bellows withstood higher numbers of repeated loadings than the bellows produced out of TB+. Lau [125] compared PolyJet printed Agilus30 bellows to Multi Jet Fusion printed polyamide (HP PA 12) bellows in different shapes. The difference between a wall thickness of 1.5 or 3.0 mm showed to be insignificant for the deflection behaviour of the bellows. The bellows were tested with a positive pressure difference varied between 0 and 20 kPa. The Agilus30 parts showed a greater deflection at lower pressures than the HP PA 12 bellows.

Anver et al. [126] applied fused filament fabrication (FFF) to produce a soft gripper with rectangular prism-shaped chambers. The authors were able to produce airtight chambers by splitting the computer-aided design model into vertical plates that were stacked uniformly with printer-dependent gaps in between them. The thermoplastic elastomer FilaFlex (Recreus) was used as the filament to produce the bellows with a wall thickness of 0.64 mm at the thinnest parts. Experiments showed a resulting force of 2.59 N at a positive pressure difference of 100 kPa. Mutlu et al. [127] also applied FFF to produce a NinjaFlex (NinjaTek), a thermoplastic polyurethane, gripper with an average wall thickness of 0.58 mm based on bellows. The gripper unfolds when negative pressure was applied to contract to middle bellows, while positive pressure was applied to the outer fingers to extend them. The negative pressure was applied by a vacuum pump (Single Stage Rotary Valve). Experiments showed that the negative pressure at the middle bellows played a key role in the actuation, compared to positive pressure applied to the finger bellows.

Berger [128] produced a pneumatic gripper, comprising a pair of bellows, of Accura SI10 (3D Systems) resin using stereolithography. The authors stated that bellows with a wall thickness of 0.7 mm could be produced without failures, whereas scaling by 0.5 damaged the bellows. The bellows were actuated with a positive air pressure with Δp varied between 0.05 and 0.6 MPa. Experiments showed a gripping force of 25 N and fracture after two gripping cycles applying a pressure of 0.4 MPa.

K.3 Bellows prototype

We prototyped 3D-printed bellows using stereolithography (SLA) on the Formlabs Form 3B. The bond created by the SLA process is air-tight as the process creates a chemical bond by cross-linking photopolymers across layers.

The model of the bellows is based on the S-shaped geometry for a linear bellow-type actuator. The prototype is printed in its expanded position, with an angle of 60° , as this is an angle that is possible to print using SLA (Formlabs Form 3B). The bellows was designed using Solidworks software (Dassault Systems Solidworks Corporation; Waltham, MA, USA). Four models of a single bellows fold with a wall thickness ranging from 0.2 mm to 0.8 mm were developed, in order to test the thinnest wall thickness that is possible to print for this model on the Formlabs Form 3B. Fig. K-1 and Table K-II provide information about the dimensions of the bellows models.

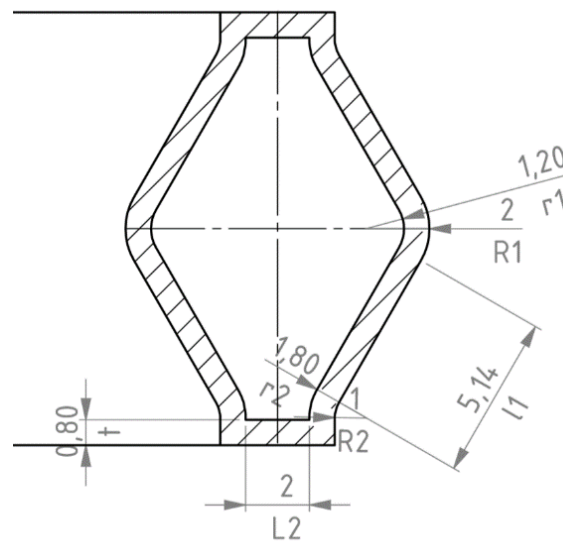
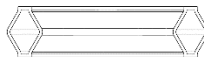
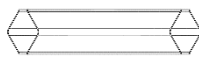
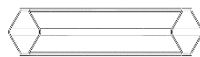



Fig. K-1. Visualisation of the cross-section of a 0.8-mm bellows fold, showing the design parameters.

Table K-II: Dimensions [mm] of the Solidworks models of the bellow folds with different wall thicknesses.

	Model bellows_08 Minimum wall thickness for flexible 80A material	Model bellows_02 Minimum wall thickness Formlabs general	Model bellows_03	Model bellows_04
				
Wall thickness, t	0.8	0.2	0.3	0.4
Outer radius outer fold, $R1$	2	2	2	2
Inner radius outer fold, $r1$	1.2	1.8	1.7	1.6
Outer radius inner fold, $R2$	1	1	1	1
Inner radius inner fold, $r2$	0.2	0.8	0.7	0.6
Vertical part, $L1$	2	2	2	2
Vertical part printed, $l1$	5.14	5.14	5.14	5.14
Height single fold, H	6	6	6	6
Vertical inner part, $L2$	3.6	3.6	3.6	3.6

Contracted central diameter, D_c	46.2	45.0	45.2	45.4
Contracted outer diameter, D	61.4	59.0	59.4	59.8
Contracted inner diameter, d	31	31	31	31

In order to test the flexibility of the bellows printed in Durable Resin using the Formlabs Form 3B SLA printer, we tested different wall thicknesses. At a 0.2-mm wall thickness, it is not possible to print the bellows fold. Although the webpage of Formlabs stated that the minimum wall thickness possible to print Durable Resin on the Form 3B is 0.2 mm, the Preform software (Formlabs) indicated that this wall thickness is impossible to print. The prototype with a wall thickness of 0.3 mm was printable and turned out to be flexible (Fig. K-2a). The cushioning effect due to the forces of the foil in the 3D printer that pulls the material is visible in the prototype. When compressing the prototype, the prototype did not maintain its annular shape. The bellows model can be improved by adding rims at the insides of the folds to obtain shape retention during expansion and contraction. A water immersion test showed that the prototype was airtight. A test with air pressure showed that at a pressure $p = 200$ kPa the prototype failed at the position of the drain hole (Fig. K-2b). Lastly, the prototype with a wall thickness of 0.8 mm is impossible to deform by hand, thus a wall thickness of 0.8 mm is too stiff for the bellows design (Fig. K-2c).

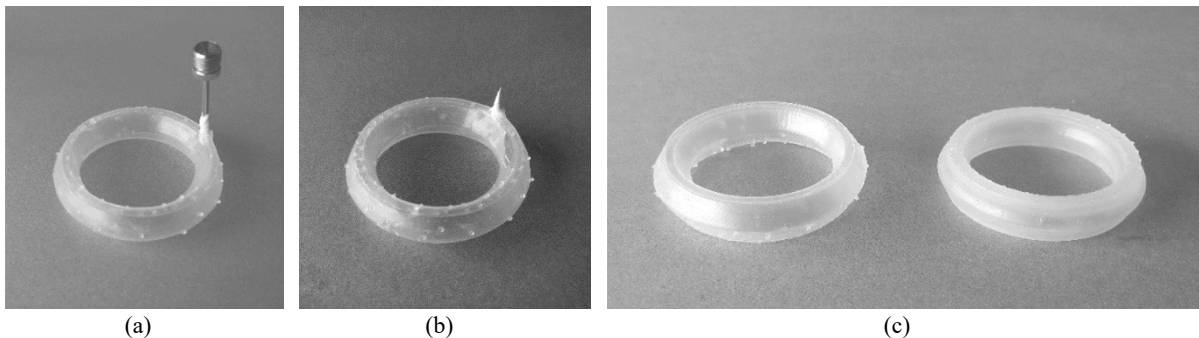


Fig. K-2. (a) 0.3-mm prototype before testing with air pressure, (b) 0.3-mm prototype after testing with air pressure showing the gap where the prototype tore, (c) left: 0.3-mm prototype, right: 0.8-mm prototype.

K.3.1 Bellows design 1: multiple folds

For a complete bellows design, multiple folds should be stacked on top of each other. To maintain the annular shape during contraction, the inner folds of the bellows were enforced by locally increasing the wall thickness of the bellows. To convert the translating motion of the bellows to the selector, a rim at the top of the bellows was added that fits within a circumferential slot in the selector (Fig. K-3b). The rim of the bellows and the slot in the selector transmit the translating motion of the bellows but allow rotation of the selector.

The four stacked folds were printed with a 0.3-mm wall thickness. The Preform software generated more support for the four-fold-design than for the single-fold design. During removal of the support structures, the walls of the three upper folds of the prototype started to tear. The changes in the forces on the walls caused by the change in the presence and absence of the support pillars probably caused the tearing of the walls. The lower fold contained less support structure, comparable to the single-fold design, and maintained its untorn walls. Fig. K-3c shows the torn walls of the prototype with four stacked folds.

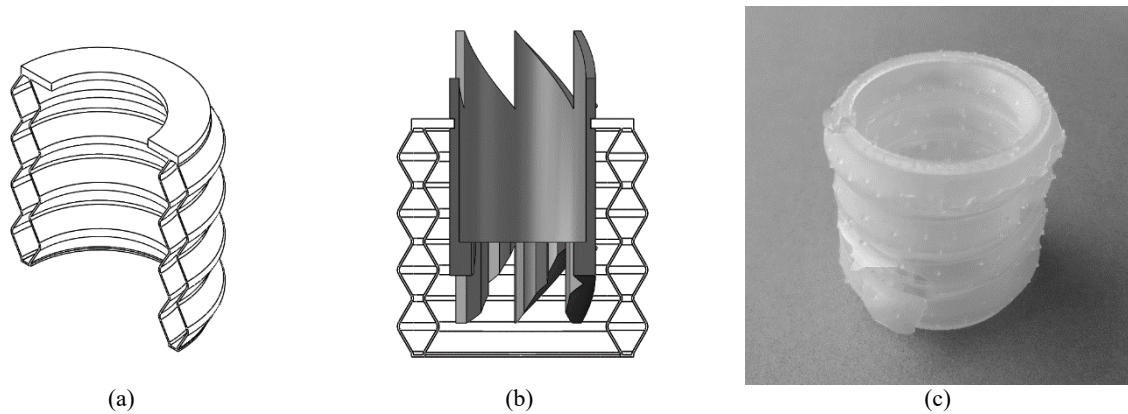


Fig. K-3: First bellows design with a rim at the top that fits into the circumferential slot of the selector, (a) Solidworks model of bellows, (b) Solidworks model with rim inside the slot of the selector, (c) prototype showing the tears in its walls after removing the support material.

K.3.2 Bellows design 2: separate folds

To overcome the problem of the changing forces on the bellows walls when removing the support structures, the 0.3-mm wall thickness bellows folds were printed separately and designed to be assembled afterwards using glue. The number of folds of the bellows depends on the angle of the expanded and contracted position and the required stroke. We assumed that the folds contract from 60° to 0° using a negative pressure source. Furthermore, we assumed that the walls contract to a circular shape. Five folds are required to obtain a 26-mm stroke. The design consists of an upper fold with a rim to interact with the selector, three middle folds, and one lower fold that contains an air inlet. The folds contain four circumferentially distributed holes to transmit the air from the lower fold(s) to the upper fold(s) to allow the extension of the bellows. Figs K-4a,b show the bellows design.

Before removing the support, the prototype was washed in alcohol to remove residual photopolymer resin. The prototype tore after washing it in alcohol (Fig. K-4c). We can conclude that the walls do not tear because of the removal of the support structures.

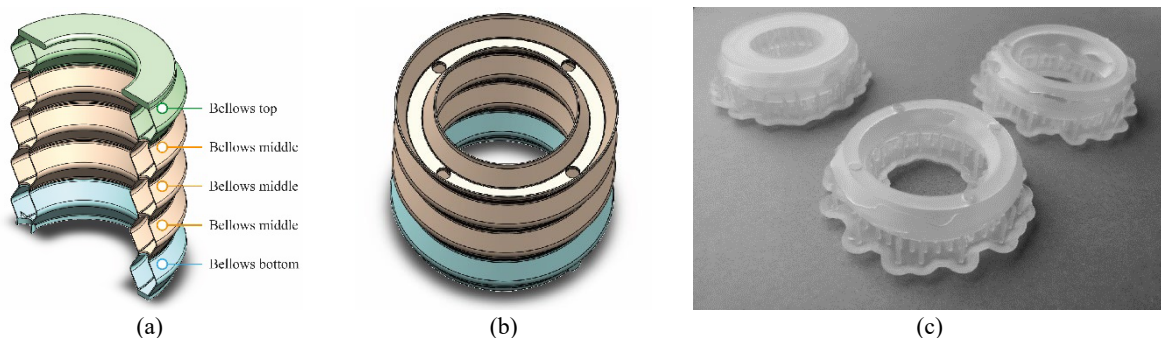


Fig. K-4. (a) Cross-section of the second bellows design consisting of five separately printed folds, (b) cross-section showing the holes to transmit the air from the lower folds to the upper folds to allow extension of the bellows, (c) image of the torn walls after washing the print in alcohol, the support is still in place.

K.3.3 Bellows design 3: separate folds

For the third bellows design, the single-fold prototype was printed at a 0.4-mm wall thickness to determine if the wall thickness affects the tearing process of the walls. The design was again for five separately printed folds to be assembled afterwards using glue.

The third prototype is flexible, pressing the top of the fold results in the contraction of the prototype. The walls of the prototype tore again after cutting away the support material that was connected to the walls (Fig. K-5). We can conclude that a 0.1-mm change in wall thickness does not seem to have a significant influence on the tearing of the walls and the flexibility of the prototype.

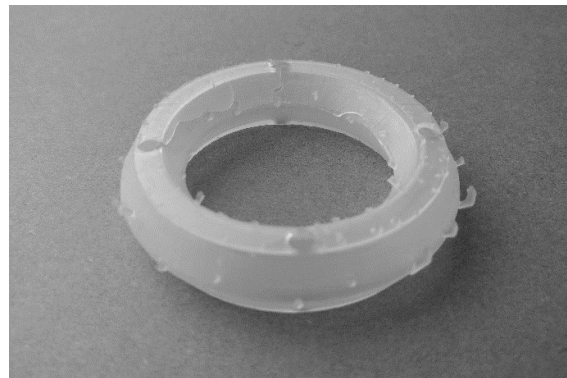
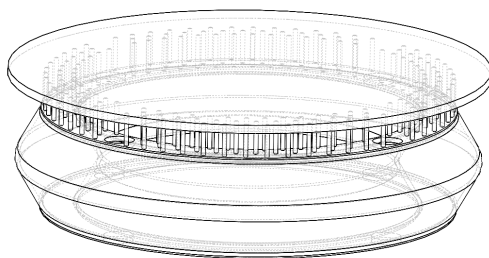


Fig. K-5. Stereolithography printed prototype of the third bellows design with a 0.4-mm wall thickness showing torn walls after cutting away support.

K.3.4 Bellows design 4: separate folds with support

The preform software generated support that touches the walls of the print. We designed the support in Solidworks to prevent tearing because of the Preform-generated support structures. The support was designed to connect a 1-mm disc at the base plate of the single-fold prototype (Fig. K-6a), instead of also connecting the disc to the sides of the prototype like the Preform software would suggest.

After cutting away the support, the 0.4-mm wall thickness bellows started to tear from the holes that transmit the air between the different folds (Fig. K-6b). The holes turned out to be a weak spot of the bellows that might have caused the walls to tear.



(a)



(b)

Fig. K-6. Third bellows design, (a) Solidworks model of the middle fold with self-designed support and (b) stereolithography printed prototype showing the torn walls.

K.3.5 Bellows design 5: multiple folds with support

The fifth bellows were designed as one part to prevent tearing of the bellows at the air holes. The wall thickness was set to 0.4 mm, with a locally increased wall thickness at the inner folds in order to maintain the annular shape during contraction. Furthermore, in order to prevent the accumulation of the support forces at the walls, the support was designed using Solidworks software, similar to the fourth bellows design.

The prototype remained airtight after washing in alcohol and removing the support structures. The airtight bellows were actuated with a syringe. Fig. K-7 shows that the bellows did not retain its annular shape in the under-vacuum state.

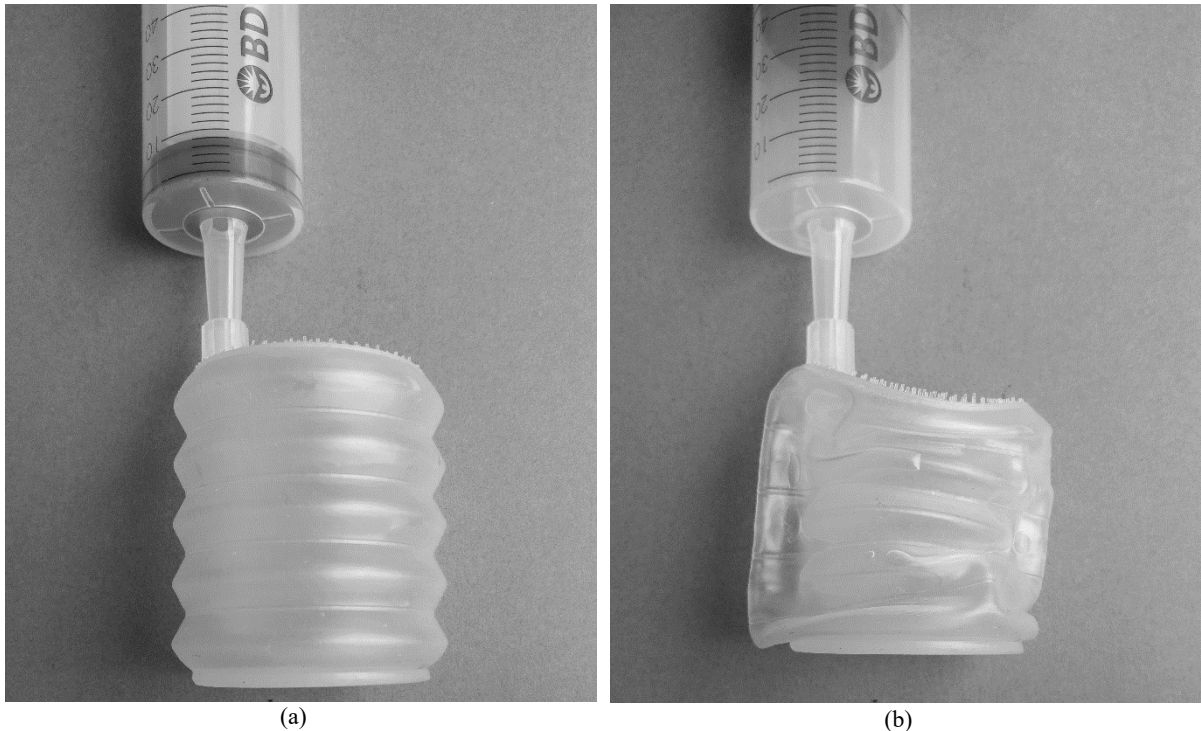


Fig. K-8. Stereolithography printed airtight annular bellows, (a) in its neutral state and (b) in its under-vacuum state.

K.3.6 Post-processing

The flexibility of the bellows changes during the curing process, the strain at fracture in tension of the durable resin changes from 75% to 55% when going from the green to the post-cured state. Curing the prototype of the first bellows design for five minutes resulted in a stiff and brittle prototype. This post-cured prototype could not be compressed without tearing the walls of the bellows further. Therefore, we concluded that the bellows should be used in their green state.

K.4 Conclusions bellows

We showed that it is possible to print airtight bellows using the SLA technology on the Formlabs Form 3B printer. To maintain flexibility and prevent friction, we recommend to use Durable resin in its green state and print the material with a 0.4-mm wall thickness. Furthermore, the support should not touch the walls of the bellows, as this results in stress accumulation and eventually tearing of the walls.

To implement the bellows in the design of the steerable needle to be used in an MRI-room, the bellows need to be actuated with alternating negative and positive air pressure. The MRI-room is equipped with pressurised air. A system to regulate the air pressure and convert it to negative pressure is required. A vacuum ejector can convert positive pressure to negative pressure using a Venturi nozzle. A three-way valve can connect the bellows to either the positive pressure supply or the negative pressure supply. Fig. K-9 shows an impression of the set-up of the pneumatically-actuated steerable needle.

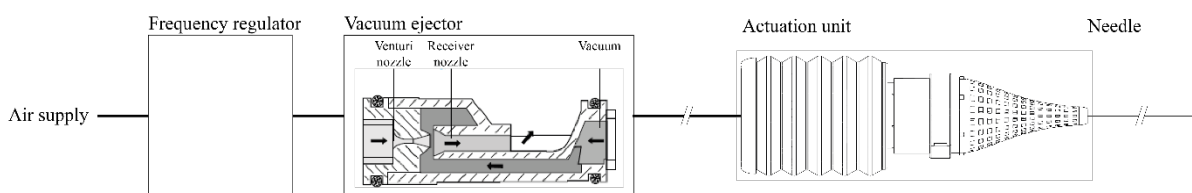


Fig. K-9. Artist impression of the set-up of the pneumatically-actuated Ovipositor MRI-Needle.

Appendix L. Technical drawings pneumatic actuator

In Fig. L-1, the exploded view of the pneumatic actuation unit can be seen. The components that were adjusted compared to the manual actuation unit are the bellows, housing bottom, housing top, selector bottom, and selector top.

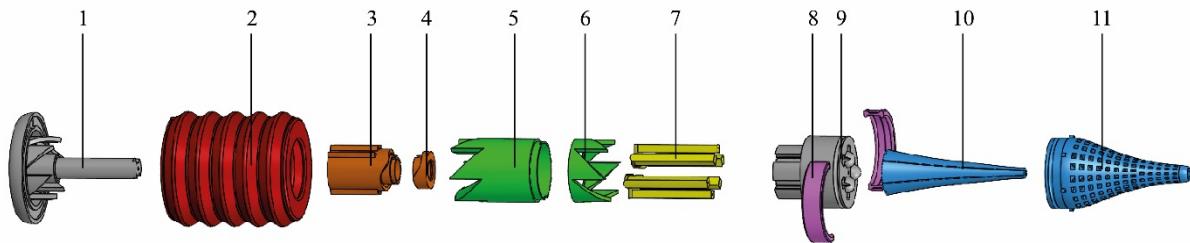


Fig. L-1. (a) Exploded view of the pneumatic actuation unit. The actuation unit consists of a housing pneumatic bottom (1), bellows (2) cam bottom (3), cam top (4), selector bottom (5), selector top (6), needle segment holder (7), lock ring (0 mm) (8), housing pneumatic top (9), double cone inside (10), and double cone inside (11).

The following technical drawings can be found in this appendix:

- Assembly drawing:
 - o Pneumatic actuator
- Part drawings:
 - o Housing pneumatic top
 - o Bellows
 - o Housing pneumatic bottom
 - o Selector top
 - o Selector bottom

The part drawings of the components that were not adjusted from the manually actuated Ovipositor MRI-Needle can be found in Appendix H.

4

3

2

1

F

F

E

E

D

D

C

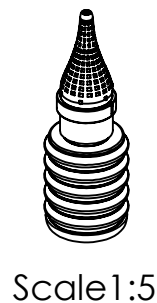
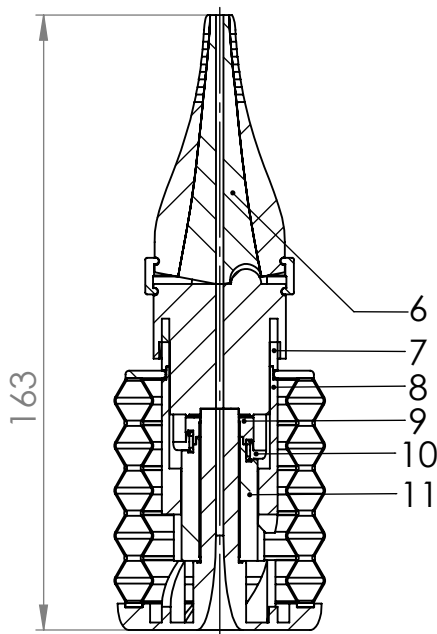
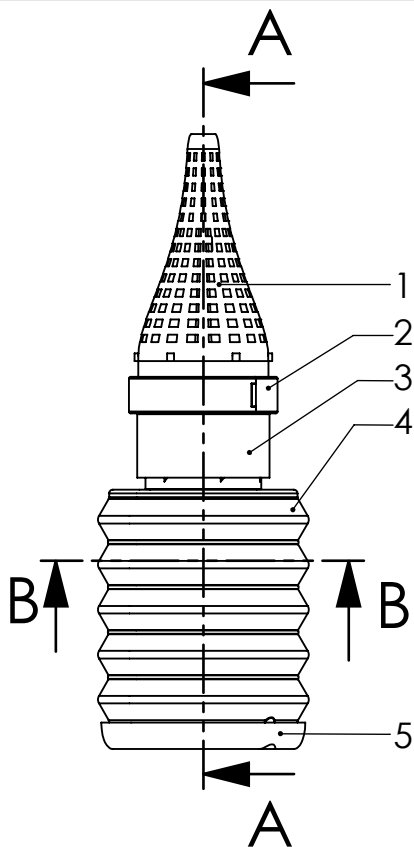
C

B

B

A

A



SECTION A-A



SECTION B-B

ITEM NO.	PART NUMBER	DESCRIPTION	QTY.
1		Double cone outside	1
2		Lock ring (no offset)	2
3		Housing pneumatic top	1
4		Bellows	1
5		Housing pneumatic bottom	1
6		Double cone inside	1
7		Selector top	1
8		Selector bottom	1
9		Cam top	1
10		Needle segment holder	6
11		Cam bottom	1

UNLESS OTHERWISE SPECIFIED: DIMENSIONS ARE IN MILLIMETERS SURFACE FINISH: TOLERANCES: LINEAR: ANGULAR:			FINISH:	DEBURR AND BREAK SHARP EDGES	DO NOT SCALE DRAWING	REVISION
NAME	SIGNATURE	DATE	TITLE:			
DRAWN			Pneumatic actuator			
CHK'D						
APPV'D						
MFG						
Q.A			MATERIAL:	DWG NO.	A4	
WEIGHT:			SCALE:1:2		SHEET 1 OF 1	

4

3

2

1

4

3

2

1

F

F

E

E

D

D

C

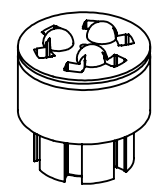
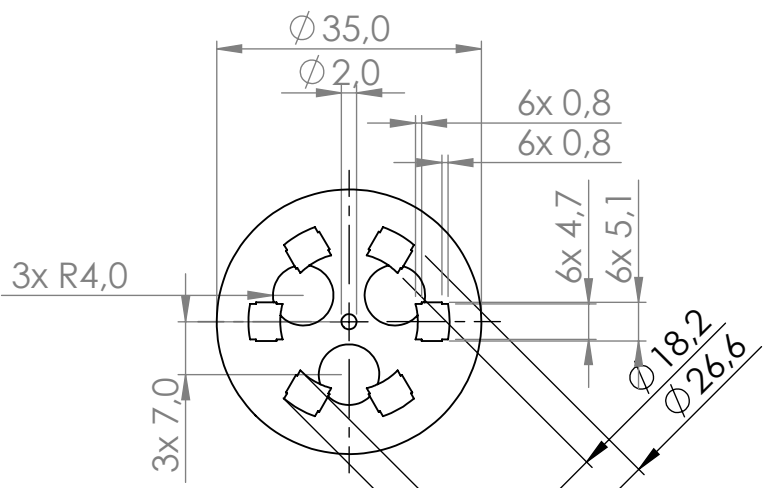
C

B

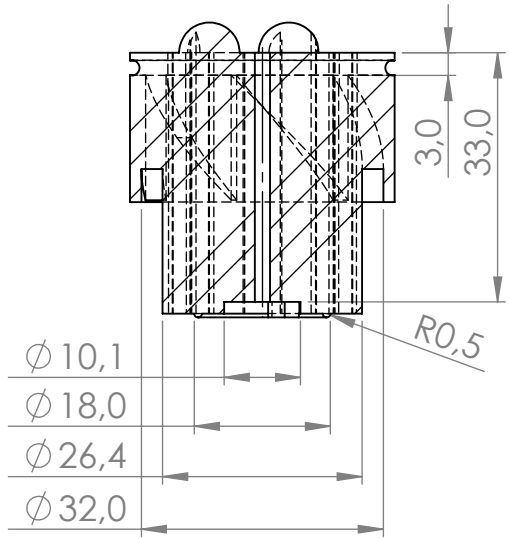
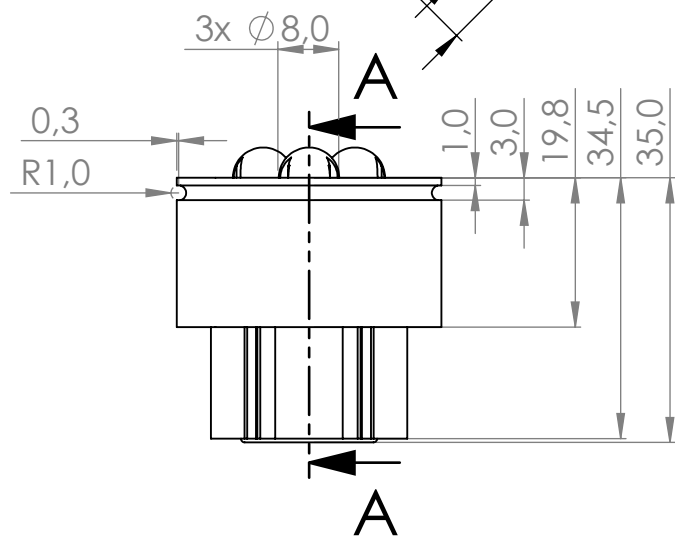
B

A

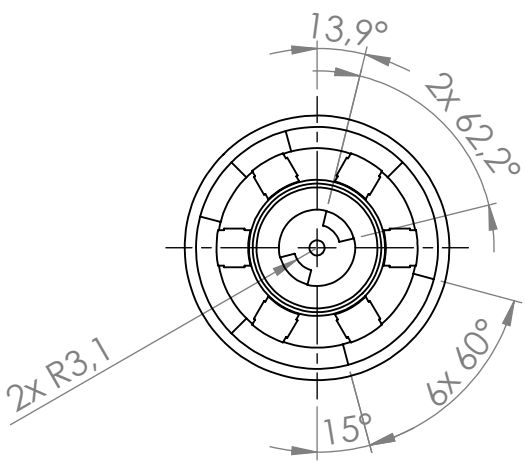
A



Scale 1:2



SECTION A-A



UNLESS OTHERWISE SPECIFIED: DIMENSIONS ARE IN MILLIMETERS SURFACE FINISH: TOLERANCES: LINEAR: ANGULAR:			FINISH:	DEBURR AND BREAK SHARP EDGES	DO NOT SCALE DRAWING	REVISION
NAME	SIGNATURE	DATE			TITLE:	
DRAWN						
CHK'D						
APPV'D						
MFG						
Q.A				MATERIAL: PLA	DWG NO.	A4
				QUANTITY: 1	Housing pneumatic topA	
				WEIGHT:	SCALE:1:1	SHEET 1 OF 1

4

3

2

1

4

3

2

1

F

F

E

E

D

D

C

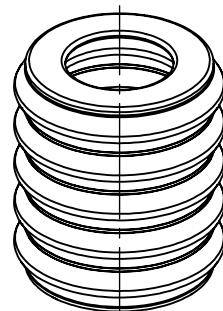
C

B

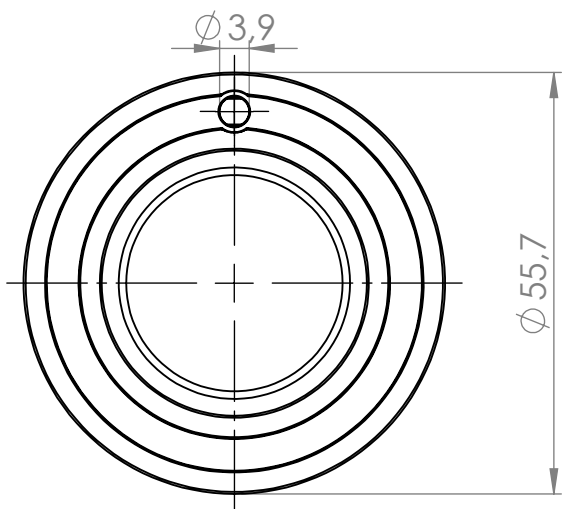
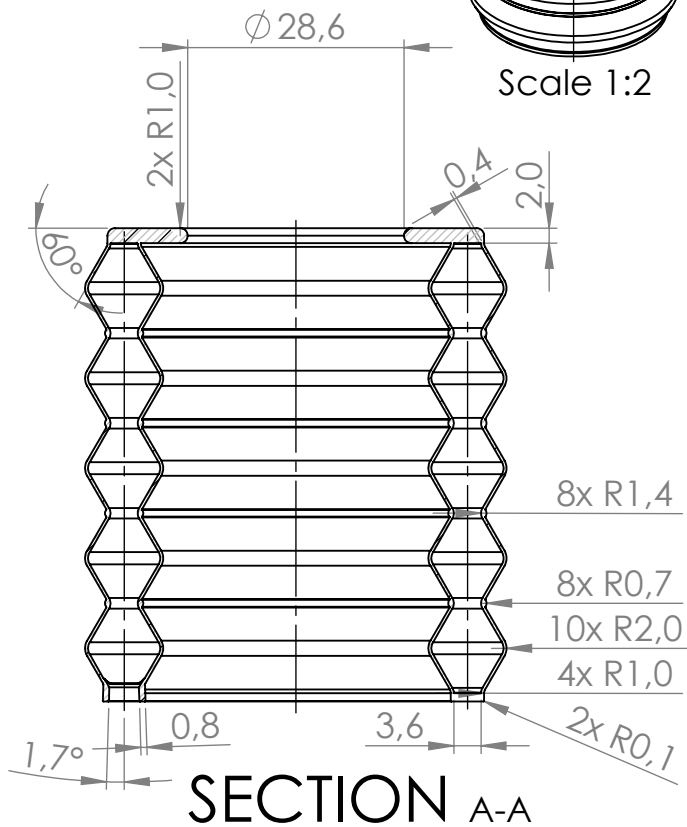
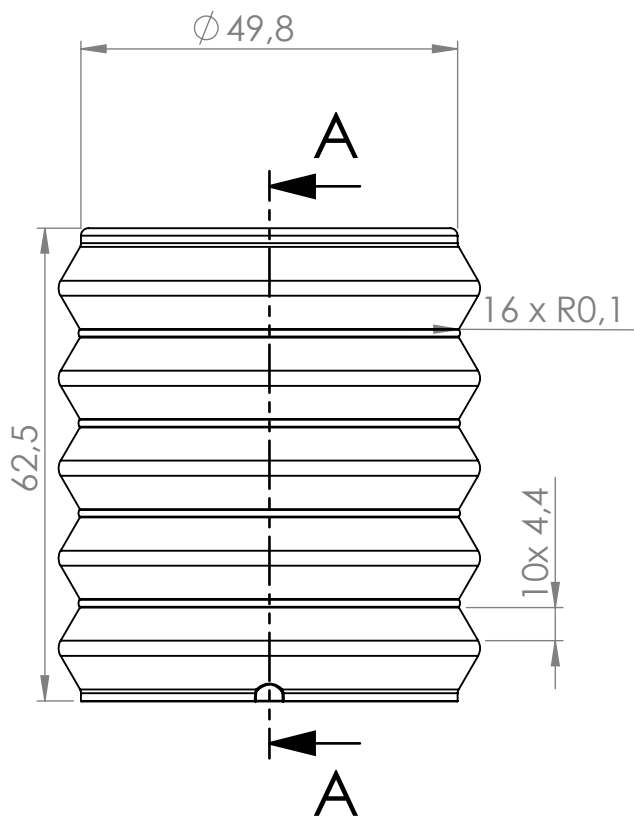
B

A

A



Scale 1:2



UNLESS OTHERWISE SPECIFIED: DIMENSIONS ARE IN MILLIMETERS SURFACE FINISH: TOLERANCES: LINEAR: ANGULAR:			FINISH:	DEBURR AND BREAK SHARP EDGES	DO NOT SCALE DRAWING	REVISION
NAME	SIGNATURE	DATE			TITLE:	
DRAWN						
CHK'D						
APPV'D						
MFG						
Q.A				MATERIAL: Durable (Formlabs), green state	DWG NO.	A4
				QUANTITY: 1	Bellows	
				WEIGHT:	SCALE: 1:1	SHEET 1 OF 1

4

3

2

1

4

3

2

1

F

F

E

E

D

D

C

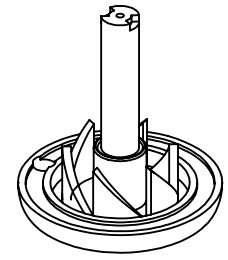
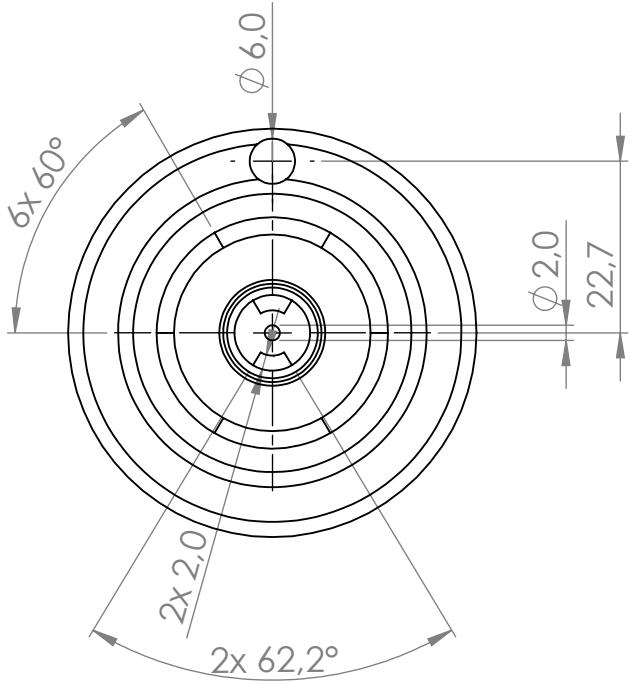
C

B

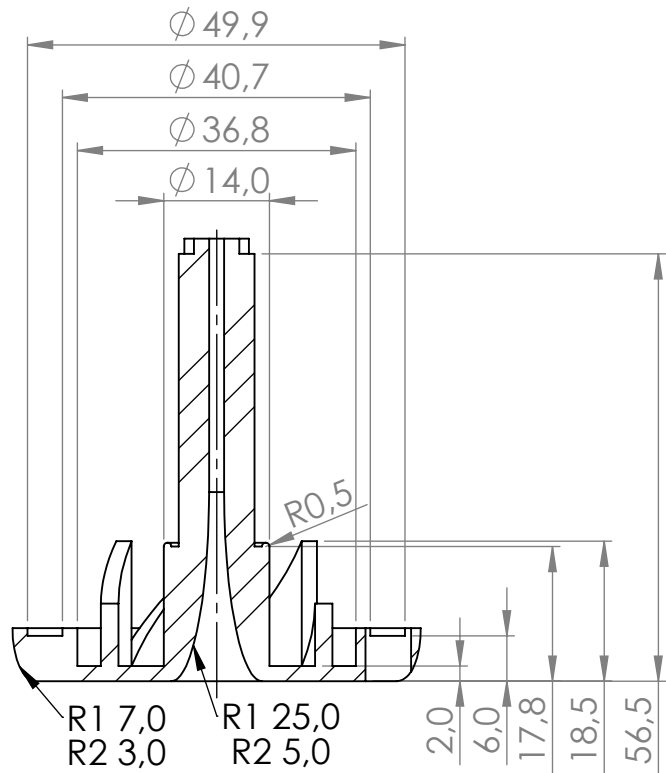
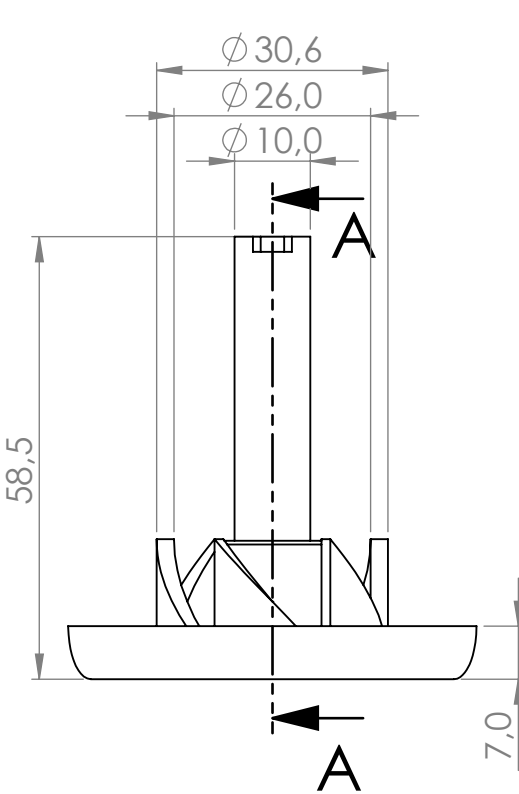
B

A

A



Scale 1:2



SECTION A-A

UNLESS OTHERWISE SPECIFIED:
 DIMENSIONS ARE IN MILLIMETERS
 SURFACE FINISH:
 TOLERANCES:
 LINEAR:
 ANGULAR:

FINISH:

DEBURR AND
BREAK SHARP
EDGES

DO NOT SCALE DRAWING

REVISION

NAME	SIGNATURE	DATE		
DRAWN				
CHK'D				
APPV'D				
MFG				
Q.A				
			MATERIAL:	
			QUANTITY: 1	
			WEIGHT:	

TITLE:	
DWG NO.	44
SCALE: 1:1	SHEET 1 OF 1

PLA Housing pneumatic bottom

4

3

2

1

4

3

2

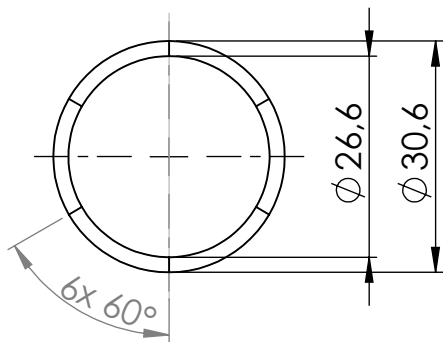
1

F

F



Scale 1:2

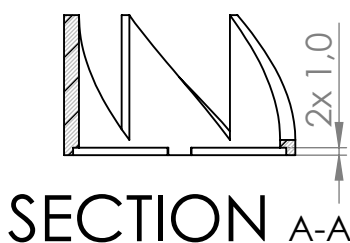
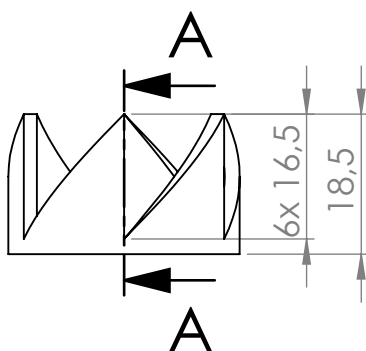


E

E

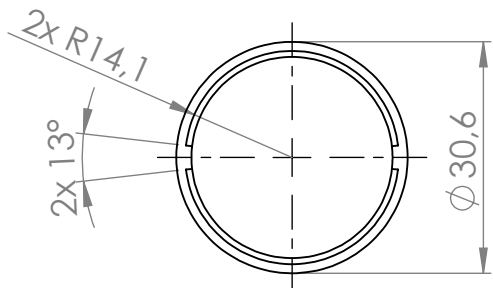
D

D



C

C



B

B

UNLESS OTHERWISE SPECIFIED: DIMENSIONS ARE IN MILLIMETERS SURFACE FINISH: TOLERANCES: LINEAR: ANGULAR:			FINISH:		DEBURR AND BREAK SHARP EDGES		DO NOT SCALE DRAWING		REVISION	
							TITLE:			
							MATERIAL:		DWG NO.	
							Material <not specified>		Selector top	
							QUANTITY: 1		A4	
							WEIGHT:		SCALE:1:1	
									SHEET 1 OF 1	

A

A

4

3

2

1

4

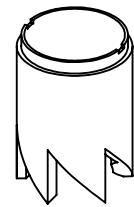
3

2

1

F

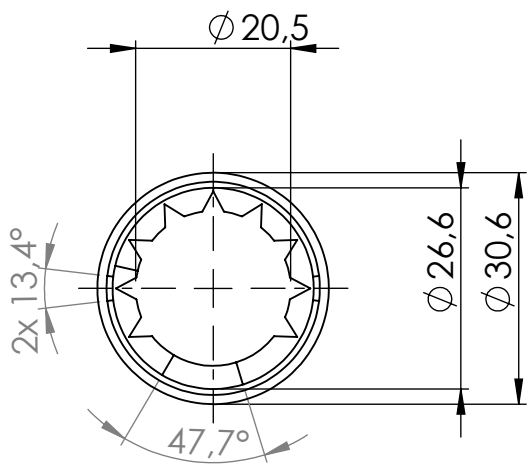
F



Scale 1:2

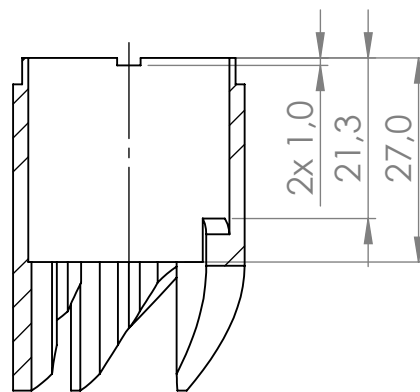
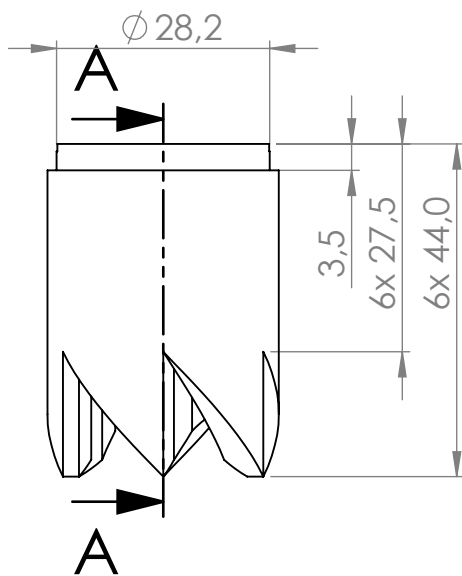
E

E



D

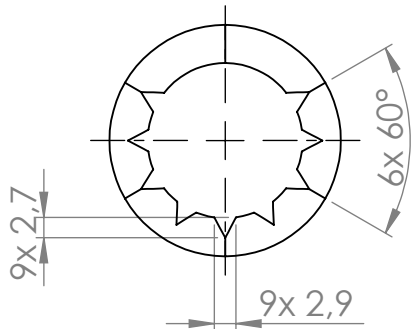
D



SECTION A-A

C

C



B

B

UNLESS OTHERWISE SPECIFIED: DIMENSIONS ARE IN MILLIMETERS SURFACE FINISH: TOLERANCES: LINEAR: ANGULAR:			FINISH:	DEBURR AND BREAK SHARP EDGES	DO NOT SCALE DRAWING	REVISION
NAME	SIGNATURE	DATE			TITLE:	
DRAWN					Selector bottom A4	
CHK'D						
APP'VD						
MFG						
Q.A				MATERIAL: Dental Model V2	DWG NO.	
				QUANTITY: 1	SCALE: 1:1	SHEET 1 OF 1
				WEIGHT:		

A

A

4

3

2

1